

Final Report 2018

Development and Improvement of Flow Models Applied to Multiphase Flows in Large-Diameter Pipes and High-Velocity Flows

Input Parameters | Casing Design | Results | About

CALCULATION TYPE

Worst Case Discharge Production

WELL LOCATION

Offshore Onshore
Seabed Depth [ft]

PVT DATA


Gas Oil Ratio [SCF/STB]
API Gravity [API]
Gas Gravity [SP.Gravity]

BHP CALCULATIONS

VLP VLP + IPR
Water Cut [%]
Oil Flow Rate [STB/D]
BHP WCD [psia]

Generate Avalon Inputs

EXIT



TEMPERATURE CALCULATION

Wellhead Temperature [°F]
Bottomhole Temperature [°F]

PVT CORRELATIONS

Rs and Pb [v]
Bo [v]
 μ_o [v]

WELLBORE FLOW CORRELATION

Hybrid Teles & Waltrich (LSU Model)
Sub Model [v]

WELL INFORMATION

Name
Date of Simulation [8/26/2018 3:57:20 PM]

NEXT

Development and Improvement of Flow Models Applied to Multiphase Flows in Large-Diameter Pipes and High-Velocity Flows

Authors:

Francisco Bruno Xavier Teles
Paulo J. Waltrich
Ipsita Gupta
Richard Hughes
Matheus Sigaki Capovilla
Florencia Anahi Vasquez Cordoba

Craft & Hawkins Department of Petroleum Engineering
Louisiana State University, Baton Rouge

Prepared under BOEM Award M17PX00030

US Department of the Interior
Bureau of Ocean Energy Management
Gulf of Mexico OCS Region



TABLE OF CONTENTS

1.	ABSTRACT.....	7
2.	INTRODUCTION	8
2.1	WORST CASE DISCHARGE RATE CALCULATION.....	8
2.2	TWO PHASE FLOW REGIMES IN VERTICAL PIPES.....	9
2.3	CLASSIFICATION OF SMALL AND LARGE PIPE DIAMETERS.....	11
2.4	TELES AND WALTRICH MODEL.....	12
2.4.1	PAGAN ET AL. (2017) MODEL.....	13
2.4.2	DUNS AND ROS (1963).....	15
2.4.3	MODEL OVERVIEW	15
3.	RESULTS AND DISCUSSION	18
3.1	ERROR CALCULATION METHOD.....	19
3.2	MODELS RESULTS FOR REINICKE ET AL. (1987) FIELD DATA	19
3.3	EVALUATION OF TWO-PHASE FLOW MODELS FOR LOUISIANA STATE UNIVERSITY'S PERTT LAB EXPERIMENTS	21
3.4	EVALUATION OF TWO-PHASE FLOW MODELS FOR FANCHER AND BROWN (1986) FIELD DATA	25
3.5	EVALUATION OF TELES AND WALTRICH MODEL FOR DEVIATED WELLS FROM ASHEIM (1986) FIELD DATA.....	29
3.6	EVALUATION OF TELES AND WALTRICH MODEL USING FIELD DATA FROM ESPANOL ET AL. (1969) and AZIZ AND GOVIER (1972).	30
3.7	PETROBRAS AMERICA	31
4.	CONCLUSIONS.....	33
5.	REFERENCES	34
6.	APPENDIX A – LSU Multiphase Flow Simulator Instructions, Best Practices, and Recommendations.....	37
6.1	Section on Input Parameters	39
6.2	Section on Casing Design	47
6.3	Results.....	50
6.4	About.....	51
6.5	APPENDIX B – Avalon® Input Generation	52
6.6	APPENDIX C – Identifying Errors	55
7.	APPENDIX D – Integrated Reservoir-Wellbore Nodal Analysis WCD Model.....	56
8.	APPENDIX E – TWO-PHASE FLOW REGIME MAP FOR LARGE DIAMETER PIPES AND HIGH-VELOCITY FLOWS (MASTERS THESIS).....	57

LIST OF FIGURES

Figure 1 – Elements required for the prediction of production rates, being (a) a schematic of a petroleum production system, including the reservoir, completion, well, wellhead assembly, and surface facilities extracted from Economides, Hill, Ehlig-Economides, and Zhu (2012), and (b) an example of a nodal analysis plot, including an inflow performance curve and two outflow performance curves, each one calculated using different models. Matheus Sigaki Capovilla (2018)	9
Figure 2 – Simplified diagram for WCD rate calculation. SPE (2015)	10
Figure 3 – Visual representation of the four main flow regimes during upward flow in vertical pipe, namely: bubbly flow, slug flow, churn flow, and annular flow. Source: Guet and Ooms (2005).	10
Figure 4 – Force balance sustained in a Taylor bubble.....	11
Figure 5 – Small and Large pipe diameter zones satisfying $d^*= 18.5$ (dash lines) and $d^*= 40$ (solid lines) for: a) air-water, and b) oil-gas systems. Diameters above the transition zones are considered large (e.g., absence of slug flow) and the diameters below the transition zones are considered small (e.g., the presence of slug flow is possible).	12
Figure 6 – Force balance for a pipe segment for churn and annular flow regimes on (a) gas core and (b) total cross-sectional area (including liquid film and gas core).....	13
Figure 7 – Graphical User Interface of the LSU Multiphase Flow Simulator pressure along the well.	16
Figure 8 – Teles and Waltrich model workflow. The model uses Pagan et al. (2017) approach for churn and annular flow. The chosen sub model for bubbly and slug flow in this study is Duns and Ros (1963).....	17
Figure 9 – Comparison of field bottomhole pressure and simulated bottomhole pressure for Teles and Waltrich; Gray (1974); Duns a Ros (1963); Ansari et al. (1994); OLGA (2000); Beggs and Brill; Mukherjee and Brill; Hagedorn and Brown. The black dash lines represent the error line for $\pm 20\%$ of the simulated pressure BHP.	20
Figure 10 – Average absolute error and standard deviation of the errors for Teles and Waltrich; OLGA (2000); Gray (1974); Ansari et al. (1994); Beggs and Brill; Hagedorn, Mukherjee and Brill; Brown, Duns and Ros (1963). The columns represent the average absolute error and the line intervals the standard deviations.	21
Figure 11 – Comparison between Teles and Waltrich model and experimental results in terms of pressure gradient versus gas superficial velocities for 4, 8, and 12 in pipe diameter and superficial liquid velocities from 0.09 to 13.9 ft/s (Figures 10a to 10f).....	22
Figure 12 – Comparison errors of pressure gradient in terms of slip velocity for 4, 8, and 12 in pipe diameter for Teles and Waltrich, Duns and Ros, Beggs and Brill, Murkherjee and Brill, and Hagedorn and Brown models. Green curves represents scenarios having: slip ratio less than one; red curves: slip ratio between one and 100; blue curves: slip ratio greater than 100.	23
Figure 13 – Average Absolute Error of pressure gradient in % for Teles and Waltrich, Duns and Ros, Beggs and Brill, Murkherjee and Brill, and Hagedorn and Brown models for 4, 8, and 12in for the LSU/PERTT Lab experimental data reported by Waltrich et al. (2017).	24

Figure 14 – Overall average absolute error of pressure gradient in % for Teles and Waltrich, Duns and Ros, Beggs and Brill, Mukherjee and Brill, and Hagedorn and Brown models for for the LSU/PERTT Lab experimental data reported by Waltrich et al. (2017).. 24

Figure 15 – Comparison between simulation results using the model proposed in this study and measured wellbore pressure profile (field data from Fancher and Brown, 1963). Circles represent the measured pressures and continuous lines are the simulated pressures. The horizontal dash lines represent the transition of flow regime along the well. 28

Figure 16 – Average absolute error of the simulated bottomhole pressure for Teles and Waltrich, Hagedorn and Brown, Mukherjee and Brill, Beggs and Brill, Duns and Ros, and Pagan et al. (2016), for Fancher and Brown (1963) field data. The standard deviation of the errors are represented by the error bars on each model. 28

Figure 17 – Comparison of field bottomhole pressure and simulated bottomhole pressure for Teles and Waltrich for 34 well in Forties field from Asheim (1986). The black dash lines represent the error line for $\pm 20\%$ of the simulated pressure BHP..... 29

Figure 18 – Average absolute error of the simulated bottomhole pressure for Teles and Waltrich, Mukherjee and Brill, Hagedorn and Brown, Beggs and Brill, and Duns and Ros for Asheim (1986) field data. The standard deviation of the errors are represented by the error bars on each model. 30

Figure 19 – Comparison of field bottomhole pressure and simulated bottomhole pressure for Teles and Waltrich for Espanol et al. (1989) data set. The black dash lines represent the error line for $\pm 20\%$ of the simulated pressure BHP. 30

Figure 20 – Average absolute error of the simulated bottomhole pressure of the three different wells for Teles and Waltrich; Mukherjee and Brill; Hagedorn and Brown; Beggs and Brill; and Duns and Ros for Petrobras’ field data. 31

Figure 21 – Overall average absolute error of the simulated bottomhole pressure for Teles and Waltrich, Mukherjee and Brill, Hagedorn and Brown, Beggs and Brill, and Duns and Ros for Petrobras’ field data. The standard deviation of the errors are represented by the error bars on each model. 32

LIST OF TABLES

Table 1 – Source and main characteristics of the database used to evaluate the performance of the Teles and Waltrich model and other commonly used correlations.	18
---	----

ABBREVIATIONS AND ACRONYMS

BOEM	Bureau of Ocean Energy Management
WCD	Worst Case Discharge
IPR	Inflow Performance Relationship
TPR	Tubing Performance Relationship
BHP	Bottomhole Pressure [psi]
GLR	Gas Liquid Ratio [SCF/STB]
GOR	Gas Oil Ratio [SCF/STB]
q_L	Liquid Ratio [BBL/d]
ID	Pipe Inner Diameter [in]
ρ	Density [lb/ft^3]
g	Gravitational Acceleration [$32.2 \text{ ft}/\text{s}^2$]
d^*	Dimensionless Diameter
V_{sg}	Gas Superficial Velocity [ft/s]
V_{sl}	Liquid Superficial Velocity [ft/s]

1. ABSTRACT

This work proposes a model developed at LSU (called here as Teles and Waltrich model) that can determine pressure gradient in all flow regimes considering the concept of small and large diameter pipes. A series of field and experimental dataset for air-water, water-natural gas, and oil-natural gas systems are tested for a wide range of conditions in order to validate this model. The main objective of this study is to evaluate the performance of Teles and Waltrich model and other models commonly used in worst-case-discharge (WCD) calculations.

The scenarios for WCD calculations in most of the offshore drilling operations occurs in situations with high oil and gas flow rates, large diameters and high pressure flows. An important part of WCD calculations is the determination of the pressure variation during the multiphase flow of oil, gas, sand and water in the wellbore during a blowout, which involves the use of multiphase flow correlations. These correlations are developed from different empirical and mechanistic wellbore flow models, being most of them flow regime dependent. However, most of these models were originally developed and validated for air-water two-phase flows, for low pressures, and for pipe diameters much smaller than the ones usually encountered in the offshore wells. There is an understanding that the fluid behavior changes considerably from small to large diameters, mainly regarding the observation of churn flow regime for large-diameter pipes, when slug flow would be expected in small diameters. In addition, most of these models available in commercial packages (often used for WCD calculations) do not consider the presence of churn flow regime, and the use of slug flow models in flow conditions that it does not exist may lead to significant errors.

Some of the comparisons between model results and experimental/field data indicates that the use of slug flow model can lead to errors higher than churn flow models. These results suggest that the use of Teles and Waltrich model, which includes a churn flow model, should be used for WCD calculations to obtain more accurate results in some cases. Some of the analysis also show that, at high pressures, *slug flow might not be present for oil-gas flows for diameters as small as 1 inch!* The application of flow regime models for slug flow for pipe diameters between 1 and 4 inches is widely used in empirical and mechanistic models in the oil and gas industry. This may deliver erroneous results, as wellbore flow models will try to predict churn flow regime using a slug flow model. For this reason, it is relevant to implement the concept of small and large diameter presented in this report in wellbore flow models for a reliable prediction of pressure gradient in vertical two-phase flow in pipes.

2. INTRODUCTION

Vertical gas-liquid two-phase upward flow can be found in a wide range of industrial applications such as in offshore risers in the petroleum industry, cooling towers in the nuclear industry, and in gas-liquid pipelines in petrochemical plants. A typical example of a problem that requires the knowledge about vertical two-phase upward flow in pipes is in worst-case-discharge (WCD) calculations. The Bureau of Ocean Energy Management (BOEM) defined the WCD rate as the maximum uncontrollable daily flow rate of hydrocarbons through an unobstructed wellbore (SPE, 2015). In other words, WCD rate is the maximum expected flow rate during a blowout, considering the absence of an in-hole drillstring and a wellhead.

Recent new regulations requires from any operator company a report describing the plans to drill new wells in the Gulf of Mexico the submission of an Oil Spill Response Plan (OSRP), which should include a contingency plan to be followed in case of a blowout (Buchholz et al., 2016). An estimative of WCD rate is required in this type of report. Two main characteristics of the flow in the wellbore are expected during WCD events: high flow rates in large-diameter long-vertical pipes. OSRP reports present WCD flow rates in the Gulf of Mexico ranging from 0.63 to 75,678 m³/day (4 to 476,000 bbl/day), averaging for the Central Gulf of Mexico about 9,540 m³/day (60,000 bbl/day), and for the Western Gulf of Mexico about 2,225 m³/day (14,000 bbl/day) (Buchholz et al., 2016). Furthermore, Zulqarnain (2015) described a representative well configuration based on statistical analysis about the current wells in the Gulf of Mexico, in which the average pipe diameter is about 0.25 m (~10 in).

Some studies have been carried out on multiphase flow in pipes of large diameter (Hernandez-Perez, Zangana, Kaji, & Azzopardi, 2010; A. Ohnuki & Akimoto, 1996; Akira Ohnuki & Akimoto, 2000; Omebere-Iyari, Azzopardi, & Ladam, 2007; Schoppa, Zabaras, Menon, & Wicks, 2013). However, there is still a lack of investigation about flows in larger diameter pipes and high flow rates.

Most mathematical models developed for vertical two-phase flow in pipes are based on experimental and field data for small diameter pipes (e.g., ID < 0.10 m - or ~4 in) and low liquid velocities, typically lower than 1 m/s (Omebere-Iyari et al., 2007; Smith, Schlegel, Hibiki, & Ishii, 2012). Thus, the applicability of such models to conditions involving large diameter and high-velocity flows is still questionable. Therefore, it is evident that studies are still needed on evaluating wellbore flow models and proposing improvements for its application on WCD calculations.

2.1 WORST CASE DISCHARGE RATE CALCULATION

In 2015, SPE released a technical report addressing the calculation of WCD rates (SPE, 2015). This calculation is based on a technique used for prediction of production rates as a function of the reservoir characteristics and the pressure drop along the flowing wellbore. This method is called nodal analysis (see Figure 1.b). It makes use of the inflow and outflow performance curves to calculate the flow rate of a well. The inflow performance relationship (IPR) represents the fluid flow in the reservoir (fluid flow through a porous medium) and the outflow performance relationship, also known as tubing performance relationship (TPR), represents the wellbore (fluid flow in pipes). Petroleum production systems, as shown in Figure 1.a, often deal with a relatively narrow range of wellbore pipe effective diameters, from 0.04 to 0.15 m (~1.5 to ~6 in), and flow rates lower than 1,600 m³/day (~10,000 bbl/day) (Takacs, 2001). On the other hand, WCD conditions involve higher two-phase fluid flow rates (possibly higher than 16,000 m³/day, or ~100,000 bbl/day) and mostly larger pipe diameters (up to 0.50 m or ~20 in). Some recent studies (Ali, 2009; Omebere-Iyari et al., 2007; Schoppa et al., 2013) reported relevant differences concerning the multiphase flow dynamics in large-diameter vertical pipes when compared to small-diameter pipes. When not considered, these differences in pipe diameters can be translated into erroneous predictions of pressure drops for the wellbore and, consequently, inaccurate WCD rate calculations.

Waltrich et al. (2017) tested several different models used in WCD calculations against experimental pressure gradient data of upward two-phase flow in large diameter pipes. Most models showed

errors larger than 50% for the pressure gradient predictions. Thus, tracking the elements that lead these models to large levels of uncertainty is necessary.

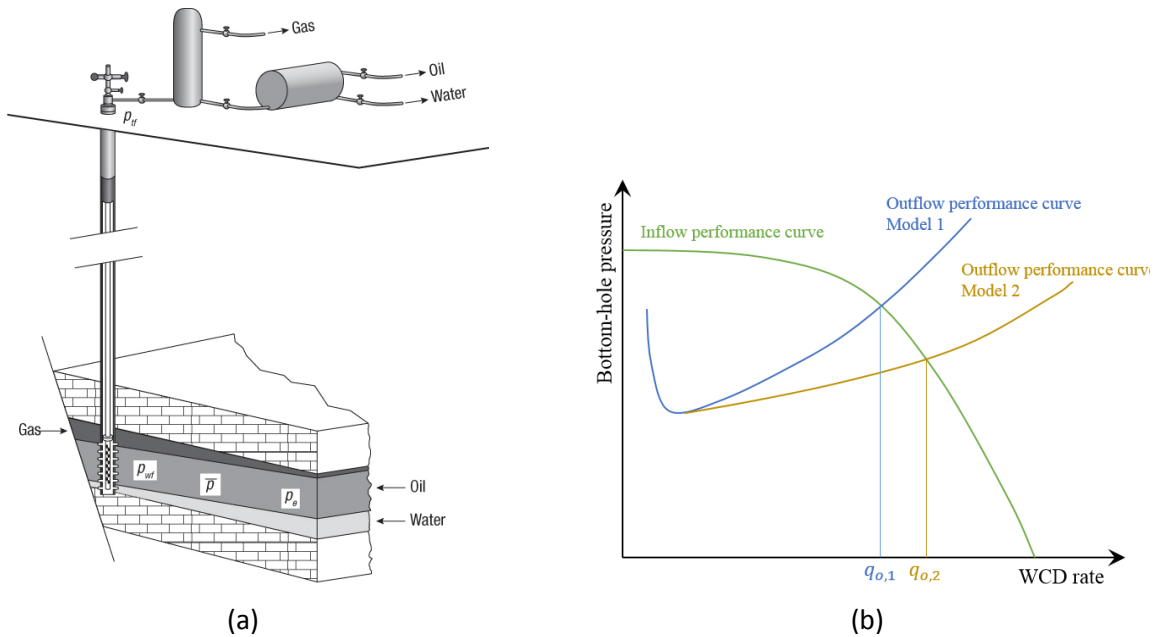


Figure 1 – Elements required for the prediction of production rates, being (a) a schematic of a petroleum production system, including the reservoir, completion, well, wellhead assembly, and surface facilities extracted from Economides, Hill, Ehlig-Economides, and Zhu (2012), and (b) an example of a nodal analysis plot, including an inflow performance curve and two outflow performance curves, each one calculated using different models. Matheus Sigaki Capovilla (2018)

2.2 TWO PHASE FLOW REGIMES IN VERTICAL PIPES

Figure 2 presents a simplified diagram for the calculation of WCD rates. As it can be seen, regarding the outflow performance curve, the determination of flow regimes has a direct impact in WCD calculations.

Flow regime prediction is a crucial part of two-phase flow analysis, since many multiphase flow models are flow regime dependent. Two-phase flow regimes are described by Shoham (2006) as a group of similar geometrical distribution of the gas and liquid phases in a pipe during a two-phase flow. Although it is possible to find several different vertical upward two-phase flow regimes characterizations throughout the literature, the four flow regimes listed below are most commonly defined in upward gas-liquid two-phase flow in vertical pipes. Figure 3 illustrates Bubbly, Slug, Churn, and Annular flow regimes.

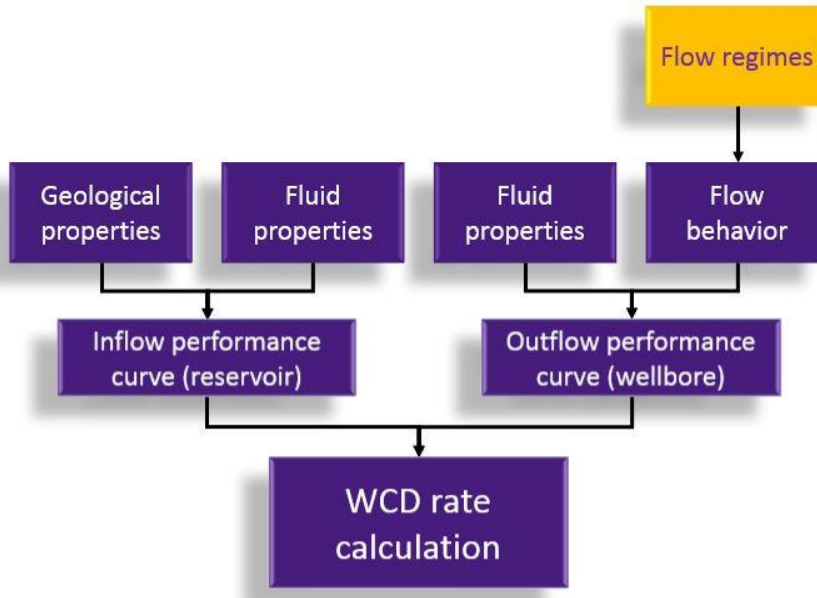


Figure 2 – Simplified diagram for WCD rate calculation. SPE (2015)

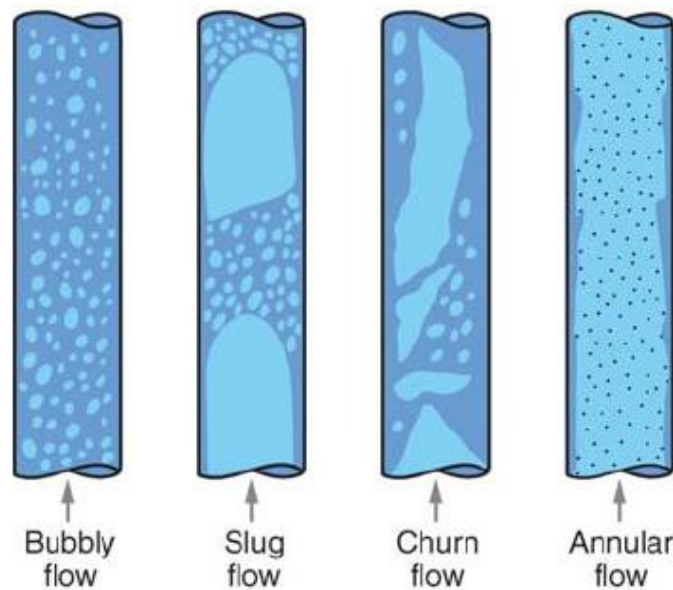


Figure 3 – Visual representation of the four main flow regimes during upward flow in vertical pipe, namely: bubbly flow, slug flow, churn flow, and annular flow. Source: Guet and Ooms (2005).

- Bubbly flow: This regime occurs when there are relatively low gas velocities and high liquid velocities. The continuous liquid phase flows carrying dispersed gas bubbles. Both phases move upward.
- Slug flow: This flow is characterized when there are a higher gas velocity and the bubbles get closer and coalesce forming a series of slug units. These slug units are composed by bullet shaped bubbles (also called Taylor bubbles) containing small bubbles dispersed within them. They are axially symmetrical and occupy almost the diameter of the pipe. There is a thin liquid film moving downward between the Taylor bubbles and the pipe wall as the gas flows upwards.

- Churn flow: For even higher gas velocities, these large bubbles are not stable anymore, and there is a chaotic movement of both gas and liquid phases in the downward and upward directions. There is no clear boundary between the phases.
- Annular flow: This occurs for very high gas velocities and it is characterized by a continuous fast-moving gas core with some liquid-phase droplets entrained, while the liquid-phase forms a continuous thin layer on the pipe wall flowing upwards.

2.3 CLASSIFICATION OF SMALL AND LARGE PIPE DIAMETERS

The flow regime determination is assumed by many investigators as the central problem in the field of multiphase flow in pipes (Shoham, 2006). Recent studies have pointed out the significant difference of flow regime behavior in small and large diameter pipes (Ali Shazia & Yeung, 2013; Akira Ohnuki & Akimoto, 2000; Wu et al., 2017). Among these differences, the absence of slug flow in large pipe diameters has been evident in several studies (Ali Shazia & Yeung, 2013; M. S. Capovilla, Cavalcanti de Sousa, & Waltrich, 2017; Cheng, Hills, & Azzopardi, 1998; Hibiki & Ishii, 2000; Kataoka & Ishii, 1987; Akira Ohnuki & Akimoto, 2000; Omebere-Iyari et al., 2007; Shoukri, Hassan, & Gerges, 2008; Wu et al., 2017), thus, it should be considered in two phase flow models.

The work of Schlegel et al. (2009) discusses that small and large diameter pipes should be differentiated using the dimensionless diameter criterion defined by Kataoka and Ishii (1987), which is represented by equation 2.1. This dimensionless diameter determination considers the force balance between the surface tension of the two interacting fluids (liquid and gas) and the pressure of the liquid phase over the bubble, as shown in Figure 4. It can be used to estimate the maximum diameter size for slug flow to occur in a vertical two-phase flow,

$$d^* = d \sqrt{\frac{g(\rho_l - \rho_g)}{\sigma}} \quad (2.1)$$

where σ is the surface tension between gas and liquid phases, ρ_g and ρ_l are the gas and liquid densities, g is the gravitational acceleration, and d is the pipe diameter.

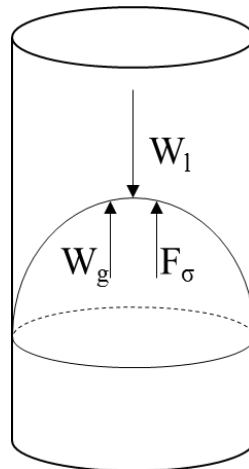


Figure 4 – Force balance sustained in a Taylor bubble.

According to Kataoka and Ishii (1987), pipes are classified as large-diameters when at their flow conditions d^* is greater than 40, and small-diameter pipes are those which d^* is smaller or equal to 18.5 (Shen, Hibiki, & Nakamura, 2015). For vertical two-phase flow in large-diameter pipes, Taylor bubbles, which are the main feature of Slug flow, are not stable. Therefore, slug flow does not exist at this condition.

Some two-phase flow experimental studies in vertical pipes of large diameter ($ID > 5$ in) showed that only 1 out of 24 studies witnessed slug flow (Ali Shazia & Yeung, 2013), which can confirm the difference between large- and small-diameter pipes.

Figure 5a and 5b show the pipe diameters satisfying the concept of small and large diameter proposed by Kataoka and Ishii (1987) for Equation 2.1 for air-water and oil-gas flows, from atmospheric pressure to 3,000 psi. For oil-gas system, 30° API oil and gas with 96.5% methane are used for the calculations. It can be seen that, for air-water systems, the diameter which satisfies the large-diameter threshold of $d^* = 40$ slightly increases with pressure, while for oil-gas systems the diameter becomes smaller as pressure increases, being approximately 1 in at 3,000 psi and 60°F. This different trends of diameter size with pressure are mainly caused by differences of surface tension in the two systems, as the surface tension of crude oil and gas decreases significantly for higher pressures (Baker & Swerdloff, 1956), whereas for water it stays nearly constant.

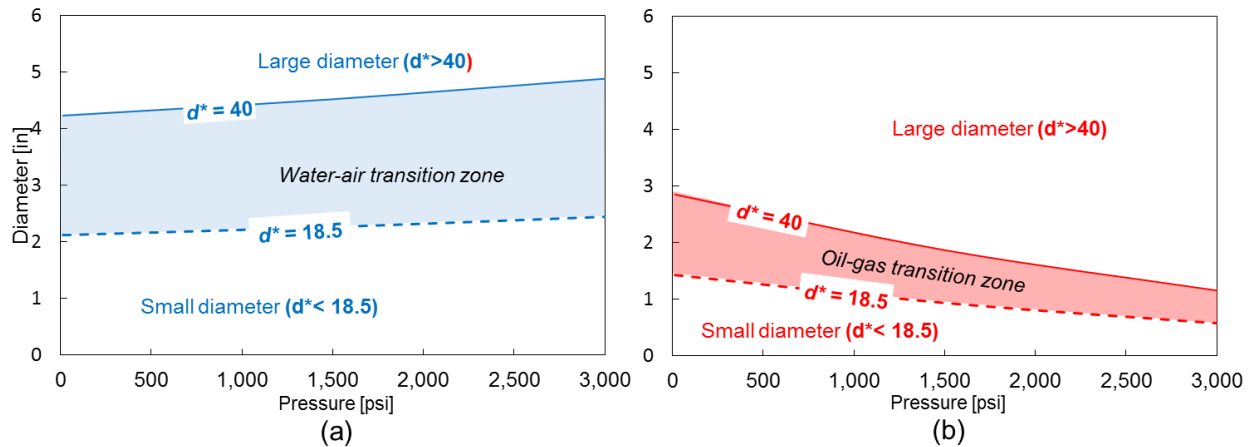


Figure 5 – Small and Large pipe diameter zones satisfying $d^* = 18.5$ (dash lines) and $d^* = 40$ (solid lines) for: a) air-water, and b) oil-gas systems. Diameters above the transition zones are considered large (e.g., absence of slug flow) and the diameters below the transition zones are considered small (e.g., the presence of slug flow is possible).

Most of the multiphase flow models are flow regime dependent, but as seen in Figure 5 *at high pressures Taylor bubbles (and consequently slug flow) might not be present on oil-gas flows for diameters as small as 1 inch!* The application of flow regime models for slug flow for pipe diameters between 1 and 4 inches is widely used in empirical and mechanistic models in the oil and gas industry. This may deliver erroneous results, as these wellbore flow models will try to predict possibly churn flow regime using a slug flow model. For this reason, it is crucial to implement the concept of small and large diameter in the models for a reliable prediction of pressure gradient in vertical two-phase flow in pipes.

Some authors reported that under conditions at which slug flow would exist, in larger diameter pipe it might be replaced by a flow regime characterized by large deformed bubbles flowing upwards or sideways. This flow regime has been commonly referred to as cap-bubble flow (Ohnuki and Akimoto, 2000; Schlegel et al., 2009; Ali and Yeung, 2013). A study about cap-bubbly flow has been carried out at LSU and is reported in Matheus Sigaki Capovilla (2018) thesis.

2.4 TELES AND WALTRICH MODEL

A hybrid wellbore multiphase flow model has been developed at LSU to predict pressure gradient for all flow regimes in large-diameter pipes. This model consists of the combination of the mode proposed by Pagan, Williams, Kam, and Waltrich (2017), for churn and annular flow for large pipe diameters, with the empirical correlation of Duns and Ros (1963) for bubbly and slug flow. In addition, the hybrid model, herein referred as Teles and Waltrich model, also accounts for the concept of large and small diameter

proposed by Kataoka and Ishii (1987). The purpose was to implement the concept of large and small diameter in order to identify whether slug flow occurs or not.

The main objective of Teles and Waltrich model is to accurately predict pressure gradient for oil and gas flow along large diameter pipes with high gas-liquid-ratios, as most of the models used to determine pressure drop along wells were originally developed and validated for air and water two-phase flow in pipe diameters smaller than 8 inches. A wide set of experimental and field data was used to evaluate the accuracy of this model, as well as for comparison with other commonly used empirical and mechanistic models.

2.4.1 PAGAN ET AL. (2017) MODEL

Pagan et al. (2017) proposed a steady-state model for calculating pressure gradient in churn and annular flow in large pipe diameters. The model is based on an approach proposed by Jayanti and Brauner (1994) for the churn flow regime in vertical pipes validated for small diameters. It consists on applying the concept of force balance in the gas core with length dl and cross-sectional area A_c , as shown in Figure 6. The gas core is represented by Figure 6(a) and the gas-liquid mixture is represented by Figure 6(b).

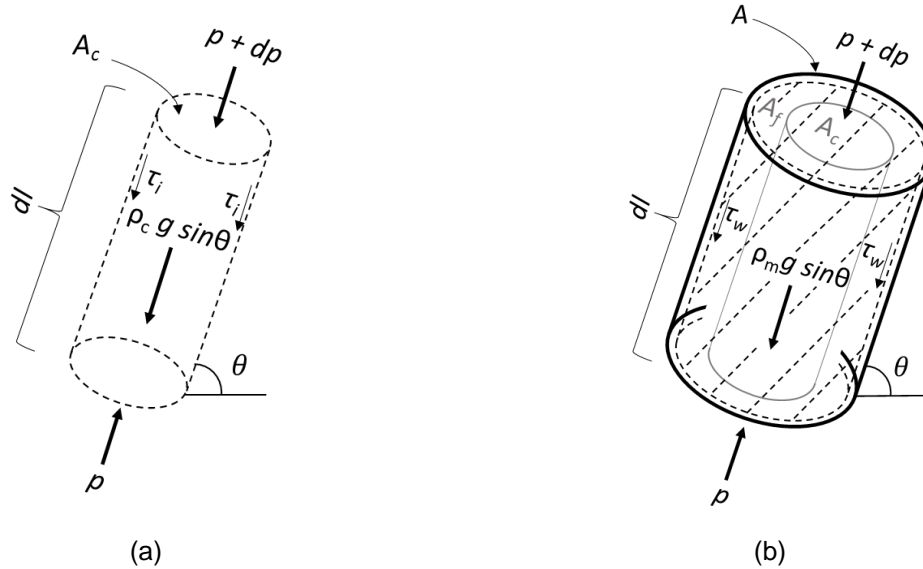


Figure 6 – Force balance for a pipe segment for churn and annular flow regimes on (a) gas core and (b) total cross-sectional area (including liquid film and gas core).

According to Pagan et al. (2017), both gas and liquid phases flow upward. In Figure 6a, the interaction between the gas and liquid phases is given by the shear stress (τ_i) at the gas-liquid interface. In addition, the force acting between the liquid phase and the pipe wall is represented by the wall shear stress (τ_w), as shown in Figure 6(b). Neglecting the acceleration term, the momentum balance equation for both control volumes represented in Figure 6(a) and Figure 6(b) are given by the following expressions (Jayanti & Brauner, 1994),

$$-\frac{dp}{dl} = \frac{4\tau_i}{d\sqrt{\alpha}} + \rho_g g \sin\theta \quad (2.2)$$

$$-\frac{dp}{dl} = \frac{4\tau_w}{d} + [\rho_g \alpha + \rho_l(1 - \alpha)] g \sin\theta \quad (2.3)$$

where dp/dl is the pressure gradient for the pipe segment dl , τ_i is the interfacial shear stress, τ_w is the wall shear stress, g is the gravitational acceleration, d is the diameter of the section, θ is the inclination angle

with the horizontal, α is the void fraction, ρ_g and ρ_l are the gas and liquid densities. Equations 2.2 and 2.3 are solved for dp/dl and θ .

2.4.1.1 WALL AND INTERFACIAL SHEAR STRESS

In the churn flow regime, the liquid motion is oscillatory. However, the net liquid rate is upward. Thus, (Jayanti & Brauner, 1994) proposed that the average wall shear stress should be calculated based on the net liquid flow rate, neglecting the liquid flow variation with time. As in the annular flow regime, the net liquid film flows always upward along the pipe wall. The wall shear stress, τ_w , is calculated from the following relationship for both annular and churn flow regimes,

$$\tau_w = \frac{1}{2} \rho_l f_l \left(\frac{u_{sl}}{1 - \alpha} \right)^2 \quad (2.4)$$

where u_{sl} is the superficial liquid velocity, and f_l is the friction factor of the liquid film. Equation 2.4 represents the wall shear stress for single-phase flow, considering that only the liquid phase is in contact with the pipe wall. For laminar flow in the liquid film, and Reynold number, Re_{lf} smaller than 2,100, the Fanning friction factor given by Equation 2.5 is used. For turbulent flow, when Re_{lf} is greater than 2,100, Blasius Equation 2.6 for smooth pipes is used.

$$f_l = \frac{16}{Re_{lf}} \quad (2.5)$$

$$f_l = \frac{0.079}{Re_{lf}^{0.25}} \quad (2.6)$$

The Reynolds number is given by,

$$Re_{lf} = \frac{u_{lf} \rho_l d}{\mu_l} \quad (2.7)$$

where d is the pipe diameter, μ_l is the liquid viscosity, u_{lf} the actual liquid film velocity of the film, which is given by:

$$u_{lf} = \frac{u_{sl}}{1 - \alpha} \quad (2.8)$$

The interfacial shear stress between the gas core and the liquid film shown in Figure 5a is calculated with the equation below:

$$\tau_i = \frac{1}{2} \rho_g f_i \left(\frac{u_{sg}}{\alpha} \right)^2 \quad (2.9)$$

where u_{sg} is the gas superficial velocity. Equation 2.9 can be used since the gas velocity is generally much larger than the liquid velocity when the fluids are flowing under churn or annular flow regimes. Thus, the liquid velocity is neglected, and the interfacial shear stress is calculated based on single-phase gas flow.

The study of Pagan et al. (2017) proposed that the interfacial friction factor should be calculated as suggested by Jayanti and Brauner (1994) by the average of $f_{i,W}$ and $f_{i,B}$ as shown below:

$$f_i = \frac{1}{2} (f_{i,W} + f_{i,B}) \quad (2.10)$$

However, instead of using the empirical correlation for $f_{i,W}$ proposed by Wallis (1969) assuming thin liquid films in pipes and $f_{i,B}$ correlation proposed by Bharathan, Richter, and Wallis (1978), it should be used the correlation of as suggested by (Alves, 2014), which leads to best results for churn and annular flow regimes, and it is given by:

$$f_{i,B} = 0.005 + 10^{(-0.56 + \frac{9.07}{d^*})} \left[\frac{d^*(1 - \alpha)}{4} \right]^{(1.63 + \frac{4.74}{d^*})} \quad (2.11)$$

where d^* is the dimensionless diameter proposed by Kataoka and Ishii (1987) (equation 2.1). Pagan et al. (2017) proposes the use of the general equation for interfacial friction factor proposed by Wallis (1969) for $f_{i,W}$ as given by,

$$f_{i,W} = 0.005 \left(1 + 300 \frac{\delta}{D} \right) \quad (2.2)$$

where δ/D is the dimensionless liquid film thickness. The latter term can be represented in terms of void fraction (α), as the void fraction can be interpreted by the cross-sectional area of the gas core, A_c , divided by the cross-sectional area of the pipe A . Thus, this study proposes Wallis (1969) modified interfacial friction factor without assumption of thin liquid film in pipes for churn flow regime, given by,

$$f_{i,W} = 0.005 + 0.75 (1 - \sqrt{\alpha}) \quad (2.3)$$

Wallis (1969) modified interfacial friction factor equation with assumption of thin liquid film is used only for annular flow regime, given by,

$$f_{i,W} = 0.005 + 0.375 (1 - \alpha) \quad (2.4)$$

Since churn flow is gradually suppressed with increasing in inclinations, this model is indented to provide reasonable results for inclination angles up to 15° with the vertical Pagan (2016).

2.4.2 DUNS AND ROS (1963)

Duns and Ros (1963) developed their model based in three different regions: bubbly, plug, and mist flow. This empirical model for pressure drop along the wellbore is a result of an intense laboratory study of 4,000 two phase flow tests. The experiments were carried out in vertical pipes with diameters ranging from 1.26 to 5.60 inches for gas-water flow (Brill & Mukherjee, 1999), and gas-diesel oil flows. In the hybrid model presented in this report, Duns and Ros correlation was chosen for bubbly and slug flow due to its good accuracy on predicting pressure drop in these flow regimes for air-water and gas-oil fluids, for a wide range of pipe diameters.

2.4.3 MODEL OVERVIEW

Figure 7 illustrates the Graphical User Interface (GUI) developed in order to run the simulations for pressure along wells. The algorithm developed is written on Visual Basic Application (VBA). The input data such as Well Calculation Type, Well Location, PVT Data, BHP Calculations, PVT and Wellbore Flow Correlations, Casing Design, Generations of Avalon Inputs (Sensitivity), etc. can be easily inserted for the simulations run.

Input Parameters | Casing Design | Results | About

LSU

CALCULATION TYPE

Worst Case Discharge Production

WELL LOCATION

Offshore Onshore

Seabed Depth [ft]

PVT DATA

Gas Oil Ratio [SCF/STB]

API Gravity [API]

Gas Gravity [SP.Gravity]

BHP CALCULATIONS

VLP VLP + IPR

Water Cut [%]

Oil Flow Rate [STB/D]

BHP WCD [psia]

Generate AVALON Inputs

TEMPERATURE CALCULATION

Wellhead Temperature [°F]

Bottomhole Temperature [°F]

PVT CORRELATIONS

Rs and Pb ▼

Bo ▼

μ_o ▼

WELLBORE FLOW CORRELATION

Hybrid Teles & Waltrich (LSU Model)

Sub Model Duns and Ros ▼

WELL INFORMATION

Name

Date of Simulation 8/9/2018 8:57:20 AM

Figure 7 – Graphical User Interface of the LSU Multiphase Flow Simulator pressure along the well.

The flow chart shown in the Figure 8 illustrates how the algorithm of the proposed model works for the calculation of pressure in each section of the well. This algorithm is deployed for each length increment from a known pressure (for instance, from the wellhead) to the bottom of the well. A full explanation containing the step-by-step to run simulations together with the best practices and recommendations to properly run simulations with the LSU model is on APPENDIX A “LSU Multiphase Flow Simulator Instructions, Best Practices, and Recommendations.”

In the previous report from LSU to BOEM (Waltrich et al., 2017 - Award M15PC00007), the main conclusion of that experimental study was that any wellbore flow correlation tested would provide errors lower than 10% for slip ratios lower than the unit ($v_{sg}/v_{sl} < 1$). Thus, for slip ratios lower than the unit, the model of Duns and Ros (1963) is selected to calculate the pressure gradient in the wellbore for small diameters and any flow regime.

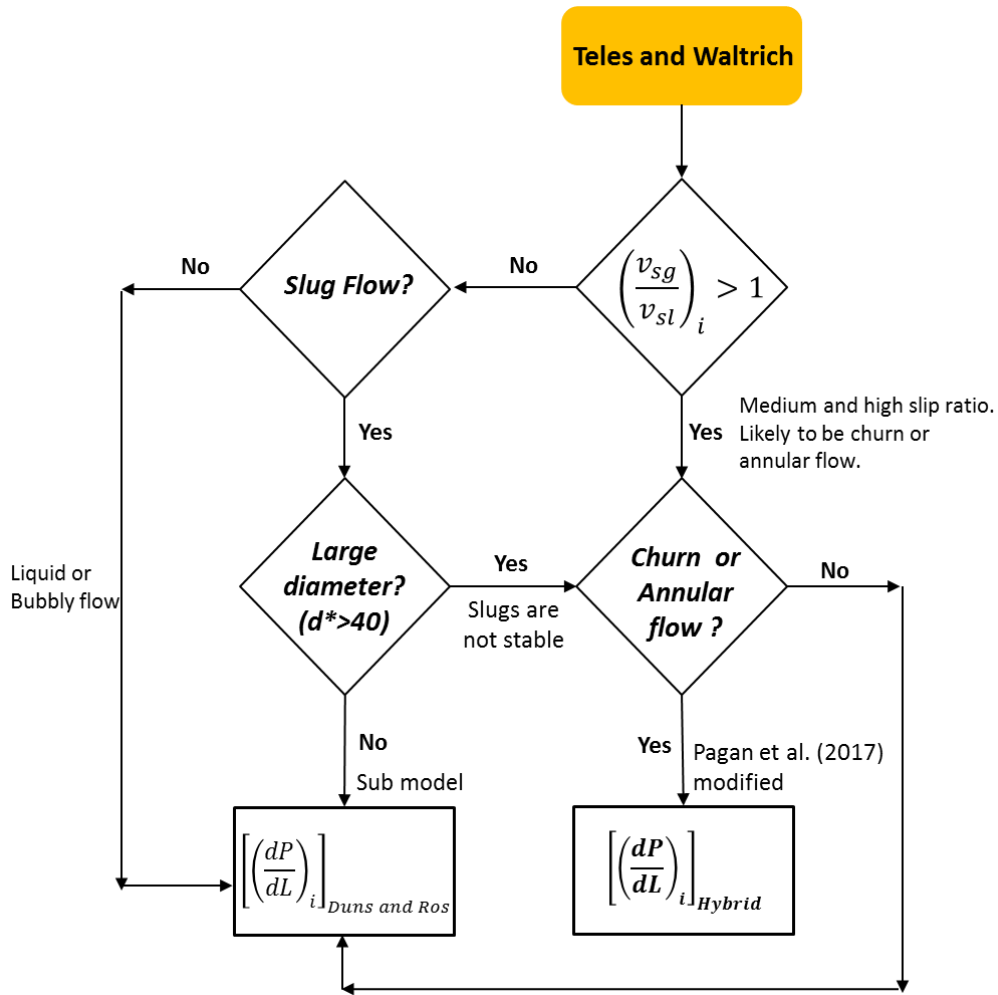


Figure 8 – Teles and Waltrich model workflow. The model uses Pagan et al. (2017) approach for churn and annular flow. The chosen sub model for bubbly and slug flow in this study is Duns and Ros (1963).

3. RESULTS AND DISCUSSION

The accuracy of Teles and Waltrich model was compared to other models often found in commercial packages used for WCD calculations. These models are:

- Beggs and Brill (1973)
- Duns and Ros (1963)
- Mukherjee and Brill (1985)
- Hagedorn and Brown (1965)
- Gray (1974)
- Ansari, Sylvester, Cem, Ovadia, and Brill (1994)
- OLGA (2000)

The results from these models are compared to field data found in the literature (Asheim, 1986); Aziz and Govier (1972); (Espanol, Holmes, & Brown, 1969; Fancher & Brown, 1963; Reinicke & Remer, 1987), and to the dataset of the experiments carried out at Louisiana State University’s PERTT Lab for a previous research project funded by BOEM (Waltrich et al., 2017 - Award M15PC00007).

A summary of the experimental and field data used in this study to evaluate the models described is shown in Table 1.

Table 1 – Source and main characteristics of the database used to evaluate the performance of the Teles and Waltrich model and other commonly used correlations.

Source	Pipe ID [in]	Liquid low rate [STB/d]	Gas-Liquid-Ratio [SCF/STB]	Fluids	Pressure [psi]
Fancher and Brown (1963)	2	75 – 936	525 – 7,283	Natural gas and oil	Up to 616
Reinicke et al. (1987)	3.98	7.5 – 493	7,734 – 1,403,645	Natural gas and water	Up to 8,880
Asheim (1986)	≈ 4, 6.2	Up to 27,700	≈ 325	Natural gas and oil	Up to 2,616
Espanol et al. (1969), Aziz and Gouvier (1972)	≈ 2.4	1,850	Up to 2,250	Natural gas and oil	Up to 5,140
PERTT Lab	4, 8, 12	Up to 29,200	Up to 887	Air and water	≈ 14.7
Petrobras	3.74, 4.5	Up to 3,665	Up to 5,720	Natural gas, oil and water	Up to 7,595

3.1 ERROR CALCULATION METHOD

The bottomhole pressure average absolute error for the results is calculated by:

$$Error (\%) = \frac{1}{n} \left(\sum_{i=1}^n |Error_{R,i}| \times 100 \right) \quad (3.1)$$

where the relative error is:

$$Error_{R,i} (\%) = \frac{BHP|_{simulated} - BHP|_{measured}}{BHP|_{measured}} \quad (3.2)$$

and n is the number of experimental or field data points. The error bars included in Figures 11, 13, 15, 17, 19, 22 are represented by the standard deviation for the average absolute error for each scenario, which is calculated using the following expression,

$$Standard\ Deviation (\%) = \sum_{i=1}^n \sqrt{\frac{(Error - Error_{R,i})^2}{n}} \quad (3.3)$$

The same procedure is applied for the LSU PERTT lab evaluation results, in this case the same the error is calculated based on pressure gradient instated of bottomhole pressure, given by,

$$Error_{R,i} (\%) = \frac{\frac{dP}{dL}|_{simulated} - \frac{dP}{dL}|_{measured}}{\frac{dP}{dL}|_{measured}} \quad (3.4)$$

3.2 MODELS RESULTS FOR REINICKE ET AL. (1987) FIELD DATA

The data base of Reinicke and Remer (1987) consists of 26 gas-water wells for tubing diameter of 3.98 in, depth ranging from about 5,577 to 16,000 ft, slightly deviated wells (no more than 8 degrees from the vertical), liquid flowrates from 7.5 to 493 BBL/D, and gas-liquid ratios ranging from 7,734 to 1,403,645 SCF/STB.

Figure 9 shows the simulated and measured bottomhole pressures for all wells using the model of Teles and Waltrich and other flow models. The simulation results shows that the simulated bottomhole pressures for Teles and Waltrich model is within $\pm 20\%$ deviation from the measured values. All other models presented errors higher than 20%, except the model of Hagedorn and Brown.

In Figure 10, the average absolute error and standard deviation of these errors for the simulation of the 24 wells of Reinicke and Remer (1987) using all flow models mentioned above are presented. These results show that for the Teles and Waltrich model, the error is within $\pm 15\%$ in relation to the field data, while for the other models the error goes up to +45%, which is the case of Duns and Ros (1963). The error for the three mechanistic models are much higher when compared to Teles and Waltrich model. The predicted flow regime using Teles and Waltrich model was churn flow for most of the wells. On the other hand Ansari et al. (1994), Beggs and Brills, and Duns and Ros predicted that most of the wells flow in slug flow regime OLGA (2000) predict some of them to be in annular flow regime as well. According to the concept of large diameter defined by Katakoa and Ishii (1987), represented by Equation 2.1, it was observed that the dimensionless diameters (d^*) for all these wells are higher than 20 (ranging from 22 to 35), leading to the conclusion that at these conditions Taylor bubbles are not stable. Thus, slug flow should not occur. Therefore, the high errors in these models are likely due to the fact of they do not considering churn flow

as a separated flow regime, and using slug flow model to determine the pressure gradient in churn flow regime. In these wells, the churn flow regime occurrence can be supported by the fact that the wells are deep, having large diameters and high pressures, conditions in which churn flow is most likely to occur, as shown in Figure 5. The fact that Hagedorn and Brown shows the second best performance for the evaluation of the field data may also corroborates the presence of churn flow. Hagedorn and Brown is not flow regime dependent and it also originally developed using experimental data for oil-gas systems. Thus, Hagedorn and Brown correlation should also incorporate the effects of surface tension showed in Figure 5, and may not include errors associated to using slug flow model as it is a flow regime independent correlation. Gray (1974) correlation for condensate gas wells provided an average absolute error of about 15%, which is lower than Ansari et al. (1994), Beggs and Brill, and Duns and Ros (1963) models.

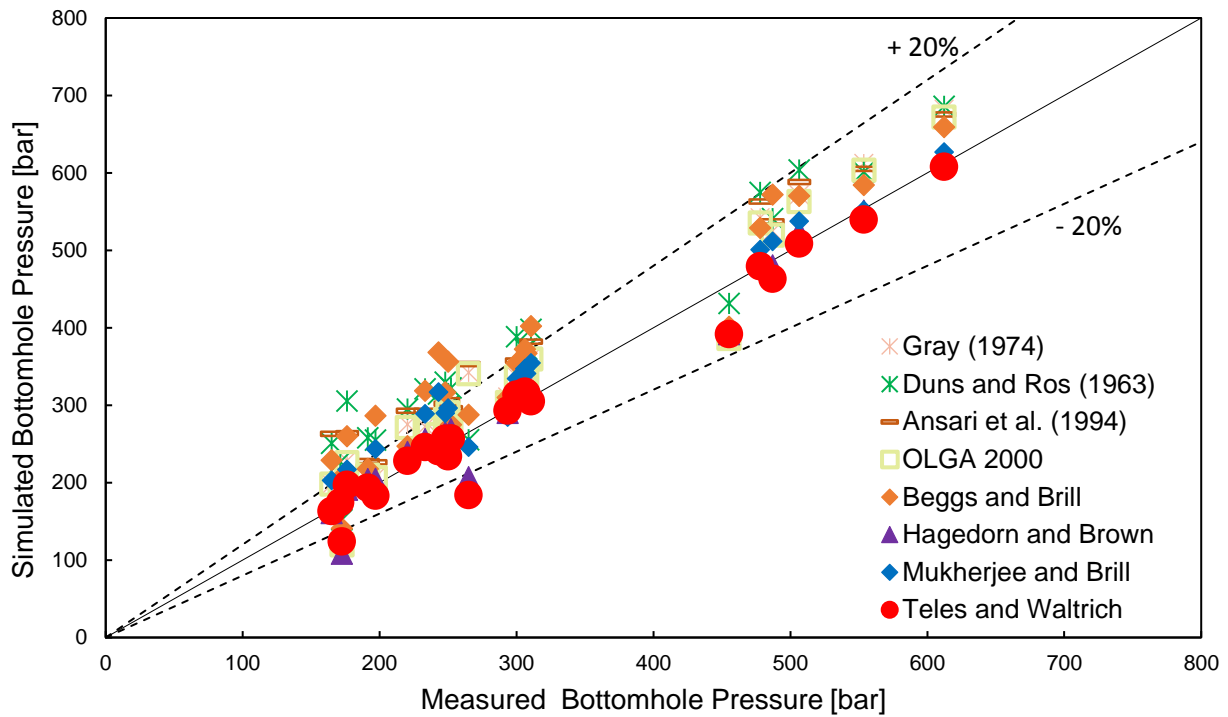


Figure 9 – Comparison of field bottomhole pressure and simulated bottomhole pressure for Teles and Waltrich; Gray (1974); Duns a Ros (1963); Ansari et al. (1994); OPGA (2000); Beggs and Brill; Mukherjee and Brill; Hagedorn and Brown. The black dash lines represent the error line for $\pm 20\%$ of the simulated pressure BHP.

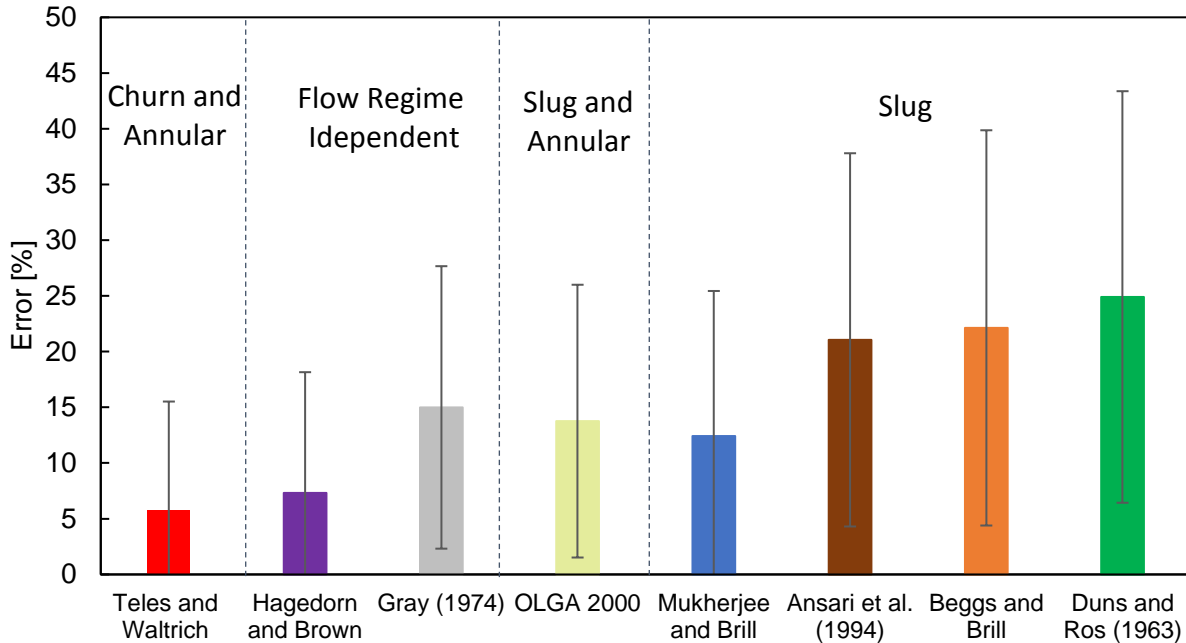


Figure 10 – Average absolute error and standard deviation of the errors for Teles and Waltrich; OLGA (2000); Gray (1974); Ansari et al. (1994); Beggs and Brill; Hagedorn, Mukherjee and Brill; Brown, Duns and Ros (1963). The columns represent the average absolute error and the line intervals the standard deviations.

3.3 EVALUATION OF TWO-PHASE FLOW MODELS FOR LOUISIANA STATE UNIVERSITY'S PERTT LAB EXPERIMENTS

An experimental campaign was carried out at Louisiana State University's PERTT Lab to cover large diameter pipes and high liquid and gas velocity flows. The data from this data set includes 130 tests conducted for diameters 3.82, 7.80, and 11.7 in. The fluids used were air and water, the liquid superficial velocities range from 0.30 ft/s up to 14.3 ft/s, and air superficial velocities from 0.23 ft/s up to 103.6 ft/s. In some of the tests, the flow regimes were observed with a high speed camera. The data collected from those experiments were reported by Waltrich et al. (2017) and will be used in this work to evaluate the accuracy of the Teles and Waltrich model. Figure 11(a) to 11(f) present the vertical lift performance curves generated by this model for each liquid superficial velocity.

Teles and Waltrich model shows a reasonable match for low superficial velocities which are the cases from Figure 11(a) and 11(b) for all diameters, and Figure 11(c) for 4 and 12 in. For higher liquid velocities the model under predicted the pressure gradient for high gas velocities, while for low liquid superficial velocities the model overestimated the pressure gradient. It was observed that for large pipe diameters, the model in this study also showed a performance similar to the Hagedorn and Brown model for all tests, with errors from around 30% and up to 50%.

Figure 12(a) to 12(e) shown the results of the errors of pressure gradient for different levels of gas-liquid superficial velocity (slip) ratios for Teles and Waltrich, Duns and Ros, Beggs and Briil, Mukherjee and Brill, and Hagedorn and Brown models. It can be observed that for low slip ratio ($v_{sg}/v_{sl} < 1$) all models have lower errors, therefore a good agreement with the experimental data. For medium slip ratio ($1 < v_{sg}/v_{sl} < 100$) the errors are higher for all models, except for Hagedorn and Brown. The high slip ratios ($v_{sg}/v_{sl} > 100$) are the ones with the highest errors, going up to more than 100% for Teles and Waltrich model. Figure 13 illustrates the average absolute error of pressure gradient for the 4, 8, and 12 in pipes for Teles and Waltrich, Duns and Ros, Beggs and Briil, Mukherjee and Brill, and Hagedorn and Brown. In addition, Figure 14 shows the overall average absolute error of pressure gradient for all models mentioned.

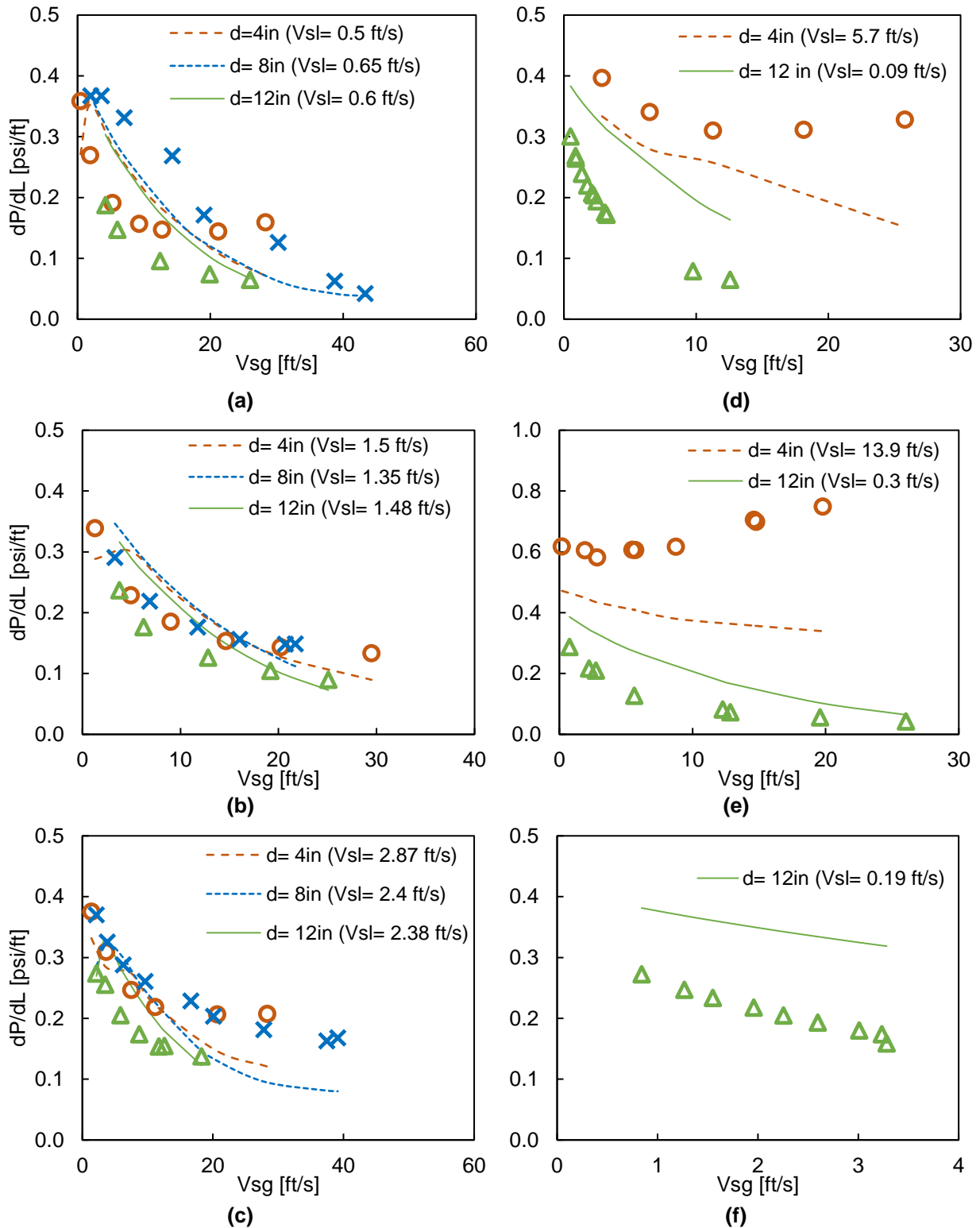


Figure 11 – Comparison between Teles and Waltrich model and experimental results in terms of pressure gradient versus gas superficial velocities for 4, 8, and 12 in pipe diameter and superficial liquid velocities from 0.09 to 13.9 ft/s (Figures 10a to 10f).

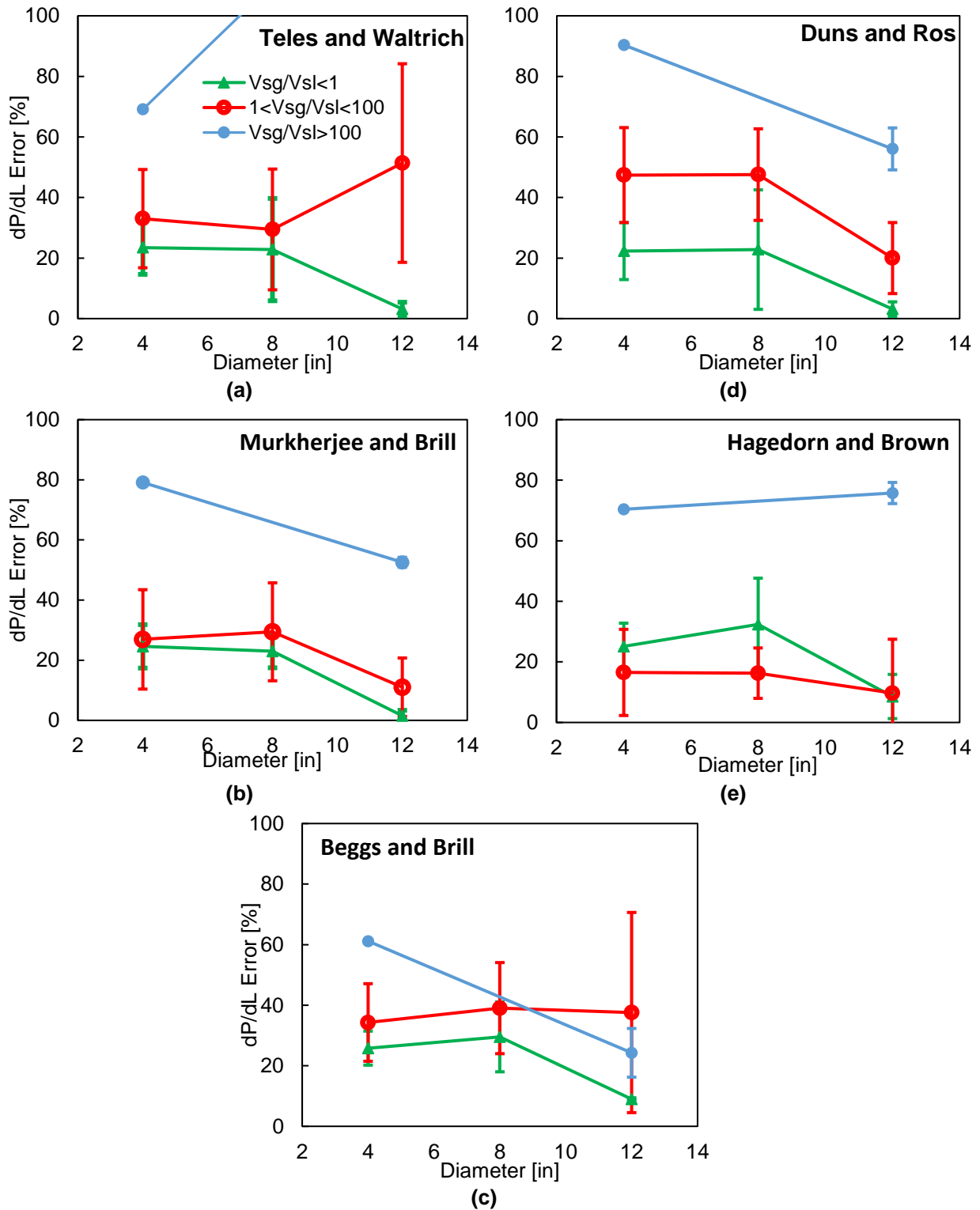


Figure 12 – Comparison errors of pressure gradient in terms of slip velocity for 4, 8, and 12 in pipe diameter for Teles and Waltrich, Duns and Ros, Beggs and Brill, Murkherjee and Brill, and Hagedorn and Brown models. Green curves represents scenarios having: slip ratio less than one; red curves: slip ratio between one and 100; blue curves: slip ratio greater than 100.

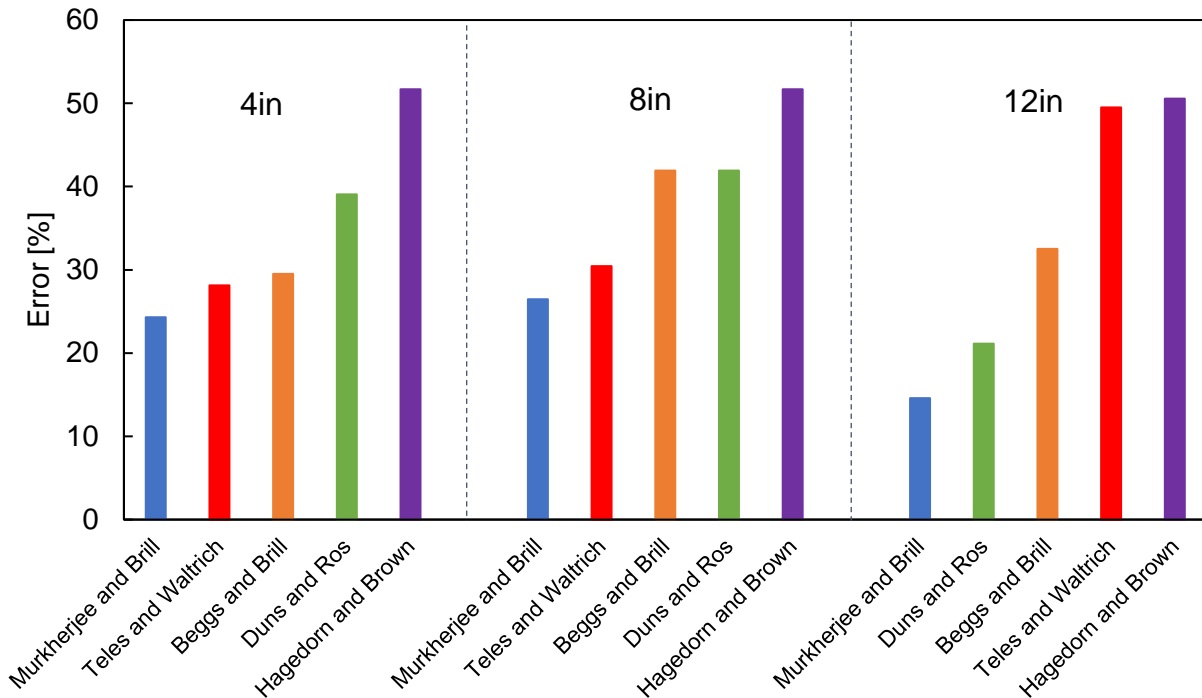


Figure 13 – Average Absolute Error of pressure gradient in % for Teles and Waltrich, Duns and Ros, Beggs and Brill, Murkherjee and Brill, and Hagedorn and Brown models for 4, 8, and 12in for the LSU/PERTT Lab experimental data reported by Waltrich et al. (2017).

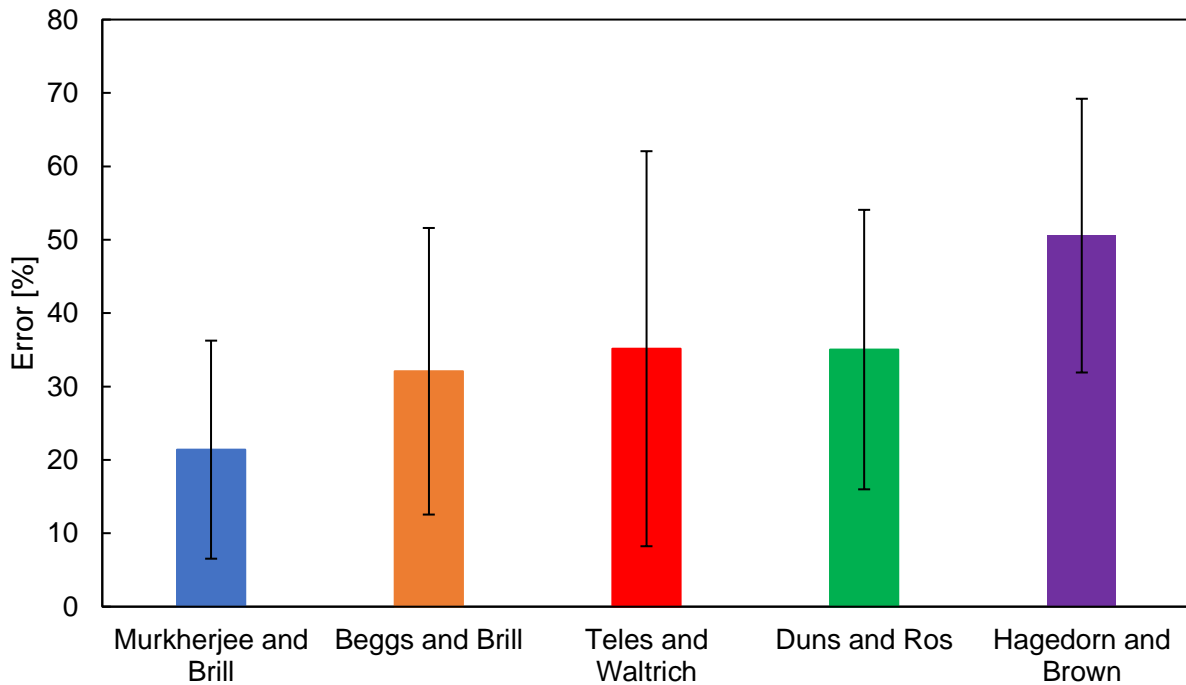


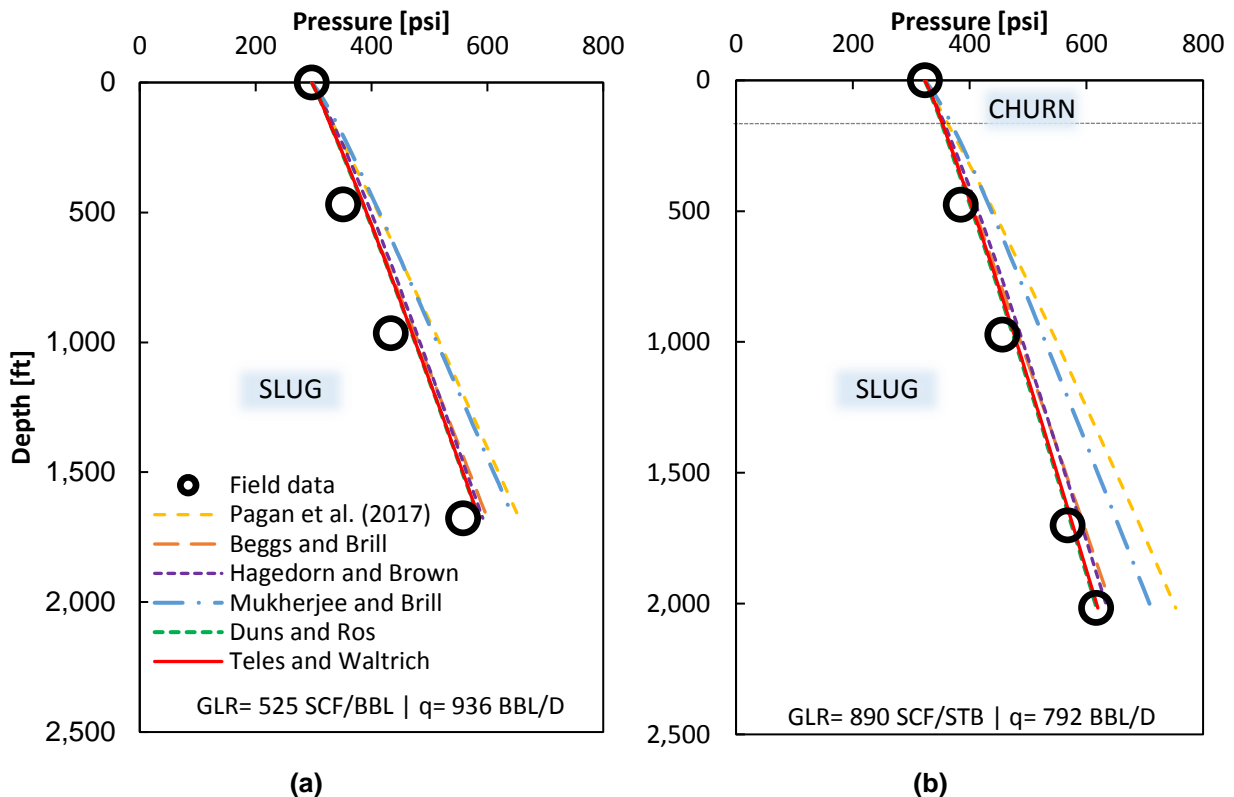
Figure 14 – Overall average absolute error of pressure gradient in % for Teles and Waltrich, Duns and Ros, Beggs and Brill, Mukherjee and Brill, and Hagedorn and Brown models for for the LSU/PERTT Lab experimental data reported by Waltrich et al. (2017)..

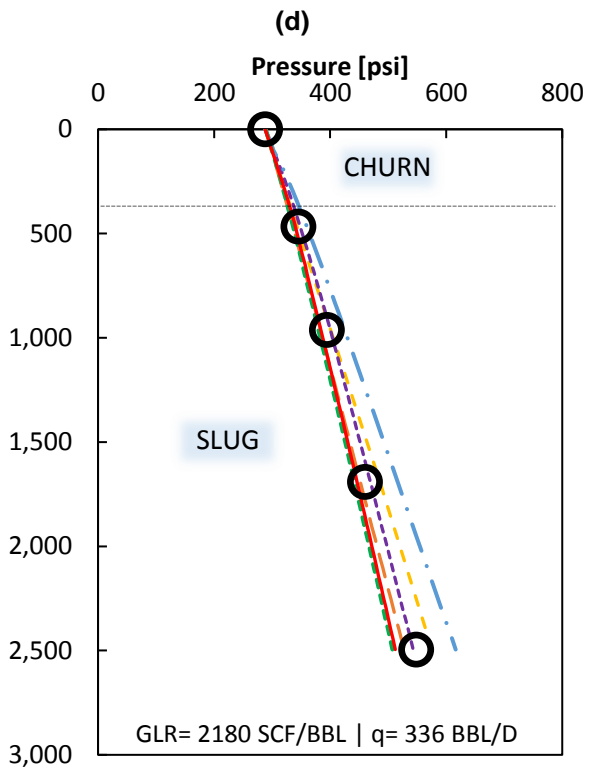
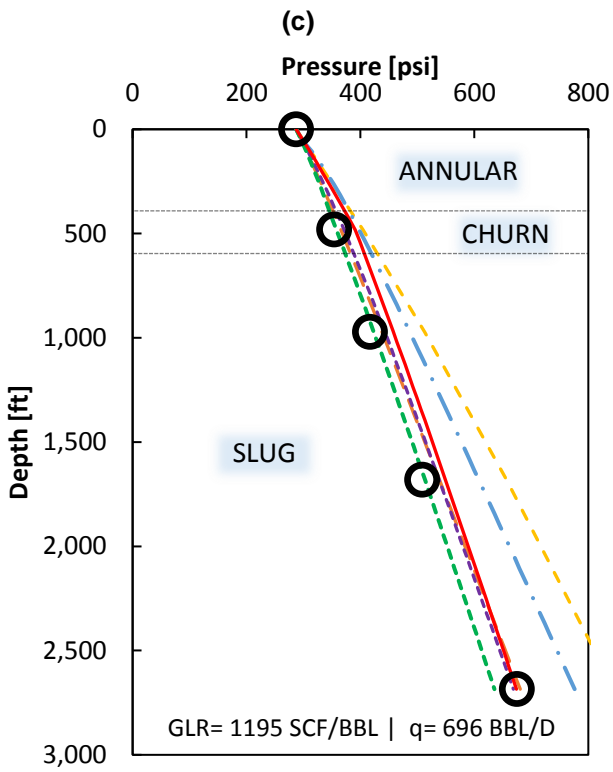
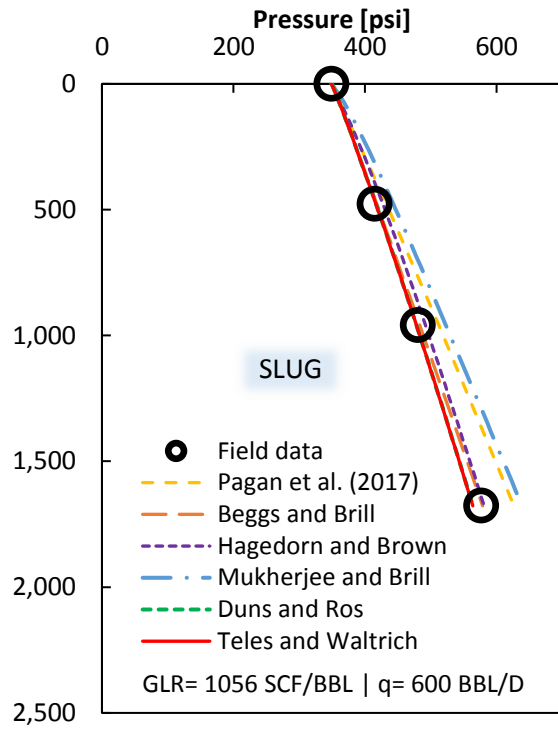
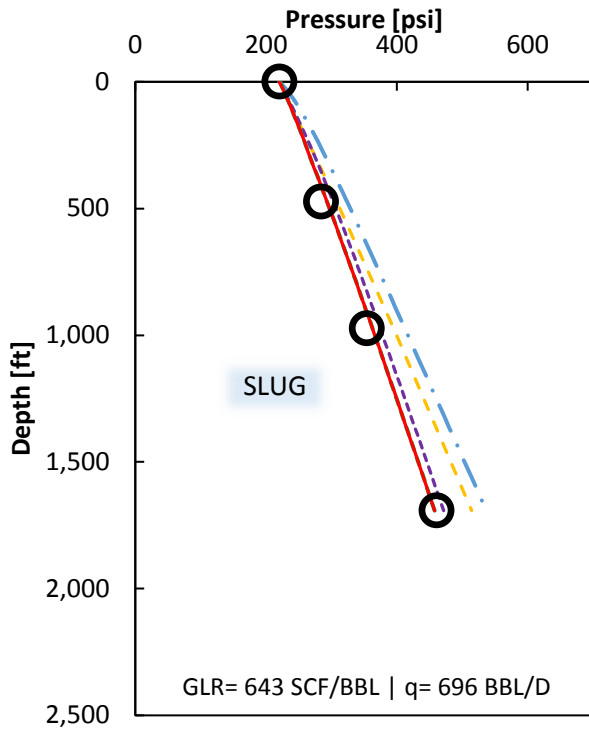
Interestingly, as shown in Figure 13, three of the models evaluated for this database showed lower error for the 12 in pipe. For this pipe diameter, the error of Teles and Waltrich model is the second largest one, being about 50%. Looking at overall average error in Figure 14, the hybrid model shows a relatively high error when predicting pressure gradient. Further investigation should be done for this experimental set of data. It was expected the proposed model to have the best results, since it is differently from the other models, Teles and Waltrich is for large diameter and high flow rates. It is important to mention that the flow regime prediction from Teles and Waltrich model agreed with the flow regime recorded by the high speed camera being most of them churn and annular flow.

3.4 EVALUATION OF TWO-PHASE FLOW MODELS FOR FANCHER AND BROWN (1986) FIELD DATA

Fancher and Brown (1986) conducted tests in an 8,000 ft vertical well with 2 in ID. The tested liquid flow rates range from 75 to 936 BBL/D, and GLRs from 525 to 7,283 SCF/BBL. The gas rates were set by the continuous injection of a gas with specific gravity of 0.57 through a gas lift valve located at 2,774 ft in the well. The produced oil has 34 API gravity of at 60 °F, and the produced rates were controlled by a downhole choke. A linear profile of fluid temperature was assumed from the bottomhole to the wellhead. The pressure profile along 12 wells were predicted using the Pagan et al. (2017); Beggs and Brill; Duns and Ros; Mukherjee and Brill; Hagedorn and Brown; and the proposed hybrid model. Figure 15(a) to 15(m) show the comparison between the results obtained with these models and the field data.

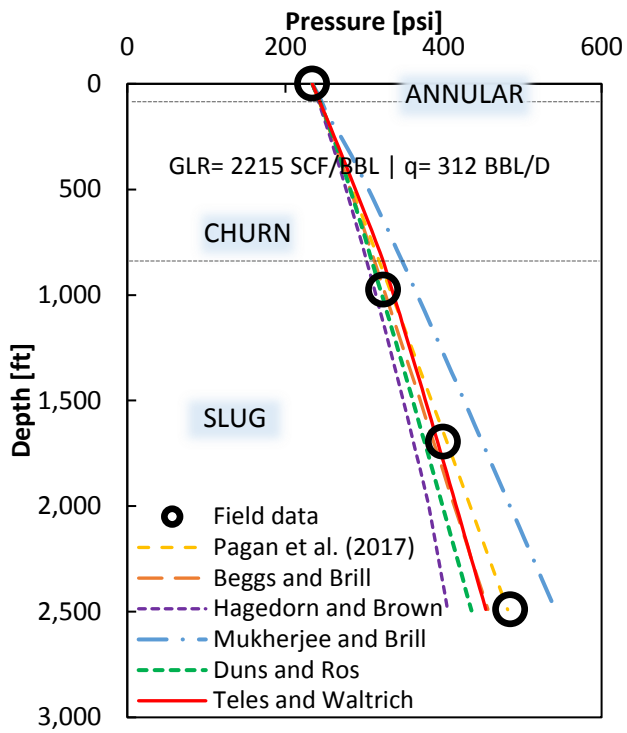
Teles and Waltrich model showed a reasonable fit to the field data of Fancher and Brown (1986). From the graphs below, for high GLR this model has a better fit than the other models, since at high flowrates of gas flow regime is more likely to be either churn or annular. It was also observed that for a liquid rate of 144 BBL/D, when GLR increases Beggs and Brill and Hagedorn and Brown deviate from the field data trend. This is probably due to the fact that this first does not consider churn flow and Hagedorn and brown is independent of flow regime, what lead to higher errors when predicting the pressure gradient in either churn or annular flow conditions. Mukherjee and Brill shows a deviation from the field data for most of the cases, while Duns and Ros model provides a good fit mainly for the slug flow conditions.



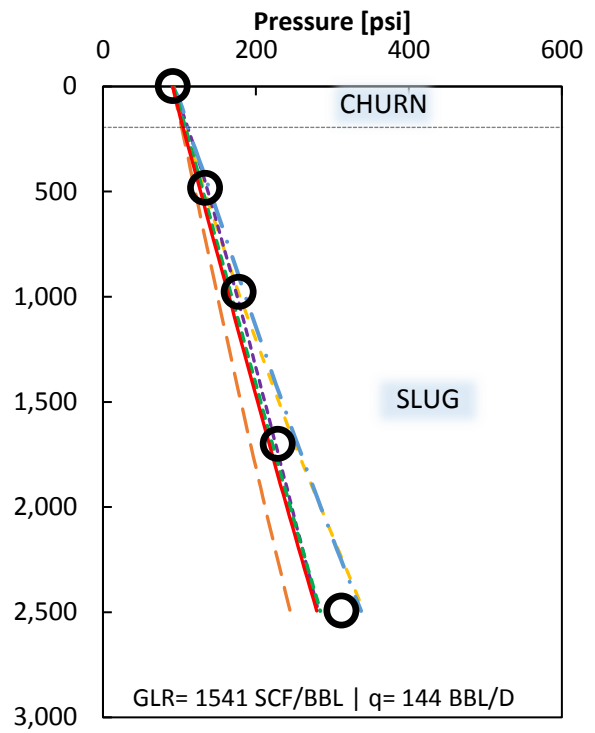


(e)

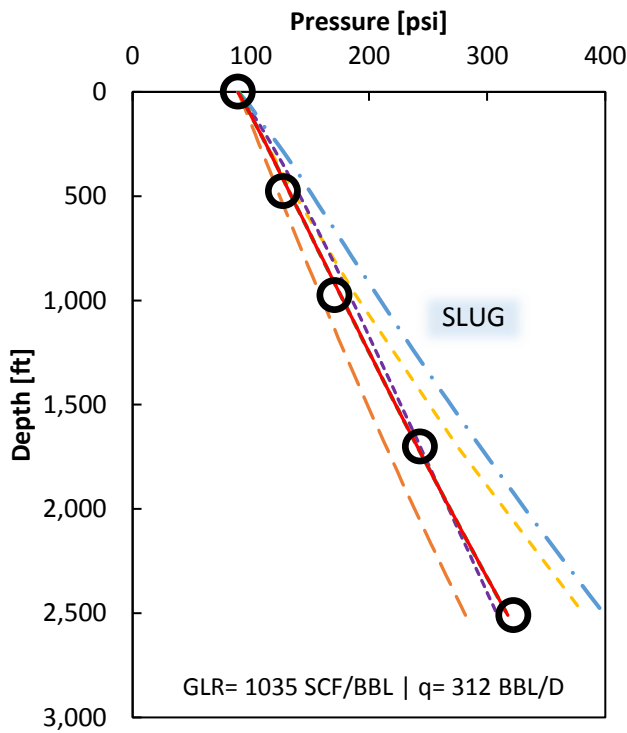
(f)



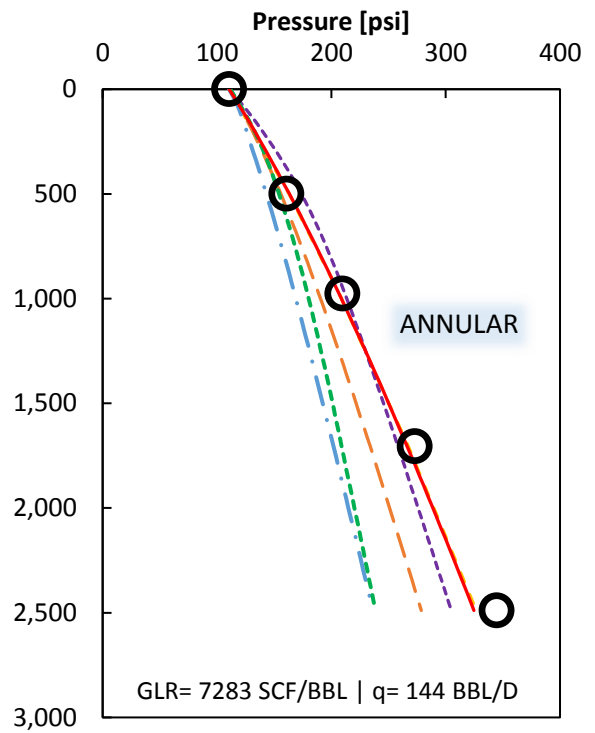
(g)



(h)



(i)



(j)

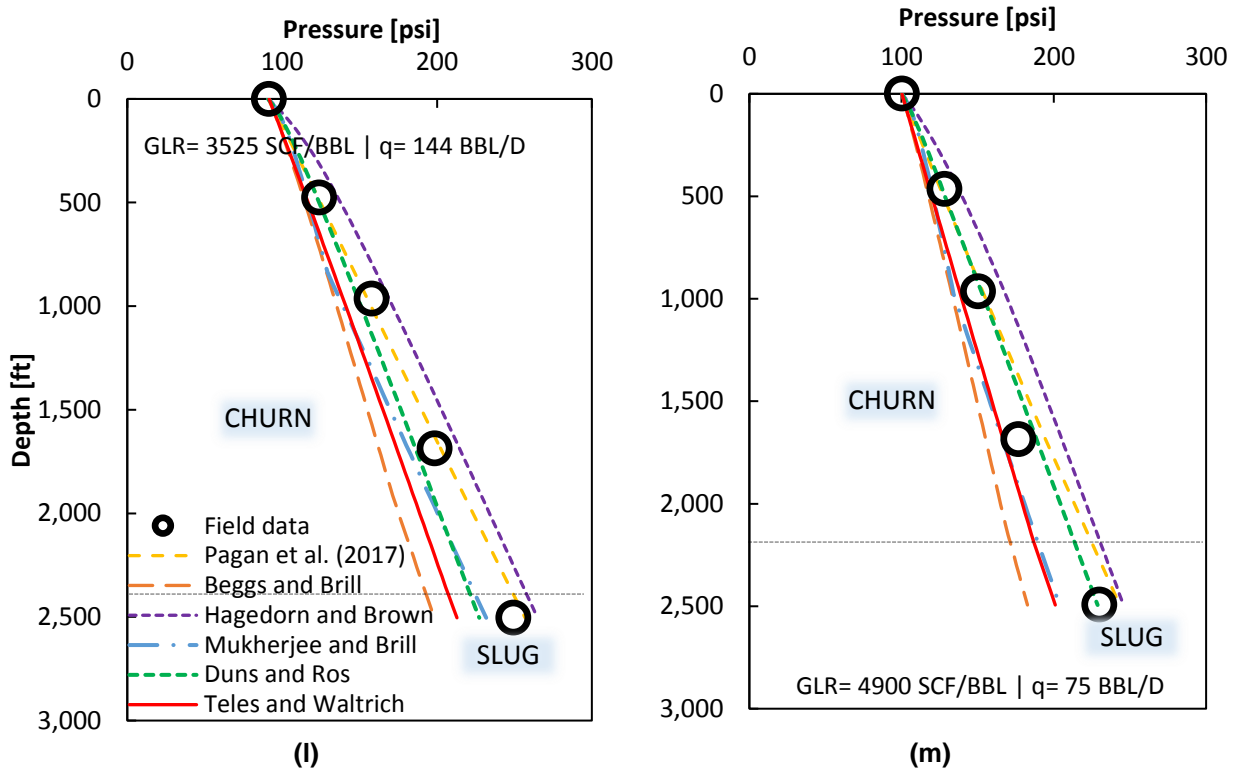


Figure 15 – Comparison between simulation results using the model proposed in this study and measured wellbore pressure profile (field data from Fancher and Brown, 1963). Circles represent the measured pressures and continuous lines are the simulated pressures. The horizontal dash lines represent the transition of flow regime along the well.

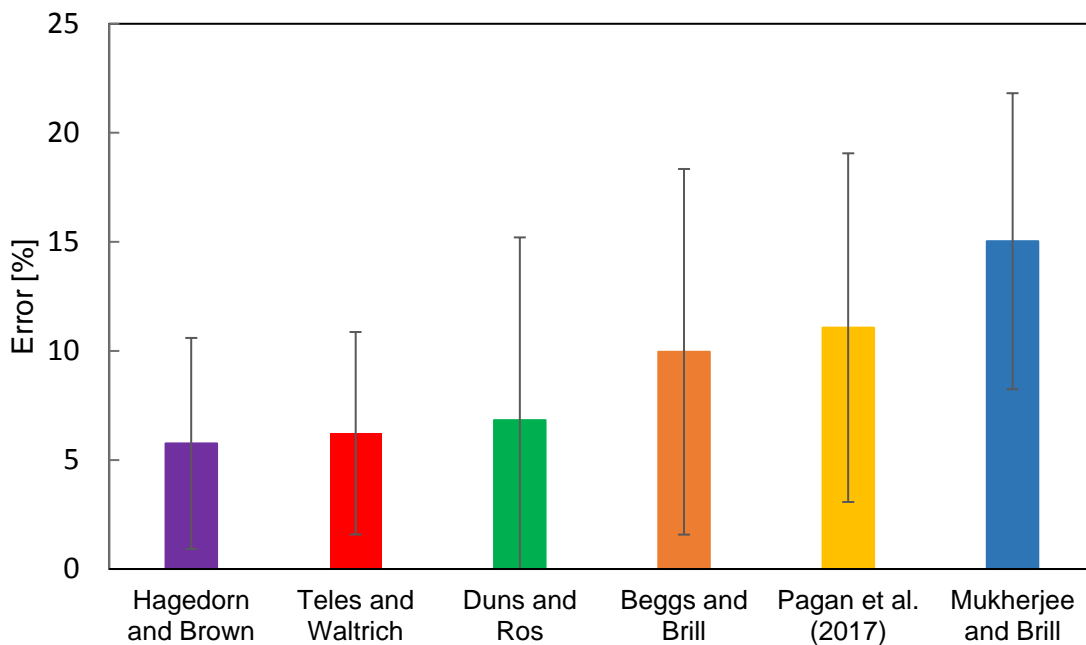


Figure 16 – Average absolute error of the simulated bottomhole pressure for Teles and Waltrich, Hagedorn and Brown, Mukherjee and Brill, Beggs and Brill, Duns and Ros, and Pagan et al. (2016), for Fancher and Brown (1963) field data. The standard deviation of the errors are represented by the error bars on each model.

A comparison of the average absolute error of simulated bottomhole pressure for the 12 wells is given in Figure 16. It was observed that Teles and Waltrich model had an average absolute error very similar to Hagedorn and Brown, up to 11% (standard deviation bar) in wells with low GLR. On the other hand, for high gas-liquid ratio scenarios, where churn flow and annular flow were predicted, the errors for Teles and Waltrich model were lower than 1%. This model had the second lowest average absolute error for the 12 wells. Duns and Ros shows a similar average absolute error, but higher standard deviation due to the high error in some higher GLR scenarios. Differently from the experimental data analysis of air-water systems from the previous section, for this field data, Mukherjee and Brill model had the highest error.

3.5 EVALUATION OF TELES AND WALTRICH MODEL FOR DEVIATED WELLS FROM ASHEIM (1986) FIELD DATA

The field data from the Forties Field were used to evaluate the accuracy of the proposed hybrid model for wells deviated up to 46 degrees with the vertical. The set of data from Asheim (1986) consists of 37 runs in an oil and gas well, with oil rates from 6,540 to 27,270 STB/D and GOR of 337 SFC/STB for the 6.184 in ID and 323 SCF/STB for the 3.958 in ID wells. For all runs, the oil and gas specific gravity are 0.84 and 1.1, respectively. The depth of the point of pressure measurement varies from 6,900 ft to 10,300 ft. Figure 17 shows the comparison of measured and simulated bottomhole pressure for the 37 scenarios. It should be noted that the error of the simulated BHP is within $\pm 20\%$.

The purpose of this analysis is to also evaluate pressure drop for large diameter piper for more field data. This system includes field data with wellbore flowing oil and natural gas, moderate high flow rates. The simulated data showed good agreement with the field data, and the error in the prediction using the simulator is consistent.

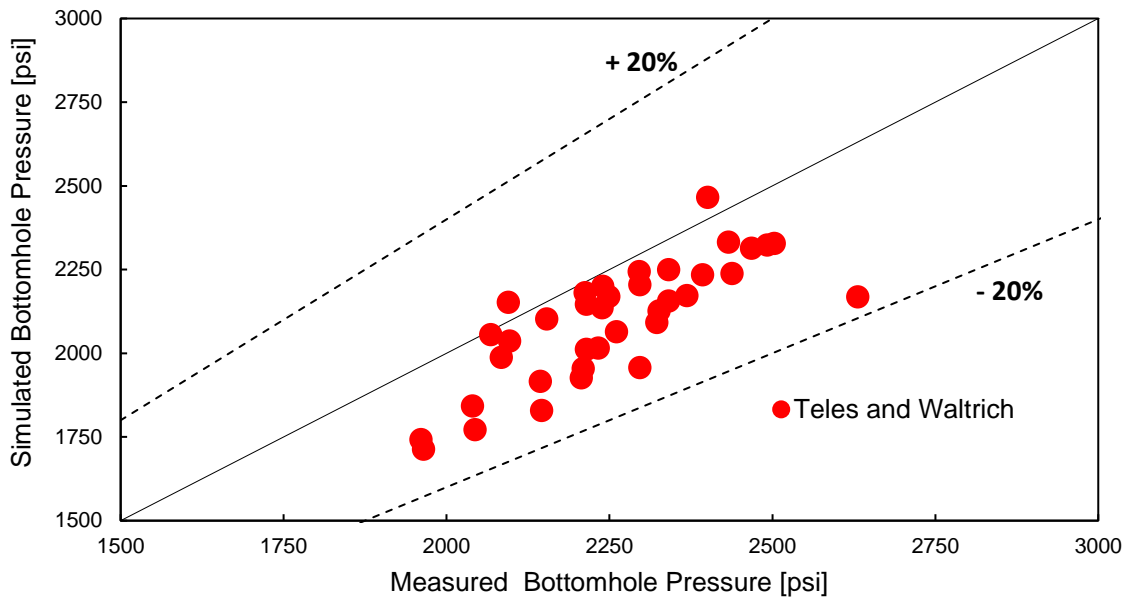


Figure 17 – Comparison of field bottomhole pressure and simulated bottomhole pressure for Teles and Waltrich for 34 well in Forties field from Asheim (1986). The black dash lines represent the error line for $\pm 20\%$ of the simulated pressure BHP.

Besides Teles and Waltrich model, this set of data for inclined well from Asheim (1986) was also simulated for other models: Mukherjee and Brill, Duns and Ros, Beggs and Brill, and Hagedorn and Brown. Figure 18 shows the comparison of the average absolute error for all these models. Teles and Waltrich model has a good agreement with the field data, having an average absolute error of about 6.5 % (represented by the red box). This model had similar results from Beggs and Brill, which already is a widely used model for deviated wells. Hagedorn and Brown provides a higher error for these simulations.

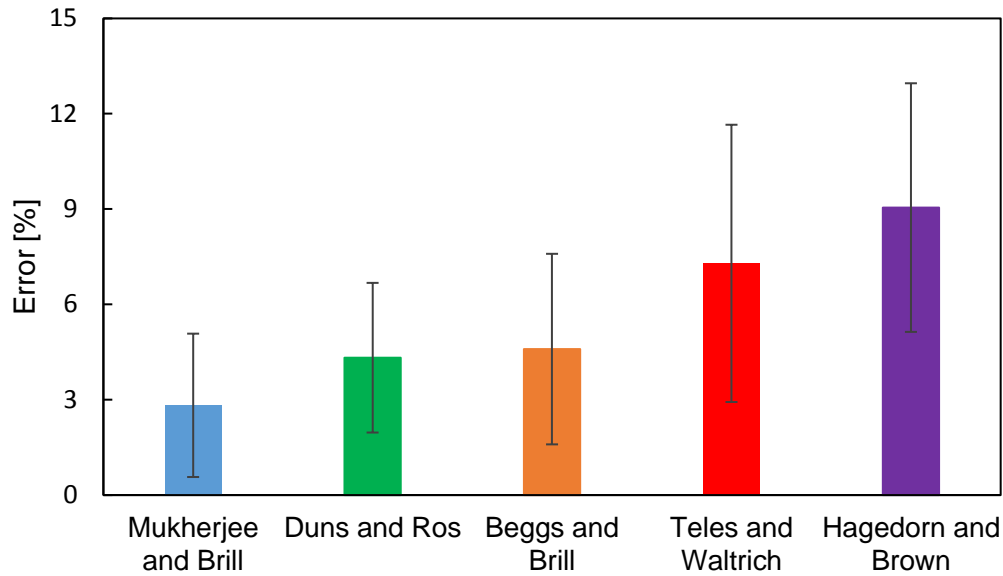


Figure 18 – Average absolute error of the simulated bottomhole pressure for Teles and Waltrich, Mukherjee and Brill, Hagedorn and Brown, Beggs and Brill, and Duns and Ros for Asheim (1986) field data. The standard deviation of the errors are represented by the error bars on each model.

3.6 EVALUATION OF TELES AND WALTRICH MODEL USING FIELD DATA FROM ESPANOL ET AL. (1969) and AZIZ AND GOVIER (1972).

This database consists of 44 tests performed in a 2.376 in ID well flowing with oil rates up to 1,656 BBL/D and gas-oil ratios from 171 to 9,975 SCF/BBL. These data were reported by Aziz and Govier (1972), and most field data comes from Espanol et al. (1989). For these oil wells the API gravity ranges from 18 to 44 and depth goes up to 12,450 ft. Figure 19 shows preliminary results for the evaluation of Teles and Waltrich model for 8 out of the 48 wells. It was observed that the simulated values of bottomhole pressures are close to the measured values, with the highest error of 14.3%. For these field data, the flow regimes are mostly bubbly and slug flow, the dimensionless dimeters are lower 18.5. Therefore further investigation and comparison of empirical and mechanistic models are not going to be carried since the churn flow condition is not present.

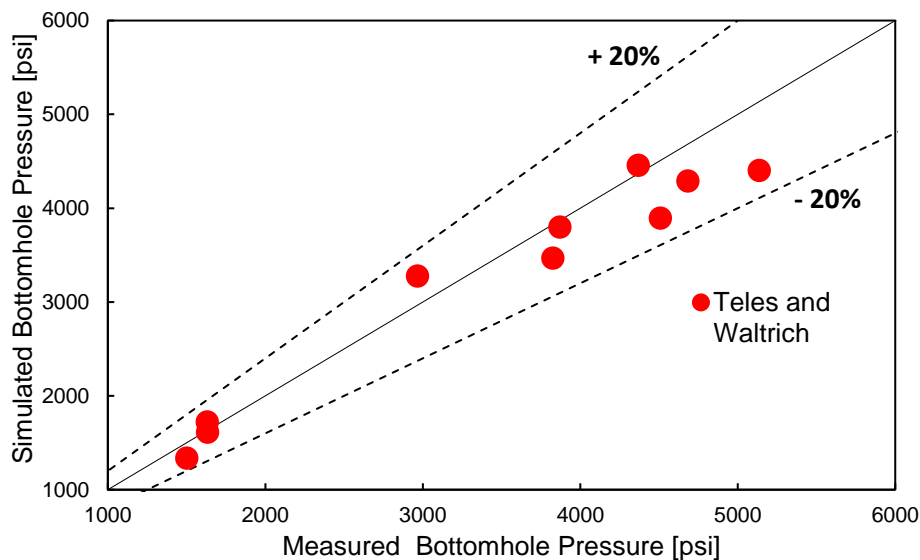


Figure 19 – Comparison of field bottomhole pressure and simulated bottomhole pressure for Teles and Waltrich for Espanol et al. (1989) data set. The black dash lines represent the error line for $\pm 20\%$ of the simulated pressure BHP.

3.7 PETROBRAS AMERICA

This data consists of twenty different production and pressure data for steady state periods of production for three condensate gas wells in the Gulf of Mexico. These wells have diameters of 3.74 and 4.5 in. Gas Liquid Ratio are up to 5,720 SCF/STB with bottomhole pressure up to 7,595 psi. The results of the average absolute error of the simulated bottomhole pressure for Teles and Waltrich; Hagedorn and Brown; Beggs and Brill; Mukherjee and Brill; and Dun and Ros model for the three wells separately are shown in Figure 20.

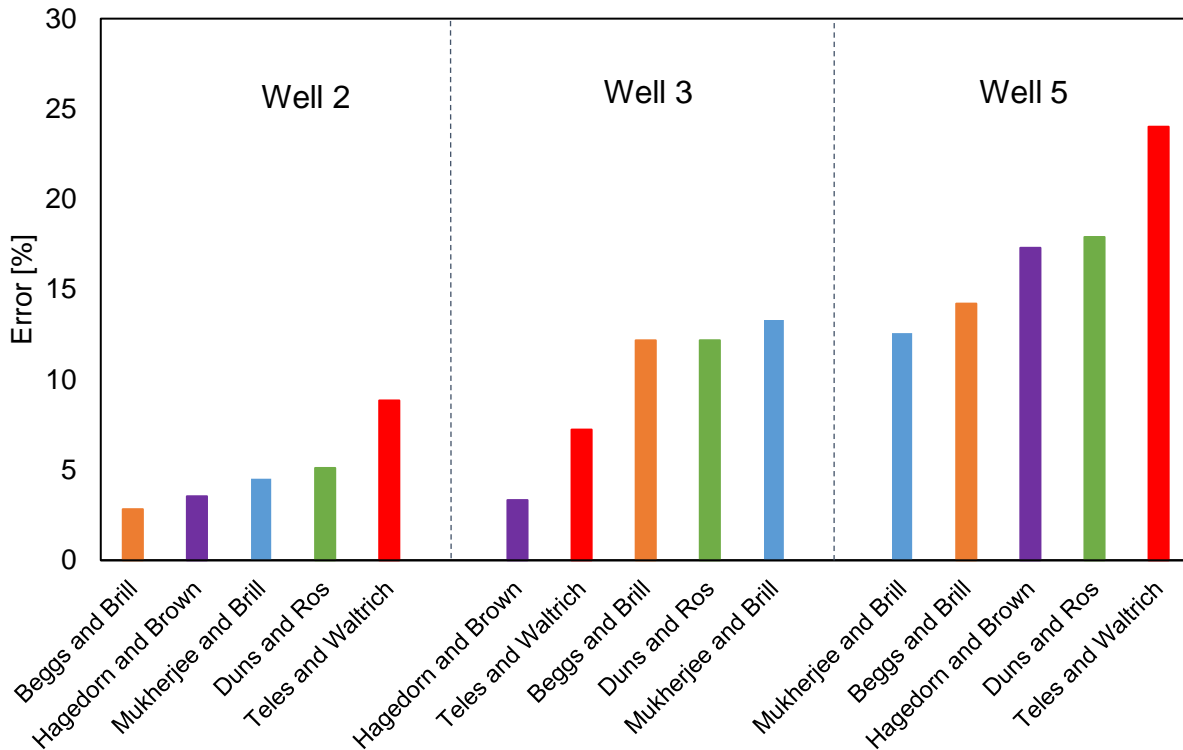


Figure 20 – Average absolute error of the simulated bottomhole pressure of the three different wells for Teles and Waltrich; Mukherjee and Brill; Hagedorn and Brown; Beggs and Brill; and Duns and Ros for Petrobras’ field data.

These simulations for Wells 5 resulted mostly bubbly and intermittent flow for the Duns and Ros; Beggs and Brill; and Mukherjee and Brill models. The gas and liquid superficial velocities for this well are as large as 1.6 ft/s, which according to previous simulations and analysis might not be enough for reaching the turbulence required in churn or annular flow regimes. The hybrid model predicted to have either churn or annular flow close to the wellhead and then bubbly flow, having significant change in pressure gradient from one flow regime to the other. In this case the bottomhole pressure was over predicted and the error for Teles and Waltrich model was the highest (up to 24%). Well 2 has higher GLRs, and the presence of churn flow all along the well was observed in a couple cases. Most of scenarios have a transition from churn to bubbly flow. The overall average absolute error for well number 2 ranges from ~4% for Hagedorn and Brown to ~9% for Teles and Waltrich.

For Well 3, Teles and Waltrich predicted to have bubbly, churn flow or churn/bubbly for all scenarios. Differently from Wells 2 and 5, this well reached GLR as high as 5,720 SCF/STB and water-cut up to 37%. The flow conditions for this well have the highest GLRs of Petrobras data set, having liquid and gas superficial velocities up to ~ 4ft/s. The hybrid model showed an average absolute error of up to 7%, the second lowest error for this well. Beggs and Brill; Duns and Ros; and Mukherjee and Brill predicted the flow regime to be either Slug/Bubbly or Slug for almost all simulations and they all have average absolute

errors of about ~12.5%. The literature reports that these three models over predict the pressure gradient for GLR higher than 5,000 SCF/STB and/or presence of water.

In some of the flow conditions for these wells, it was observed convergence errors, and discrepancies on the pressure gradient and flow regime prediction. A modified Duns and Ros flow regime map accounting for the concept of nonexistence of slug flow in large diameter wells was used to perform the simulations for Petrobras America data set. This flow regime map was used for the fact that it was validated for diameters higher than 4.5 in as well as with hydrocarbon fluids. Further investigation should be done in the simulations of this data set regarding the flow regime map.

Figure 21 shows the overall average absolute error for all simulations together. It is observed that overall the Hybrid model has an error of 10%, similar error are shown for Beggs and Brill; Duns and Ros; and Mukherjee and Brill models. This overall error for Teles and Waltrich model results mainly from the simulations of well 5, where the average absolute error was ~24%. The simulations for Petrobras data set evidenced the improvements on the applicability of the Hybrid model for high GLR well, as observed for well 3.

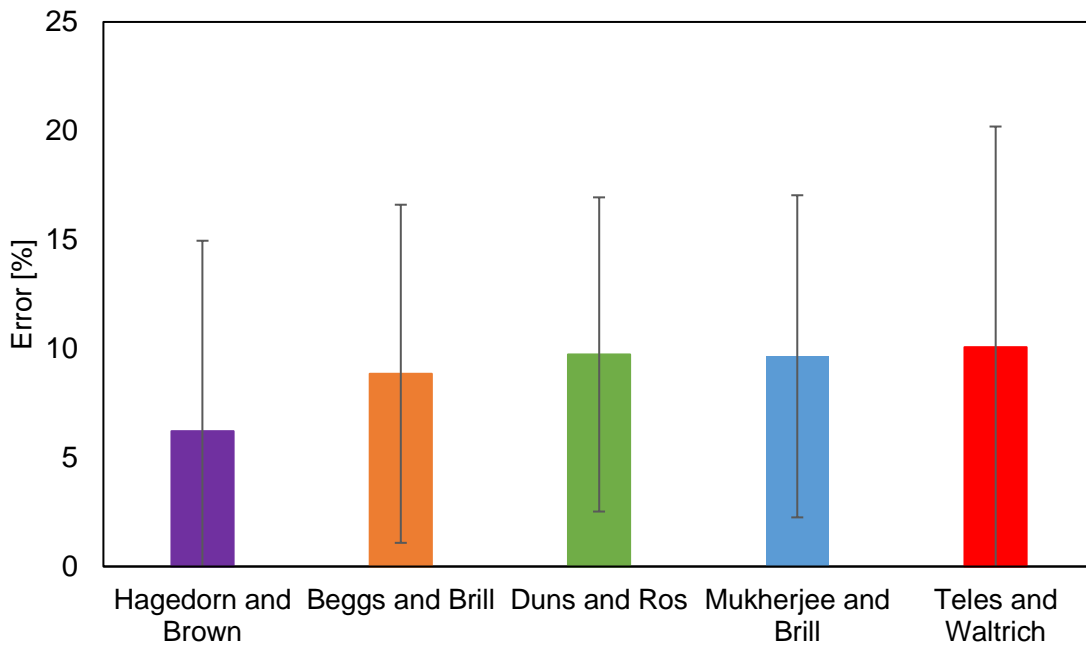


Figure 21 – Overall average absolute error of the simulated bottomhole pressure for Teles and Waltrich, Mukherjee and Brill, Hagedorn and Brown, Beggs and Brill, and Duns and Ros for Petrobras’ field data. The standard deviation of the errors are represented by the error bars on each model.

4. CONCLUSIONS

- For the field data of high gas-liquid-ratio flows, Teles and Waltrich model showed a better performance than the other empirical and mechanistic models such as OLGA (2000), Gray, Beggs and Brill, Mukherjee and Brill, Duns and Ros, and Hagedorn and Brown. Average absolute error for Teles and Waltrich was about 5% while for the other flow regime dependent models it was up to 25%.
- With Reinicke and Remer (1987) data set evaluation, it was concluded that considering slug flow when there is churn flow leads to significant errors. Therefore, churn flow needs to be modeled separately in order to obtain accurate results. Hagedorn and Brown, as a flow regime independent model, has low errors. However, this model was not accurate when evaluating the other field and experimental data.
- Teles and Waltrich model has a reasonable accuracy for two-phase flow in inclined wells. This model only underestimates the bottomhole pressure by at most 17% for a 20 degrees deviated well.
- For the experimental results from PERTT Lab, Teles and Waltrich model did not show an accuracy as good as Mukherjee and Brill, Beggs and Brill, Duns and Ros. The average absolute error of pressure gradient was around 35%. As the other models Teles and Waltrich also showed higher errors for pressured gradient prediction in scenarios with slip ratio greater than one unit. This can also be observed in the pressure gradient versus gas superficial velocity plots when simulated pressure starts deviating from measured pressure for higher gas superficial velocities. The results of the analysis of experimental data (air-water) from PERTT Lab were not as expected for Teles and Waltrich model. It was observed that this model had an excellent accuracy for field data (oil-natural gas and water-natural gas), what leads us to investigate more the set of data and simulations performed for the experimental case.
- The hybrid model showed reasonable results for the investigations of Petrobras America data set having average absolute error of 10%. It was observed that the presented model has better performance when calculating pressure gradient for high GLR, as for well 3.
- These simulations evidenced that empirical models might provide erroneously results when the flow conditions is out of the applicability range (i.e. GLR and water cut), as shown in Beggs and Brill and Duns and Ros results for well 3 in Petrobras data.
- Hagedorn and Brown shows good results for most of the vertical wells, smaller diameter, and lower liquid velocities scenarios. However, this model has limitations regarding these parameters, and higher errors for PERTT lab, Asheim (1986), well 5 for Petrobras data were observed.
- The LSU Multiphase Flow Simulator showed to be a good tool to analyze pressure drop along well and flow regime changes. Not only this, it can be used to investigate and compare the results with other widely used empirical correlations.
- More study should be carried out regarding the flow regime map for large diameter wells and friction factor calculation for high velocities conditions.

5. REFERENCES

- Ali, S. F. (2009). *Two phase flow in large diameter vertical riser*. (PhD), Cranfield University, School of Engineering, Department of Process and System Engineering,
- Ali Shazia, F., & Yeung, H. (2013). Two-phase flow patterns in large diameter vertical pipes. *Asia-Pacific Journal of Chemical Engineering*, 9(1), 105-116. doi:10.1002/apj.1750
- Alves, M. V. C. (2014). *Modelagem Numerica do Escoamento Transient Churn-Annular em Tubulacoes Verticais e sua Aplicacao na Simulacao de Carga de Liquido em Pocos de Gas*. Universidade Federal de Santa Catarina, Florianopolis, Santa Catarina
- Ansari, A. M., Sylvester, N. D., Cem, S., Ovadia, S., & Brill, J. P. (1994). Supplement to SPE 20630, A Comprehensive Mechanistic Model for Upward Two-Phase Flow in Wellbores. In: Society of Petroleum Engineers.
- Asheim, H. (1986). MONA, An Accurate Two-Phase Well Flow Model Based on Phase Slippage. doi:10.2118/12989-PA
- Aziz, K., & Govier, G. W. (1972). Pressure Drop In Wells Producing Oil And Gas. doi:10.2118/72-03-04
- Baker, O., & Swerdloff, W. (1956). Calculation of Surface Tension 6 - Finding Surface Tension of Hydrocarbon Liquids. *Oil and Gas Journal*, 125.
- Beggs, D. H., & Brill, J. P. (1973). A Study of Two-Phase Flow in Inclined Pipes. doi:10.2118/4007-PA
- Bharathan, D., Richter, H. J., & Wallis, G. B. (1978). *Air-water counter-current annular flow in vertical tubes*. Report EPBI-NP-786. Retrieved from
- Brill, J. P., & Mukherjee, H. K. (1999). *Multiphase Flow in Wells*: Henry L. Doherty Memorial Fund of AIME, Society of Petroleum Engineers.
- Buchholz, K., Krieger, A., Rowe, J., Etkin, D. S., McCay, D. F., Gearon, M. S., . . . Turner, J. (2016). *Oil Spill Response Plan (OSRP) Equipment Capabilities Review - Task 1: Worst Case Discharge Analysis*. Retrieved from
- Capovilla, M. S. (2018). *Two-Phase Flow Regime Map for Large Diameter Pipes and High Velocity Flows*. (Masters), Louisiana State University, Baton Rouge, LA.
- Capovilla, M. S., Cavalcanti de Sousa, P., & Waltrich, P. J. (2017). *Experimental investigation of vertical high-velocity two-phase flows in large-diameter pipes*. Paper presented at the 18th International Conference on Multiphase Production Technology, Cannes, France.
- Cheng, H., Hills, J. H., & Azzopardi, B. J. (1998). A study of the bubble-to-slug transition in vertical gas-liquid flow in columns of different diameter. *International Journal of Multiphase Flow*, 24(3), 431-452. doi:[https://doi.org/10.1016/S0301-9322\(97\)00067-0](https://doi.org/10.1016/S0301-9322(97)00067-0)
- Cordoba, F. A. V. (2018). *Integrated Reservoir-Wellbore Nodal Analysis Workflow for Worst Case Discharge Modeling*. (Masters), Louisiana State University, Baton Rouge, LA.
- Duns, H., Jr., & Ros, N. C. J. (1963). *Vertical flow of gas and liquid mixtures in wells*. Paper presented at the 6th World Petroleum Congress, Frankfurt am Main, Germany.
- Economides, M. J., Hill, A. D., Ehlig-Economides, C., & Zhu, D. (2012). *Petroleum Production Systems*: Pearson Education.
- Espanol, J. H., Holmes, C. S., & Brown, K. E. (1969). *A Comparison of Existing Multiphase Flow Methods for the Calculation of Pressure Drop in Vertical Wells*. Paper presented at the Fall Meeting of the Society of Petroleum Engineers of AIME, Denver, Colorado.
- Fancher, G. H., Jr., & Brown, K. E. (1963). Prediction of Pressure Gradients for Multiphase Flow in Tubing. doi:10.2118/440-PA
- Gray, H. E. (1974). *Vertical Flow Correlation in Gas Wells. User's Manual for API 148 Subsurface Controlled Safety Valve Sizing Computer Program, Appendix B*. Retrieved from

- Guet, S., & Ooms, G. (2005). FLUID MECHANICAL ASPECTS OF THE GAS-LIFT TECHNIQUE. *Annual Review of Fluid Mechanics*, 38(1), 225-249.
doi:10.1146/annurev.fluid.38.061505.093942
- Hagedorn, A. R., & Brown, K. E. (1965). Experimental Study of Pressure Gradients Occurring During Continuous Two-Phase Flow in Small-Diameter Vertical Conduits.
doi:10.2118/940-PA
- Hernandez-Perez, V., Zangana, M., Kaji, R., & Azzopardi, B. J. (2010). *Effect of pipe diameter on pressure drop in vertical twophase flow*. Paper presented at the 7th International Conference on Multiphase Flow ICMF Tampa, FL USA.
- Hibiki, T., & Ishii, M. (2000). Experimental study on hot-leg U-bend two-phase natural circulation in a loop with a large diameter pipe. *Nuclear Engineering and Design*, 195(1), 69-84. doi:[https://doi.org/10.1016/S0029-5493\(99\)00176-4](https://doi.org/10.1016/S0029-5493(99)00176-4)
- Jayanti, S., & Brauner, N. (1994). CHURN FLOW. 8(1-4), 471-521.
doi:10.1615/MultScienTechn.v8.i1-4.90
- Kataoka, I., & Ishii, M. (1987). Drift flux model for large diameter pipe and new correlation for pool void fraction. *International Journal of Heat and Mass Transfer*, 30(9), 1927-1939.
doi:[https://doi.org/10.1016/0017-9310\(87\)90251-1](https://doi.org/10.1016/0017-9310(87)90251-1)
- Mukherjee, H., & Brill, J. P. (1985). Pressure Drop Correlations for Inclined Two-Phase Flow. *Journal of Energy Resources Technology*, 107(4), 549-554. doi:10.1115/1.3231233
- Ohnuki, A., & Akimoto, H. (1996). An experimental study on developing air-water two-phase flow along a large vertical pipe: effect of air injection method. *International Journal of Multiphase Flow*, 22(6), 1143-1154. doi:[https://doi.org/10.1016/0301-9322\(96\)00039-0](https://doi.org/10.1016/0301-9322(96)00039-0)
- Ohnuki, A., & Akimoto, H. (2000). *Experimental Study on Transition of Flow Pattern and Phase Distribution in Upward Air-Water Two-Phase Flow Along a Large Vertical Pipe* (Vol. 26).
- OLGA. (2000). Dynamic Multiphase Flow Simulator: Schlumberger.
- Omebere-Iyari, N. K., Azzopardi, B. J., & Ladam, Y. (2007). Two-phase flow patterns in large diameter vertical pipes at high pressures. *AIChE Journal*, 53(10), 2493-2504.
doi:10.1002/aic.11288
- Pagan, E. (2016). *Modeling Churn and Annular Flow Regimes in Vertical and Near-Vertical Pipes with Small and Large Diameters*. (Masters), Louisiana State University Baton Rouge.
- Pagan, E., Williams, W. C., Kam, S., & Waltrich, P. J. (2017). A simplified model for churn and annular flow regimes in small- and large-diameter pipes. *Chemical Engineering Science*, 162, 309-321. doi:<https://doi.org/10.1016/j.ces.2016.12.059>
- Rao, B. (1998). Multiphase Flow Models Range of Applicability. In L. C. CTES (Ed.). Tech Note: CTES, L.C.
- Reinicke, K. M., & Remer, R. J. (1987). Comparison of Measured and Predicted Pressure Drops in Tubing for High-Water-Cut Gas Wells. doi:10.2118/13279-PA
- Schlegel, J. P., Sawant, P., Paranjape, S., Ozar, B., Hibiki, T., & Ishii, M. (2009). Void fraction and flow regime in adiabatic upward two-phase flow in large diameter vertical pipes. *Nuclear Engineering and Design*, 239(12), 2864-2874.
doi:<https://doi.org/10.1016/j.nucengdes.2009.08.004>
- Schoppa, W., Zabarar, G. J., Menon, R., & Wicks, M. (2013). *Gaps and Advancements for Deepwater Production and Remote Processing: Large Diameter Riser Laboratory Gas-Lift Tests*. Paper presented at the Offshore Technology Conference, Houston, Texas, USA.

- Shen, X., Hibiki, T., & Nakamura, H. (2015). Bubbly-to-cap bubbly flow transition in a long-26m vertical large diameter pipe at low liquid flow rate. *International Journal of Heat and Fluid Flow*, 52, 140-155. doi:<https://doi.org/10.1016/j.ijheatfluidflow.2015.01.001>
- Shoham, O. (2006). *Mechanistic Modeling of Gas-Liquid Two-Phase Flow in Pipes*.
- Shoukri, M., Hassan, I., & Gerges, I. (2008). Two-Phase Bubbly Flow Structure in Large-Diameter Vertical Pipes. *The Canadian Journal of Chemical Engineering*, 81(2), 205-211. doi:10.1002/cjce.5450810205
- Smith, T. R., Schlegel, J. P., Hibiki, T., & Ishii, M. (2012). Two-phase flow structure in large diameter pipes. *International Journal of Heat and Fluid Flow*, 33(1), 156-167. doi:<https://doi.org/10.1016/j.ijheatfluidflow.2011.10.008>
- SPE. (2015). Calculation of Worst-Case Discharge (WCD). In: Society of Petroleum Engineers.
- Takacs, G. (2001). *Considerations on the Selection of an Optimum Vertical Multiphase Pressure Drop Prediction Model for Oil Wells*. Paper presented at the SPE/ICoTA Coiled Tubing Roundtable, Houston, Texas.
- Wallis, G. B. (1969). One-dimensional two-phase flow.
- Waltrich, P. J., Capovilla, M. S., Lee, W., Zulqarnain, M., Hughes, R., Tyagi, M., . . . Griffith, C. (2017). *Experimental Evaluation of Wellbore Flow Models Applied to Worst-Case-Discharge Calculations*. Paper presented at the SPE Health, Safety, Security, Environment, & Social Responsibility Conference - North America, New Orleans, Louisiana, USA.
- Wu, B., Firouzi, M., Mitchell, T., Rufford, T. E., Leonardi, C., & Towler, B. (2017). A critical review of flow maps for gas-liquid flows in vertical pipes and annuli. *Chemical Engineering Journal*, 326, 350-377. doi:<https://doi.org/10.1016/j.cej.2017.05.135>
- Zulqarnain, M. (2015). *Deepwater Gulf of Mexico oil spill scenarios development and their associated risk assessment*. (PhD), Louisiana State University, Baton Rouge, LA.

6. APPENDIX A – LSU Multiphase Flow Simulator Instructions, Best Practices, and Recommendations.

Input Parameters | Casing Design | Results | About

CALCULATION TYPE

Worst Case Discharge Production

WELL LOCATION

Offshore Onshore

Seabed Depth [ft]

PVT DATA

Gas Oil Ratio [SCF/STB]

API Gravity [API]

Gas Gravity [SP.Gravity]

BHP CALCULATIONS

VLP VLP + IPR

Water Cut [%]

Oil Flow Rate [STB/D]

BHP WCD [psia]

Generate Avalon Inputs

TEMPERATURE CALCULATION

Wellhead Temperature [°F]

Bottomhole Temperature [°F]

PVT CORRELATIONS

Rs and Pb [v]

Bo [v]

μ_o [v]

WELLBORE FLOW CORRELATION

Hybrid Teles & Waltrich (LSU Model)

Sub Model Duns and Ros [v]

WELL INFORMATION

Name

Date of Simulation 8/26/2018 3:57:20 PM

EXIT NEXT

Craft & Hawkins Department of Petroleum Engineering
Louisiana State University, Baton Rouge

US Department of the Interior
Bureau of Ocean Energy Management
Gulf of Mexico OCS Region



August 2018

Instructions and Best Practices/Recommendations

The following pages describe in details how to use the LSU Multiphase Flow Simulator. Recommended Practices (RP) are provided at different steps for the user to consider and apply as appropriate.

RP: This simulator should be the only Excel file opened in order to avoid any conflict on the simulations. Make sure that Macros are allowed.

The screenshot shows the 'Input Parameters' tab of the LSU Multiphase Flow Simulator. The window title is 'LSU Multiphase Flow Simulator' and the tab is 'Input Parameters'. The interface is divided into several sections:

- CALCULATION TYPE:** Radio buttons for 'Worst Case Discharge' (A) and 'Production' (B).
- WELL LOCATION:** Radio buttons for 'Offshore' (C) and 'Onshore' (D). A text field for 'Seabed Depth' (C.i) is shown in feet.
- PVT DATA:** Text fields for 'Gas Oil Ratio' (E) in SCF/STB, 'API Gravity' (F) in API, and 'Gas Gravity' (G) in SP.Gravity.
- BHP CALCULATIONS:** Radio buttons for 'VLP' (H) and 'VLP + IPR' (I). Text fields for 'Water Cut' (H.i) in %, 'Oil Flow Rate' (H.ii) in STB/D, and 'BHP WCD' (H.iii) in psia.
- TEMPERATURE CALCULATION:** Text fields for 'Wellhead Temperature' (K) and 'Bottomhole Temperature' (L) in °F.
- PVT CORRELATIONS:** Dropdown menus for 'Rs and Pb' (M), 'Bo' (N), and 'μo' (O).
- WELLBORE FLOW CORRELATION:** A checked radio button for 'Hybrid Teles & Waltrich (LSU Model)' (P) and a dropdown menu for 'Sub Model' (P.i) set to 'Duns and Ros'.
- WELL INFORMATION:** Text fields for 'Name' (Q) and 'Date of Simulation' (R) set to '8/26/2018 3:57:20 PM'.

At the bottom, there are 'EXIT' (S) and 'NEXT' (T) buttons. A 'Generate Avalon Inputs' checkbox (J) is also present.

Figure 6.1 – LSU Multiphase Flow Simulator, First Tab.

6.1 Section on Input Parameters

The instructions below are for the input parameters included on Tab 1, as illustrated on Figure 6.1.

CALCULATION TYPE (A, B)

Choose (A) or (B) depending on modeling purpose.

- **Worst Case Discharge**

Figure 6.2 shows two screenshots of the software interface. The left screenshot displays the 'CALCULATION TYPE' section with 'Worst Case Discharge' selected (A) and the 'WELL LOCATION' section with 'Offshore' selected (C) and 'Seabed Depth' input field (C.i). The right screenshot displays the 'CALCULATION TYPE' section with 'Worst Case Discharge' selected (A) and the 'WELL LOCATION' section with 'Onshore' selected (D) and 'Atmospheric Pressure' input field (D.i).

Figure 6.2 – WCD choice.

If Worst Case Discharge **A** is selected, enter the **WELL LOCATION** in order to determine the top node pressure.

Choose (C) Offshore and enter the Seabed depth (ft) on (C.i) or choose Onshore **(D)** and enter the Atmospheric Pressure (psia) on (D.i).

- **Production**

Figure 6.3 shows a screenshot of the software interface. The 'CALCULATION TYPE' section has 'Production' selected (B) and the 'Wellhead Pressure' input field (B.i).

Figure 6.3 – Production choice.

If Production (B) is selected, enter the Wellhead Pressure (psia) on (B.i).

PVT DATA (E, F, G)

Figure 6.4 shows a screenshot of the software interface. The 'PVT DATA' section has three input fields: 'Gas Oil Ratio' (E) [SCF/STB], 'API Gravity' (F) [API], and 'Gas Gravity' (G) [SP.Gravity].

Figure 6.4 – PVT Data.

Enter producing GOR (SCF/STB) (E), Oil API Gravity (F), and Condensate Gas Gravity (G).

LSU Multiphase Flow Simulator

Input Parameters | Casing Design | Results | About

CALCULATION TYPE

A Worst Case Discharge **B** Production

WELL LOCATION

C Offshore Onshore **D**

C.i Seabed Depth [ft]

PVT DATA

E Gas Oil Ratio [SCF/STB]

F API Gravity [API]

G Gas Gravity [SP.Gravity]

BHP CALCULATIONS

H VLP VLP + IPR **I**

H.i Water Cut [%]

H.ii Oil Flow Rate [STB/D]

H.iii BHP WCD [psia]

J Generate Avalon Inputs

S **EXIT**

TEMPERATURE CALCULATION

K Wellhead Temperature [°F]

L Bottomhole Temperature [°F]

PVT CORRELATIONS

M Rs and Pb

N Bo

O μ_o

WELLBORE FLOW CORRELATION

P Hybrid Teles & Waltrich (LSU Model)

P.i Sub Model

WELL INFORMATION

Q Name

R Date of Simulation

T **NEXT**

Figure 6.1 – LSU Multiphase Flow Simulator, First Tab.

WCD CALCULATIONS (H, I)

Choose **(H)** or **(I)** depending on whether you want a pressure gradient (VLP) or a Nodal Analysis (VLP+IPR) to be performed.

- **VLP (Vertical Lift Curve)**

The screenshot shows the 'BHP CALCULATIONS' window with the 'VLP' radio button selected. The 'H' radio button is also selected. The interface includes three input fields: 'Water Cut [%]' (labeled H.i), 'Oil Flow Rate [STB/D]' (labeled H.ii), and 'BHP WCD [psia]' (labeled H.iii). The 'BHP WCD' field is highlighted with a red box and contains the word 'Optional'.

Figure 6.5 – BHP Calculations, VLP.

Enter the Water Cut (%) **(H.i)**, Oil Flow Rate (STB/day) **(H.ii)**, and BHP WCD (psia) **(H.iii)**.

*RP: Water Cut **(H.i)** can have a range from 0 to 99%.*

*RP: BHP WCD **(H.iii)** is entered to compare the VLP (gradient). Either a measured BHP or a BHP calculated using another system can be entered in order to determine the **error** compared with the BHP calculated using the LSU Multiphase Flow Simulator at the rate and water cut provided. This entry is optional, if left in blank or “zero” the error will not be provided in the Results.*

- **VLP + IPR (Inflow Performance Relationship)**

The screenshot shows the 'BHP CALCULATIONS' window with the 'VLP + IPR' radio button selected. The 'I' radio button is also selected. The interface includes four input fields: 'Water Cut [%]' (labeled I.i), 'Reservoir [psia]' (labeled I.ii), 'PI [STB/D/psia]' (labeled I.iii), and 'Qo WCD [STB/D]' (labeled I.iv). The 'Qo WCD' field is highlighted with a red box and contains the word 'Optional'.

Figure 6.6 – BHP Calculations, Nodal Analysis.

Enter the Water Cut (%) **(I.i)**, Reservoir Pressure **(I.ii)**, and Productivity Index (PI) (STB/day/psia) **(I.iii)**. Qo (STB/day) is calculated based on a Linear Inflow Performance Curve.

*RP: Water Cut **(I.i)** can have a range from 0 to 99%.*

*RP: Qo WCD **(I.iv)** is optional! Either a measured Oil Flow Rate or an Oil Flow Rate calculated using another system can be entered in order to determine the **error** compared with the Oil Flow Rate calculated in this simulator. As for BHP WCD, this entry is optional, if this value is left in blank or “zero” the error will not be provided in the Results.*

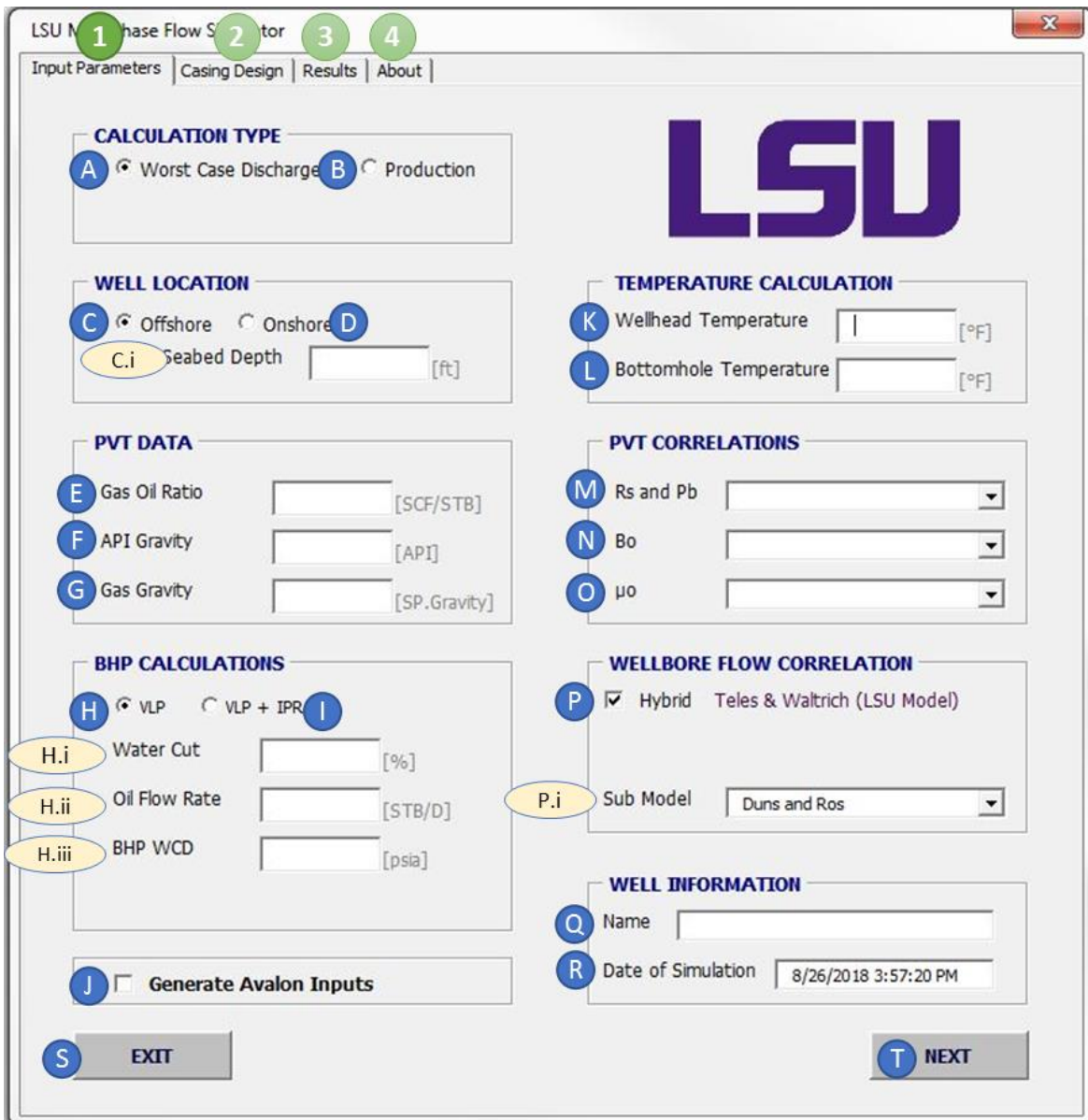


Figure 6.1 – LSU Multiphase Flow Simulator, First Tab.

TEMPERATURE CALCULATION (K, L)

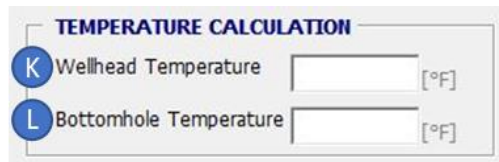


Figure 6.7 – Temperature Calculation.

Enter the top node temperature (°F) (**K**) (either at the wellhead, surface, or seabed) and bottomhole temperature (°F) (**L**). The temperature is assumed to change linearly between top temperature and the bottomhole temperature.

PVT CORRELATIONS (M, N, O)

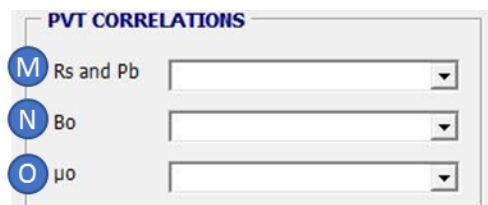


Figure 6.8 – PVT Correlations

Choose the correlations for Solution Gas Oil Ratio and Bubble Point Pressure (**M**), Oil Formation Volume Factor (**N**), and Oil Viscosity (**O**).

RP: All these correlations were empirically developed and if the flow conditions go beyond the range of applicability, errors on the calculation of the fluid properties might happen. This can lead to errors on the pressure curves and the simulation can crash. More information about these possible errors are provided in APPENDIX B: “Identifying Errors” at the end of this guide.

Avalon® Input Generation (J)



Figure 6.9 – Avalon® input generation option.

This option is fully explained in Appendix B “Avalon® Input Generation”.

WELLBORE INFORMATION (Q, R)

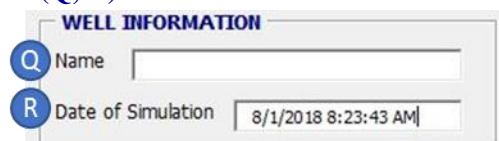


Figure 6.10 – Well information.

Enter the Well name on (**Q**). The date of Simulation (**R**) is automatically provided by the simulator.

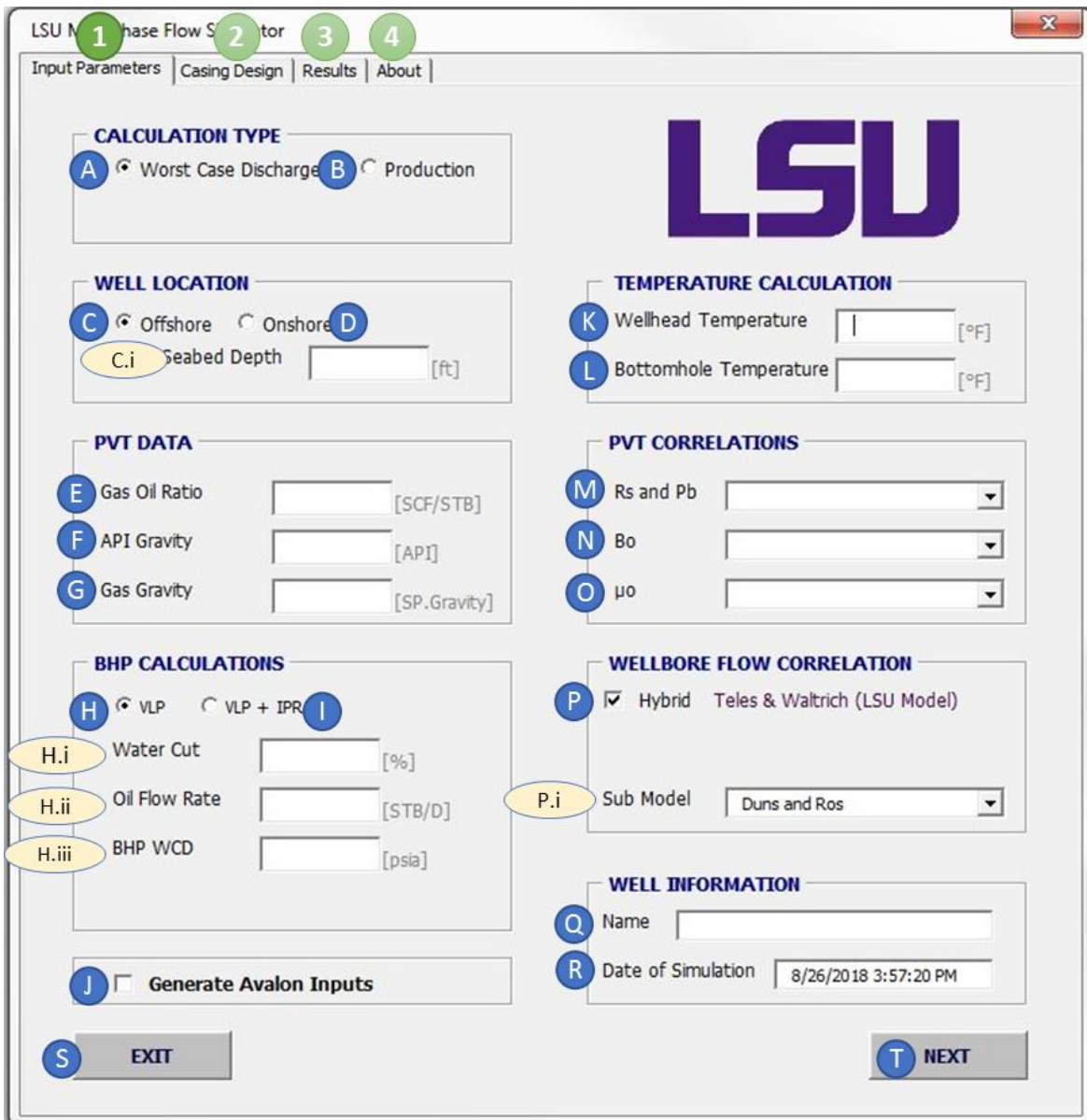


Figure 6.1 – LSU Multiphase Flow Simulator, First Tab.

WELLBORE FLOW CORRELATION (P, U)

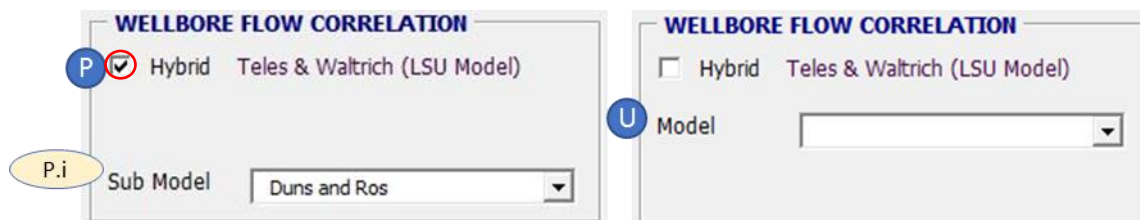


Figure 6.11 – Wellbore Flow Correlation.

If Hybrid **Teles & Waltrich (LSU Model)** (P) is selected, the Sub Model (P.i) is recommended to be Duns and Ros, since that is how LSU Model was validated. If not using the Hybrid model, leave the check box empty and choose only a Model (U) for the system to use. Table 6.1 shows the models available and their applicability.

Recommendation: *LSU Model must be used for large diameters where churn flow regime is likely to be present. It has shown good results, since it also considers the absence of slug flow in large diameter well as described in this report. The hybrid model works well for high GOR and wells inclination up to 15° from the vertical.*

Table 6.1 – Models and their applicability. Rao (1998); and Brill and Mukherjee (1999).

Model	Applicability
<i>Aziz, Govier, and Fogarase</i>	Can be considered a mechanistic correlation. No GLR and water-cut ranges of applicability were found for this correlation.
<i>Baxadendell and Thomas</i>	No-slip holdup correlation. No flow pattern consideration. Not recommended for quantitative work.
<i>Beggs and Brill</i>	Recommend for inclined wells. GLR lower than 5,000 SCF/STB. Generally good for water-cut up to 10%.
<i>Dukler</i>	Based on similarity analysis. Friction factor and holdup calculations are based on field data. No GLR and water-cut ranges of applicability were found for this correlation.
<i>Duns and Ros</i>	GLR lower than 5,000 SCF/STB. Not recommended when water is present.
<i>Fancher and Brown</i>	No-slip holdup correlation. No flow pattern consideration. It always under predicts the pressure. This should not be used for qualitative work.
<i>Gray</i>	Recommended for gas condensate wells.
<i>Hagedorn and Brown</i>	GLR lower than 5,000 SCF/STB. Accurate prediction for tubing sizes between 1 and 1.5 in. Good for a wide range of water-cuts.
<i>Mukherjee and Brill</i>	This model is an attempt to overcome some of the limitations of Beggs and Brill model. No GLR and water-cut ranges of applicability were found for this correlation.
<i>Orkiszewski</i>	GLR lower than 5,000 SCF/STB. Good for a wide range of water-cuts. Good for °API higher than 30. This correlation contains a discontinuity for velocities higher than 10ft/s.

LSU Multiphase Flow Simulator

Input Parameters | Casing Design | Results | About

CALCULATION TYPE

A Worst Case Discharge **B** Production

WELL LOCATION

C Offshore Onshore **D**

C.i Seabed Depth [ft]

PVT DATA

E Gas Oil Ratio [SCF/STB]

F API Gravity [API]

G Gas Gravity [SP.Gravity]

BHP CALCULATIONS

H VLP VLP + IPR **I**

H.i Water Cut [%]

H.ii Oil Flow Rate [STB/D]

H.iii BHP WCD [psia]

J Generate Avalon Inputs

S **EXIT**

TEMPERATURE CALCULATION

K Wellhead Temperature [°F]

L Bottomhole Temperature [°F]

PVT CORRELATIONS

M Rs and Pb

N Bo

O μ_o

WELLBORE FLOW CORRELATION

P Hybrid Teles & Waltrich (LSU Model)

P.i Sub Model

WELL INFORMATION

Q Name

R Date of Simulation

T **NEXT**

Figure 6.1 – LSU Multiphase Flow Simulator, First Tab.

6.2 Section on Casing Design

LSU Model - Phase Flow Simulator

Input Parameters | Casing Design | Results | About

WELBORE CONFIGURATION

MD and TVD MD and Angle

A Number of Casings: **OK** Up to of 5 casing setting depths!

	Measured Depth [ft]	TVD [ft]	Tubing ID [in]	Tubing Roughness [in]	Discretization
1	D	E	F	G	H
2					
3					
4					
5					

I **IMPORT**

*Wellbore configuration from seabed until the top of sand 1.

J **RUN**

K **EXIT**

Figure 6.12 – Casing Design, Second Tab.

WELL CONFIGURATION (A, B, C, D, E, F, G, H)

Enter the number of casings setting (A) down to the top of the open hole section (sand 1). Then click on the **OK** button.

Enter either MD and TVD (B) or MD and Angle (from horizontal) (C).

Enter the setting Measured Depth (D), either True Vertical Depth or Angle with the Horizontal (degrees) (E), Inner Tubing Diameter (F), Tubing Roughness (G) and discretization (H) for each section, then click on “Import” button (I).

RP: The depths entered are the setting depths (top down), not section’s length.

RP: It is possible to set 5 casing depths (Number of casings).

Recommendation: Discretization is the number of sub intervals that the system will use to compute the pressure gradient values. The maximum total number of discretization intervals should be 200. For a 10,000ft deep well 50 increments for discretization has shown to be a good number. Higher numbers should be entered for complex multiphase flow conditions.

Once all the correct input for the **wellbore configuration** is entered, press the **IMPORT** button (I) in order to import the wellbore profile to the simulator. After that, the well profile appears as illustrated in Figure 6.13. This figure also illustrates an example of how these data should be entered by the user.

*RP: The button **IMPORT** (J) should be pressed after any modification on the wellbore configuration input data page, otherwise the simulations will be done based on the last imported data.*

RP: If any of the depths entered are not correct, errors in the calculation of pressure gradient will occur. A message will be seen for a few cases in which the entered data is not correct. For instance, when TVD is higher than MD. The code does not identify every possible error; therefore when importing the well data if the simulator has a run time error (crashes), close it, reopen the simulator and make sure all the data are correct.

Having all the correct input data entered, click on the **RUN** button (J). After a few seconds the Results will be shown.

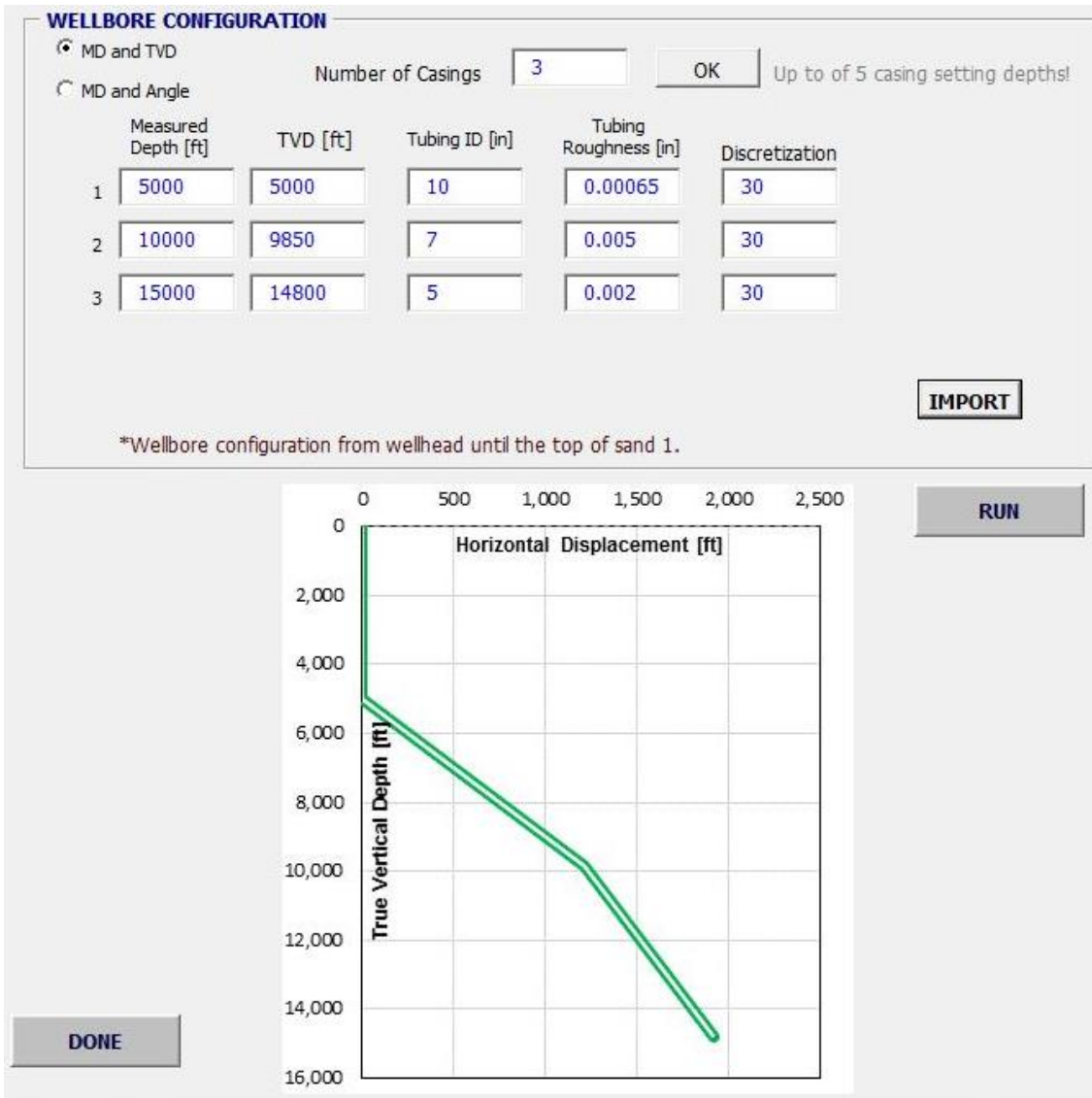


Figure 6.13 – Wellbore Configuration Example.

6.3 Results

On the Results tab, the Pressure (A) versus Depth (B) profile and the flow regimes present in the well will be shown. In addition, Bottomhole Pressure (C) and the Error (D) if the data was provided, or the Oil Flowrate and Error will also be displayed.

Figure 6.14 shows an example for BHP calculation, where the LSU Model was used and annular flow is present in the well.

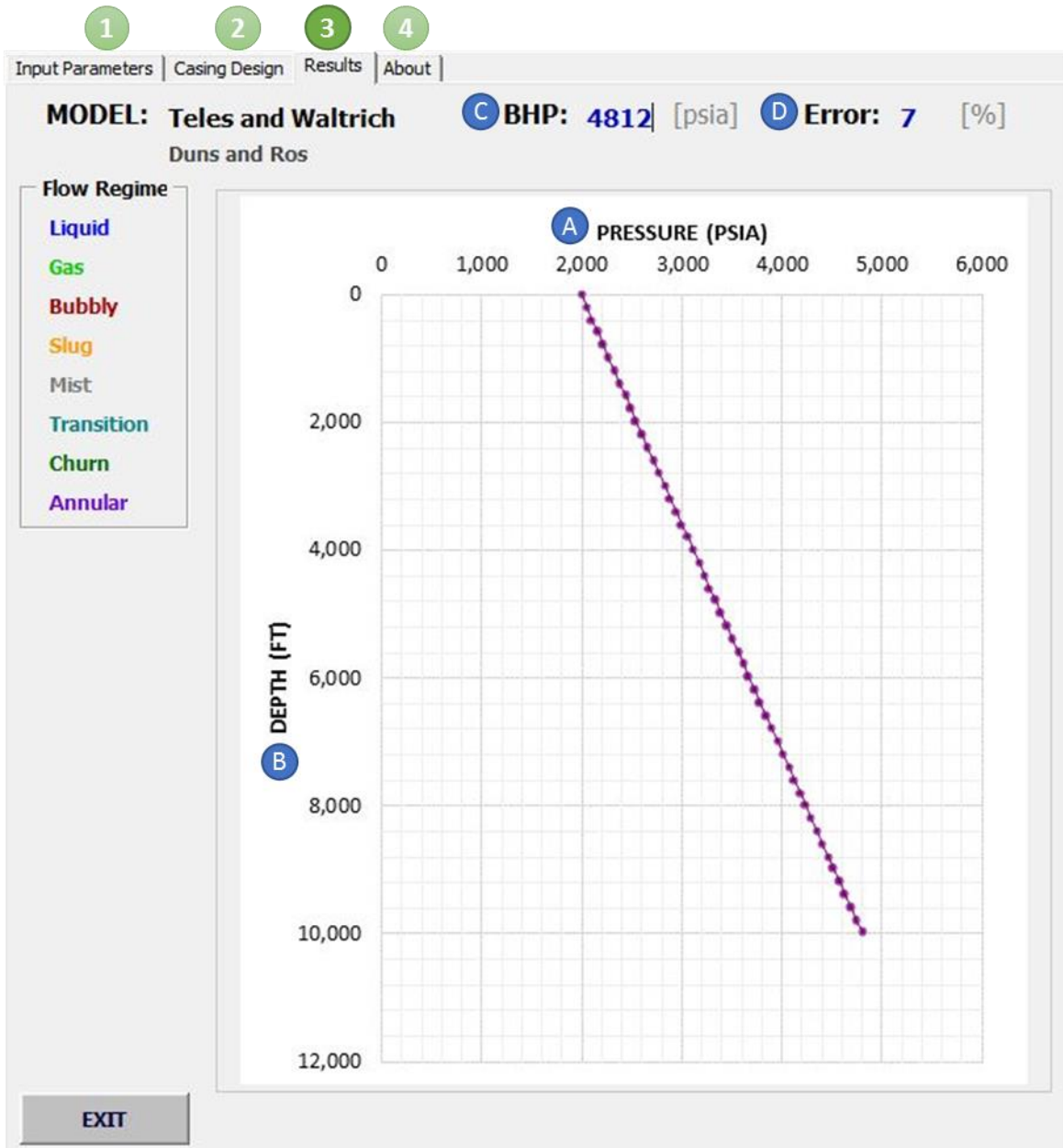


Figure 6.14 – Results, Third Tab.

6.4 About

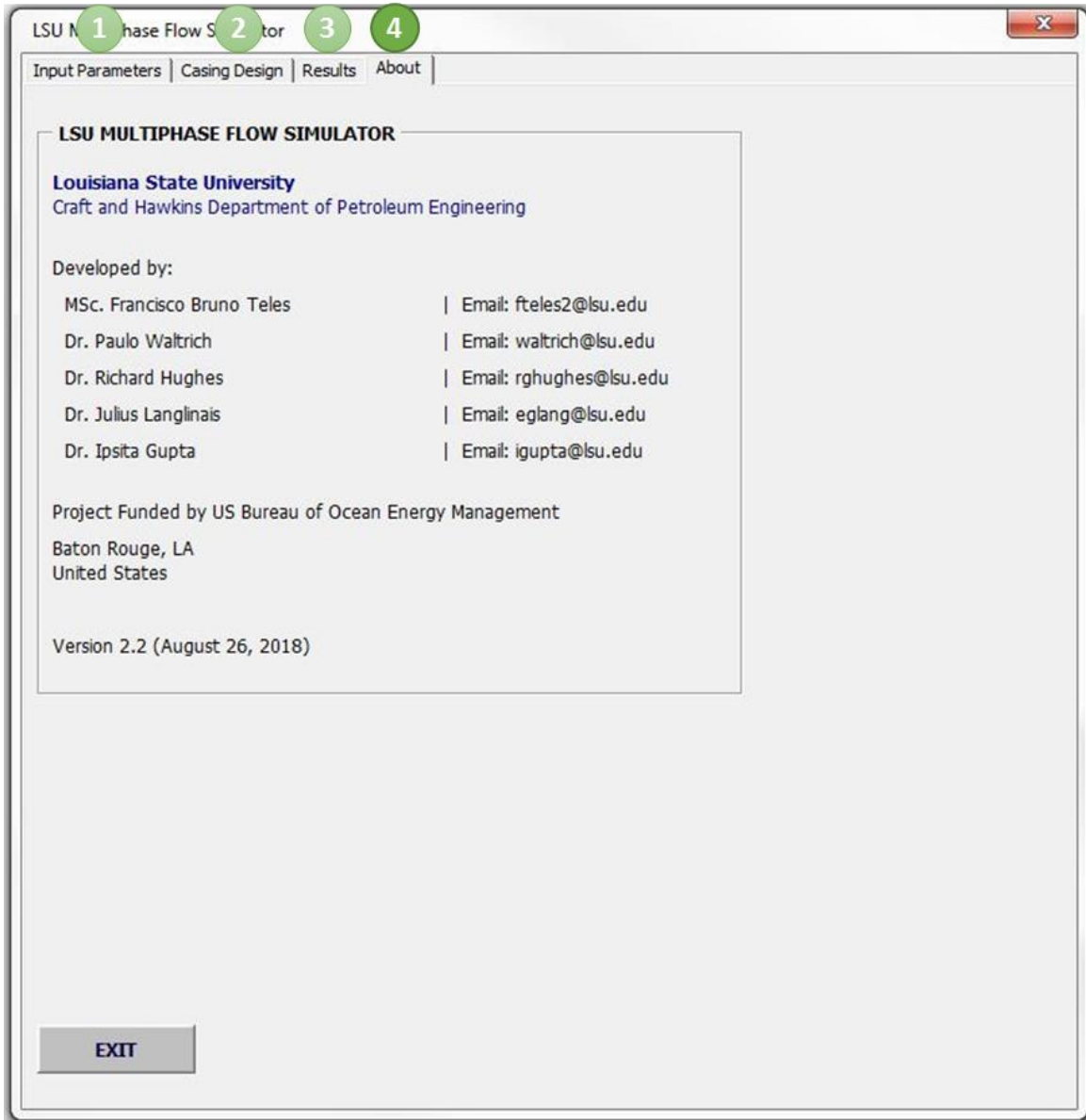


Figure 6.15 – About Section, Fourth Tab.

This tab shows the information about the developers and institutions involved on the LSU Multiphase Flow Simulator project.

To close the simulator just click on the **EXIT** button, then the Excel spreadsheet will be shown.

To open the Graphical User Interface after closing it, press the button shown below on the Excel spreadsheet, as illustrated in Figure 6.16.



Figure 6.16 – Opening GUI button.

6.5 APPENDIX B – Avalon® Input Generation



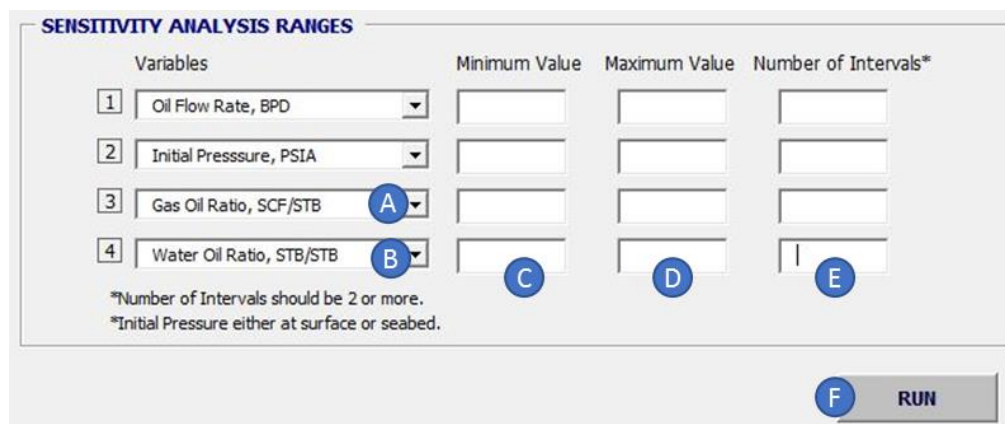
Figure 6.17 – Avalon® generation input option

- If this option is selected, the LSU Multiphase Flow Simulator is going to perform a sensitivity analysis for different parameters and ranges chosen by the user.

Enter the same input as described before (**TEMPERATURE CALCULATION, PVT CORRELATIONS, and WELLBORE FLOW CORRELATION**). For **PVT DATA** and **WCD CALCULATION** on Input Parameters tab **enter the variables that will not be on the sensitivity analysis**.

RP: If there is any number on these inputs, they will be ignored and only those on the Avalon® Input Generation tab will be considered.

Figure 6.18 shows the Avalon® Input Generation tab.



Variables	Minimum Value	Maximum Value	Number of Intervals*
1 Oil Flow Rate, BPD			
2 Initial Pressure, PSIA			
3 Gas Oil Ratio, SCF/STB (A)			
4 Water Oil Ratio, STB/STB (B)	(C)	(D)	(E)

*Number of Intervals should be 2 or more.
*Initial Pressure either at surface or seabed.

(F) RUN

Figure 6.18 – Avalon® Input Generation.

Variables 1 and 2 are pre-selected and they are Oil Flow Rate (STB/D) and Initial Pressure (either surface or seabed pressure in PSIA), respectively.

Select at least one additional variable (3) in order for the sensitivity analysis to be performed. Once the fourth variable is chosen, the boxes for the inputs appear. After having inserted all values, click on the **RUN** button.

The results of bottomhole pressure for the sensitivity analysis are shown in the Excel Spreadsheet on the tab “Sensitivity”. By clicking on Import Results button, the Graphical User Interface closes and the spreadsheet appears as shown in Figure 6.19.

*RP: The bottomhole pressures generated on this spreadsheet can be copied to Avalon® by clicking on “Modify or Import Nodal Data” on the Avalon® software and pasting the LSU Multiphase Flow results on its table. Then, the Inflow Tubing Curves can be plotted. **Make sure the same variables, minimum, maximum and number of intervals are chosen in Avalon® interface on the “Producing Well Case Study Variables” set up in order for the curves to be imported correctly. Also make sure that the sequence of the first and second variables on the Avalon® screen is the same as in the LSU Multiphase Flow Simulator sensitivity results.***

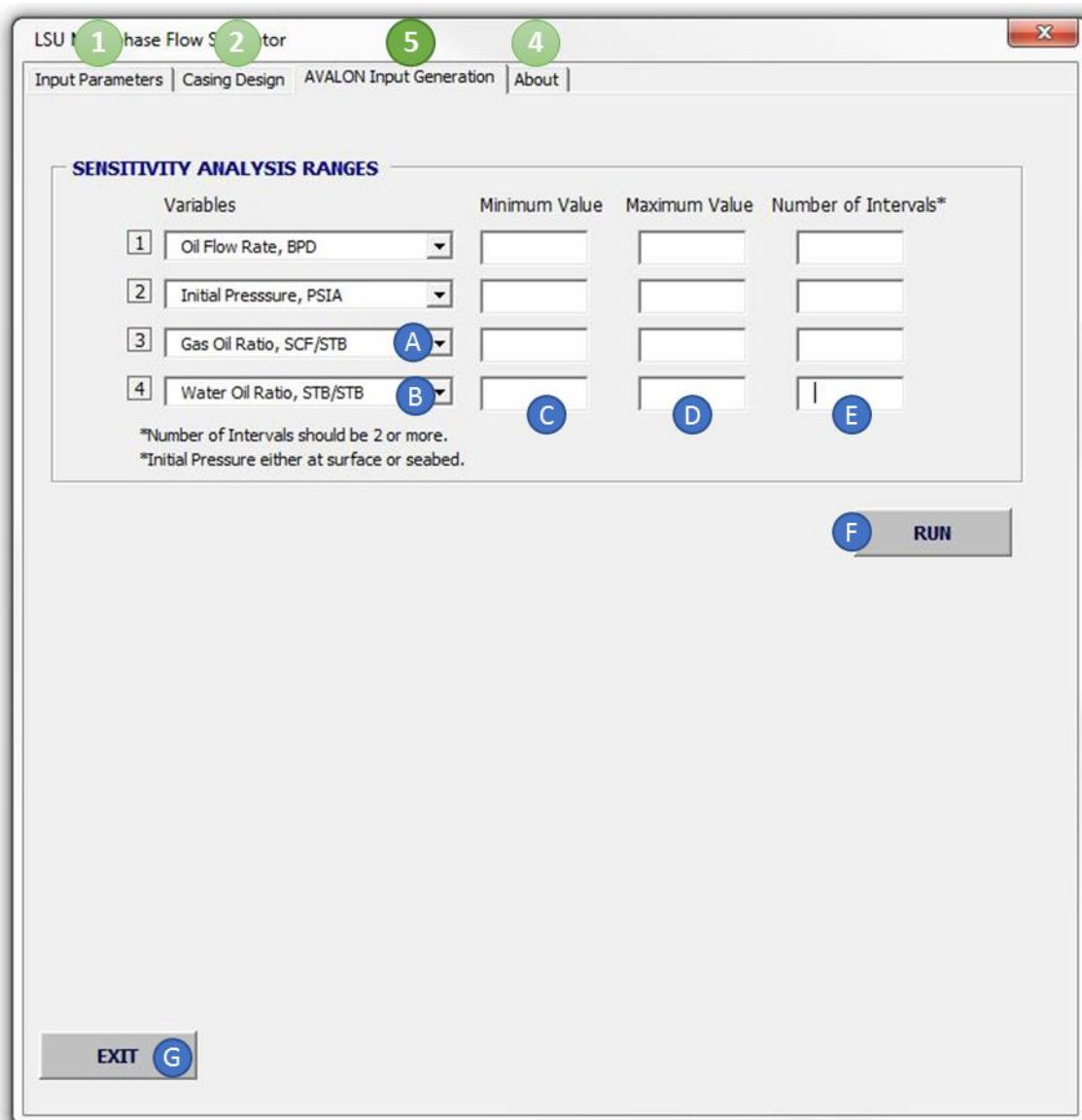


Figure 6.18 – Avalon® Input Generation, Fifth Tab.

NOTICE

RP: Depending on the number of variables, intervals, and discretization, the simulator may take several minutes to run. It might even look like Excel has stopped running. If the simulation takes too long and Excel has really stopped running, this may be due to one of the reasons described in Appendix C.

	A	B	C	D	E	F	G	H	I
1				Initial Pressure					
2	Entry	Oil Rate	GOR	500	1375	2250	3125	4000	
3	1	100	200	4500.79	5388.14	6277.59	7167.09	8056.64	
4	2	100	900	4293.58	5154.16	5983.31	6808.83	7633.81	
5	3	100	1600	4196.48	5107.01	5940.37	6739.39	7509.5	
6	4	100	2300	4091.8	5057.65	5905.85	6711.99	7486.73	
7	5	100	3000	3977.64	5007.37	5871.02	6684.43	7463.87	
8	6	2311.111	200	4437.3	5389.96	6279.43	7168.95	8058.54	
9	7	2311.111	900	2568.05	4769.53	5824	6747.26	7619.74	
10	8	2311.111	1600	1684.47	3702.83	5408.65	6411.65	7314.47	
11	9	2311.111	2300	1465.37	3209.51	4639.03	5873.33	7073.18	
12	10	2311.111	3000	1419.27	2930.27	4369.61	5535.33	6575.59	
13	11	4522.222	200	4381	5394.22	6283.79	7173.4	8063.04	
14	12	4522.222	900	2465.51	4426.79	5684.25	6708.83	7618.8	
15	13	4522.222	1600	1755.04	3660.8	5041.03	6156.31	7169.34	
16	14	4522.222	2300	1550.31	3223.57	4648.53	5796.98	6821.49	
17	15	4522.222	3000	1499.09	2958.85	4381.92	5545.58	6584.92	
18	16	6733.333	200	4380.31	5400.51	6290.19	7179.88	8069.6	
19	17	6733.333	900	2499.53	4432.26	5686.31	6710.07	7623.45	
20	18	6733.333	1600	1824.22	3676.16	5052.01	6165.94	7174	
21	19	6733.333	2300	1634.37	3246.97	4663.79	5809.86	6833.36	
22	20	6733.333	3000	1590.5	3003.65	4401.96	5562.35	6599.96	
23	21	8944.444	200	4387.04	5408.78	6298.58	7188.37	8078.17	
24	22	8944.444	900	2542.14	4442.85	5693.84	6716.39	7631.86	
25	23	8944.444	1600	1896.31	3697.33	5067.3	6179.21	7183.91	
26	24	8944.444	2300	1719.92	3282.36	4684.86	5827.8	6849.77	
27	25	8944.444	3000	1683.74	3059.53	4429.73	5585.45	6620.9	
28	26	11155.56	200	4396.34	5418.96	6308.89	7198.8	8088.68	
29	27	11155.56	900	2591.12	4458.78	5704.83	6726.52	7643.39	
30	28	11155.56	1600	1972.8	3724.35	5086.71	6196.2	7198.15	
31	29	11155.56	2300	1809.51	3327.78	4711.84	5850.52	6870.66	
32	30	11155.56	3000	1781.84	3124.52	4465.33	5614.9	6647.58	
33	31	13366.67	200	4407.97	5431.03	6321.1	7211.12	8101.1	
34	32	13366.67	900	2645.09	4477.27	5719.15	6739.24	7657.75	
35	33	13366.67	1600	2055.98	3757.01	5110.26	6217.45	7216.25	
36	34	13366.67	2300	1904.24	3381.37	4744.45	5878.41	6896.06	
37	35	13366.67	3000	1885.95	3197.72	4508.09	5650.64	6680.07	
38	36	15577.78	200	4421.77	5444.95	6335.17	7225.31	8115.39	
39	37	15577.78	900	2703.92	4499.52	5736.7	6755.94	7674.8	
40	38	15577.78	1600	2144.04	3795.23	5137.97	6241.58	7238.82	
41	39	15577.78	2300	2004.52	3442.37	4782.72	5910.84	6925.89	
42	40	15577.78	3000	1996.46	3278.21	4558.36	5692.7	6718.18	
43	41	17788.89	200	4437.67	5460.71	6351.09	7241.36	8131.54	
44	42	17788.89	900	2766.85	4526.32	5757.43	6775.17		
45	43	17788.89	1600	2236.33	3838.56	5169.54	6269.32	7264.24	
46	44	17788.89	2300	2111.66	3509.84	4826.56	5948.32	6960.17	
47	45	17788.89	3000	2113.81	3365.54	4616.15	5740.94	6761.99	
48	46	20000	200	4455.59	5478.3	6368.84	7259.23	8149.52	

Figure 6.19 – Sensitivity Analysis Table.

6.6 APPENDIX C – Identifying Errors

- *Convergence Error of Pressure Gradient*

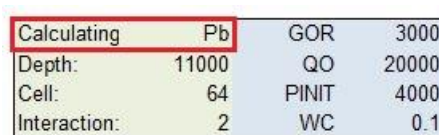
In some cases one or more of the calculations for the flow conditions go beyond the range of applicability for which these correlations were developed. When this happens, the pressure gradient calculation does not converge and simulation either has a run time error or gets stuck in a loop and the system is non-responsive.

When generating the sensitivity analysis table, if there are any convergence errors, the BHP calculation for this specific cases will be skipped. This means that the Spreadsheet with the sensitivity results will contain blank cells since the BHP could not be calculated.

- *Fluid Properties Calculation Error*

As stated previously, when the flow conditions go beyond the range of applicability in which these empirical correlations were based, other errors might happen and the simulation has run-time errors (i.e. when there is a division by zero or a square of a negative number).

When this happens the user should close the Graphical User Interface and look at where the error occurred. As shown below in the red box in Figure 6.20, the properties that are being calculated appear. If an error happens and one of the fluid properties will appear in the cell, (“Bo” for Oil Formation Volume Factor, “Pb” for Bubble Point Pressure, “Rs” for Solution Gas Oil Ratio, “Oil Visc.” for Oil Viscosity). If this happens the user should choose a different correlation for that property and run the simulator again.



Calculating	Pb	GOR	3000
Depth:	11000	QO	20000
Cell:	64	PINIT	4000
Interaction:	2	WC	0.1

Figure 6.20 – Simulation Progress.

If the error keeps happening after changing the PVT correlations, it means that it will not be possible to run the simulator for this flow condition.

- *Critical Flow Condition Error*

For cases with very high flow velocities of gas and/or liquid, critical flow might be present. So far the LSU model cannot be used to calculate pressure drops at these conditions. If there is critical flow at some point in the well, the simulation will not converge and a flag will appear warning about this. Therefore, the simulator will not be able to predict bottomhole pressure for these cases. The research group at LSU is working on how the simulator can better handle critical flow conditions, which is an on-going issue for all multiphase flow simulators.

7. APPENDIX D – Integrated Reservoir-Wellbore Nodal Analysis WCD Model

On a separate (not in scope of current project) but related study, Cordoba and Gupta (2018); Cordoba (2018) generated an integrated reservoir-wellbore nodal analysis Worst Case Discharge (WCD) model whereby the static wellbore models are dynamically coupled with material balance tanks such that reservoir pressure feeding into the wellbore (and thus IPR) models are updated every time step of the worst case discharge forecast. The reservoir coupling is not restricted to a single formation, but to stacked reservoirs (oil, gas, water) analogous to Gulf of Mexico geologic stacking patterns. Preliminary results suggest that this coupled nodal analysis method can act as a quicker method compared to full scale reservoir simulations for worst case discharge calculations while integrating both the reservoir and the wellbore. Additionally sensitivity studies suggest that the significance of inclusion of water sands in worst case discharge calculations depends on the stratigraphic position in relation to the sands in the open-hole section. Results from an example simulation Cordoba (2018) is given below where including the water sand at the base does not impact the WCD volumes, but excluding the water sand at the top of the open hole makes a huge impact.

Table 7.1 – Comparison of WCD volumes based on aquifer stratigraphic position from Cordoba (2018)

		GAP - Water at the base	GAP - Water at the base disable	% ERROR
BASE CASE - Hagedorn and Brown - Water at the base	Cumulative Oil Production (MMSTB)	0.875	0.952	8%
	Cumulative Water Production (MMSTB)	1.102	0.907	21%
	Cumulative Gas Production (MMscf)	375.332	411.839	9%
		GAP - Water at the top	GAP - Water at the top disable	% ERROR
BASE CASE - Hagedorn and Brown - Water at the top	Cumulative Oil Production (MMSTB)	2.32	1.166	99%
	Cumulative Water Production (MMSTB)	1.007	0.321	214%
	Average Gas Rate (MMscf/day)	15.622	4.042	286%

This study is ongoing subject to availability of funding.

8. APPENDIX E – TWO-PHASE FLOW REGIME MAP FOR LARGE DIAMETER PIPES AND HIGH-VELOCITY FLOWS (MASTERS THESIS)

A Thesis
Submitted to the Graduate Faculty of the
Louisiana State University and
Agricultural and Mechanical College
in partial fulfillment of the
requirements for the degree of
Master of Science
in
Craft & Hawkins Petroleum Engineering Department

by
Matheus Sigaki Capovilla
B.Sc., Federal University of Santa Catarina, 2015

Acknowledgments

I would like to thank my advisor, Dr. Paulo Waltrich for the opportunity given to me to be part of this program and this project. I also want to thank him for all discussions and help building knowledge to complete this thesis. I want to extend this acknowledgment to my committee members, Dr. Crag Griffith, Dr. Mauricio Almeida, and Dr. Julius Langlinais, who generously accepted a short notice invitation to be part of it. You honor me by sharing your knowledge and experience with me.

I am very grateful for my family, for the unconditional love given to me. My parents Ivete and Marcos, for being the most loving and supportive people in the world. My fiancée Larissa, for always being there for me, for putting me up everytime I went down, and for sharing the best moments of my life. My daughter Beatriz, for giving me a reason to go forward. I also thank my siblings, Mariana and Alyson, for being part of my life.

Finally, I want to thank my friends. New friends that I made here in Baton Rouge and old friends that I carry with me for a long time. You have made my path more enjoyable. Special thanks for my best friend, Thiago, for helping me to keep me on my way.

Thank y'all.

Table of Contents

ACKNOWLEDGMENTS	ii
LIST OF TABLES	iv
LIST OF FIGURES	v
ABSTRACT	viii
CHAPTER	
1 INTRODUCTION	1
1.1 WCD rate calculation	1
1.2 Two-phase flow regimes in vertical pipes	3
1.3 Influence of pipe diameter on two-phase flow regimes	6
1.4 Statement of the problem and objectives	9
2 LITERATURE REVIEW	13
2.1 Important parameters for two-phase flow in pipes	13
2.2 Teles and Waltrich model [33] (or modified Pagan et al. [34])	14
2.3 Pagan et al. [34] model	15
2.4 Duns and Ros [11] model	19
2.5 Flow regime maps	26
2.6 Critical flow transition	41
3 EXPERIMENTAL DATA	45
3.1 Experimental data from literature	45
3.2 LSU experiments from Waltrich et al. [9]	48
4 RESULTS AND DISCUSSIONS	52
4.1 Evaluation of current flow regime maps	52
4.2 Computational Fluid Dynamic (CFD) observations	57
4.3 Flow regime map validation	61
4.4 Water and air – Data from Waltrich et al. [9]	65
4.5 Oil and gas – Data from Asheim [65]	70
4.6 Critical flow	71
5 CONCLUSIONS AND FUTURE WORKS	80
5.1 Summary and conclusions	80
5.2 Recommendations for future work	82
REFERENCES	84
APPENDIX: DATA FROM LSU EXPERIMENTS	90
VITA	94

List of Tables

2.1	Summary of pros and cons of the flow regime maps considered in this study.	32
3.1	Literature review on flow regime characterization of vertical upward two-phase flows in large diameter pipes.	46
3.2	Field data that provide information of pressure gradient.	48
4.1	Analysis of conforming and non-conforming experimental data points for different transition boundaries of different flow regime maps.	55
4.2	Experimental data considered for calculation of pressure gradient with CFD on Waltrich et al. [9].	57
4.3	Comparative of calculated absolute error with the model proposed in this work and the model by Teles and Waltrich for groups of data points with different diameters and similar conditions.	67
4.4	Natural gas composition considered for the calculation of the critical mixture velocity.	71
A.1	Experimental data generated at LSU.	90

List of Figures

1.1	Elements required for the prediction of production rates	2
1.2	Simplified diagram for WCD rate calculation.	4
1.3	Visual representation of the four central flow regimes during upward flow in a vertical pipe	5
1.4	Flow regime maps: (a) Aziz et al. [17] empirical map, and (b) Taitel et al. [18].	6
1.5	Force balance sustained in a Taylor bubble.	7
1.6	Separation of what is considered a large diameter pipe by Kataoka and Ishii [25] criteria. The area above the curves represent the diameters considered large.	8
1.7	Cap-bubble flow, adapted from Ohnuki and Akimoto [23].	9
1.8	Flow regime progression with increasing height along the wellbore and estimated pressure profiles considering different flow regimes along the flow.	11
2.1	Teles and Waltrich model workflow [33].	15
2.2	Average Absolute Error of pressure gradient in % for various two-phase flow pressure gradient models	16
2.3	Force balance for a pipe segment for churn and annular flow regimes.....	16
2.4	Empirical flow regime map by Duns and Ros [11]	20
2.5	L1 and L2 factors versus dimensionless diameter number (N_d) [11].	22
2.6	F-factor numbers for Region I, based on the dimensionless viscosity number N_l [11].	24
2.7	F-factor numbers for Region II, based on the dimensionless viscosity number N_l [11].	24
2.8	Dimensionless f_1 factor as a function of Re and relative roughness ϵ/D [11].	25
2.9	Dimensionless f_2 factor as a function of the group $f_1 R N_d^{2/3}$ [11].	26
2.10	Correlation for the film-thickness ϵ under mist-flow conditions [11].	27

2.11	Representation of Wu et al. [16] method to evaluate accuracy of flow regime map.....	28
2.12	Comparative between different flow regime transitions models and experimental observations for pipe diameters between 12.3 and 67 mm [16].....	29
2.13	Experimental results reported by Beck et al. [61] for experimental two-phase flow in a pipe with a 0.12 m diameter and Wallis [41] calculated for their experimental conditions.	44
3.1	Different flow regimes for vertical upward two-phase flows in large diameter pipes of the experimental data considered in this study.....	47
3.2	Literature review on works with characterized flow regimes for vertical upward two-phase flows in large diameter pipes.	48
3.3	Schematic diagram of the experimental apparatus and pictures of the test sections	49
3.4	LSU data points with the final visual observation of flow regimes.	50
3.5	Superficial fluid velocity ranges for the data considered in this work, including data produced at LSU.	51
4.1	Flow regimes of 695 experimental data points plotted against transition curves of flow regime maps by Duns and Ros [11], Aziz et al. [17], Mishima and Ishii [19], and Schlegel et al. [32].....	53
4.2	Slug flow development depending on pipe diameter.	56
4.3	Data points evaluated with CFD on Waltrich et al. [9] work plotted on newly proposed flow regime map.	58
4.4	CFD visualization of experimental data points reported by Ali and Yeung [24] presented in Table 4.2.	59
4.5	CFD visualization of experimental data points reported by Waltrich et al. [9] presented in Table 4.2.	59
4.6	Flow regime observation for Test 1 from Waltrich et al. [9] conditions.	60
4.7	Modified diagram proposed by this work for the model developed by Teles and Waltrich.	62

4.8	Proposed flow regime maps with all experimental data points produced at LSU, classified into the four flow regimes considered in this work, plus the data points without identified flow regimes	66
4.9	Comparison of errors in dp/dz calculation for the experimental data predicted to be in cap-bubble flow, simulated with different models.	67
4.10	Comparison of errors in dp/dz calculation for the experimental data predicted to be in be cap-bubble flow, simulated with different models. Only data without identified flow regimes from LSU were considered.....	69
4.11	Comparison of pressure gradient prediction accuracy between different models for conditions predicted as cap-bubble flow in the newly proposed flow regime map	69
4.12	Comparison of errors in pressure gradient calculation for the date reported by Asheim [65], simulated with the model by Teles and Waltrich and with the modification proposed in this work.....	70
4.13	Comparative of the effect of pressure on the critical mixture velocity for mixtures of (a) black oil and natural gas, and (b) water and air.	72
4.14	Example calculation of an equivalent property for a two-phase mixture being assumed as a homogeneous fluid.	73
4.15	Mixture critical velocity and void fraction relation for black oil and natural gas, and water and air mixtures. The considered conditions are a 9.62 MPa pressure and 15 °C temperature.	75
4.16	Representative model well in the Gulf of Mexico region during a blowout and the critical flow transition boundary considering a surface and sub-sea release.....	76
4.17	Surface release data points by Zulqarnain [3] plotted with Wallis [41] critical flow transition criteria and its modification by Beck et al. [61]	77
4.18	Proposed hybrid flow regime map with critical flow transition boundary.	78
4.19	Flow regime maps by (a) Mishima and Ishii [19]; and (b) Schelegel et al. [32].....	79

Abstract

Worst-case-discharge (WCD) calculations are a pre-requisite for any new well to be drilled in the Gulf of Mexico (GoM). Models that were mostly developed for production rates prediction are currently used to calculate the WCD rate. These models were mostly developed for pipe diameters and flow velocities much smaller than those expected during WCD events. Therefore, these models may be miscalculating WCD rates.

This study aims at analyzing one of possible sources of errors in these models: the flow regime maps. The influence of diameter change on flow regimes is discussed. A thorough literature review is carried out for different flow regime maps. These maps are tested against experimental data to define the best flow transition models. A new map with the best transition models is presented. A new flow regime is added to the map, replacing the slug flow: cap-bubble flow. This map is tested with numerical simulation to reproduce experimental and field conditions. In order to do this, a modification to a numerical model is proposed, coupling the new map to the model and the calculation of the pressure gradient when in cap-bubble flow. The results show improvement over the standard map.

Critical flow regime models and its existence during WCD are discussed. It is observed that it will be unlikely for the flow to be in critical conditions during a sub-sea release of deepwater wells, but it is possible that it happens during surface releases.

A series of future works is recommended.

Chapter 1

Introduction

Vertical gas-liquid two-phase upward flow can be found in a wide range of pipe diameters in many industrial applications such as in offshore risers in the petroleum industry, cooling towers in the nuclear industry, and in gas-liquid pipelines in petrochemical plants. A typical example of a problem that requires the knowledge about vertical two-phase upward flow in pipes is in worst-case-discharge (WCD) calculations. The Bureau of Ocean Energy Management (BOEM) defined the WCD rate as the maximum uncontrollable daily flow rate of hydrocarbons through an unobstructed wellbore [1]. In other words, WCD rate is the maximum expected flow rate during a blowout, considering the absence of an in-hole drillstring and a wellhead.

Recent new regulations require from any operator company planning to drill new wells in the Gulf of Mexico the submission of an Oil Spill Response Plan (OSRP), which should include a contingency plan to be followed in case of a blowout [2]. An estimative of WCD rate is required in this type of report. Two primary characteristics are expected during WCD events: high flow rates and large-diameter long-vertical pipes. Later OSRP reports present WCD flow rates in the Gulf of Mexico ranging from 0.63 to 75,678 m³/day (4 to 476,000 bbl/day), averaging for the Central Gulf of Mexico about 9,540 m³/day (60,000 bbl/day), and for the Western Gulf of Mexico about 2,225 m³/day (14,000 bbl/day) [2]. Furthermore, Zulqarnain [3] described a representative well configuration based on statistical analysis about the current wells in the Gulf of Mexico, in which the predominant pipe diameter is about 0.25 m (~10 in).

1.1 WCD rate calculation

In 2015, SPE released a technical report proposing a methodology for the calculation of WCD rates [1], based on a technique known as nodal analysis (see Figure 1.1), used in production rates estimation. The nodal analysis approach is dependent on reservoir characteristics and the pressure drop along the flowing wellbore. Figure 1.1.a shows a

schematic drawing of the components considered when using the nodal analysis method. It makes use of the inflow and outflow performance curves to calculate the flow rate of a well. Figure 1.1.b presents an example of how it is possible to graphically estimate the production rate by the use of these two curves. The inflow performance relationship (IPR) represents the fluid flow in the reservoir (fluid flow through a porous medium) and the outflow performance relationship, also known as tubing performance relationship (TPR), represents the wellbore (fluid flow in pipes).

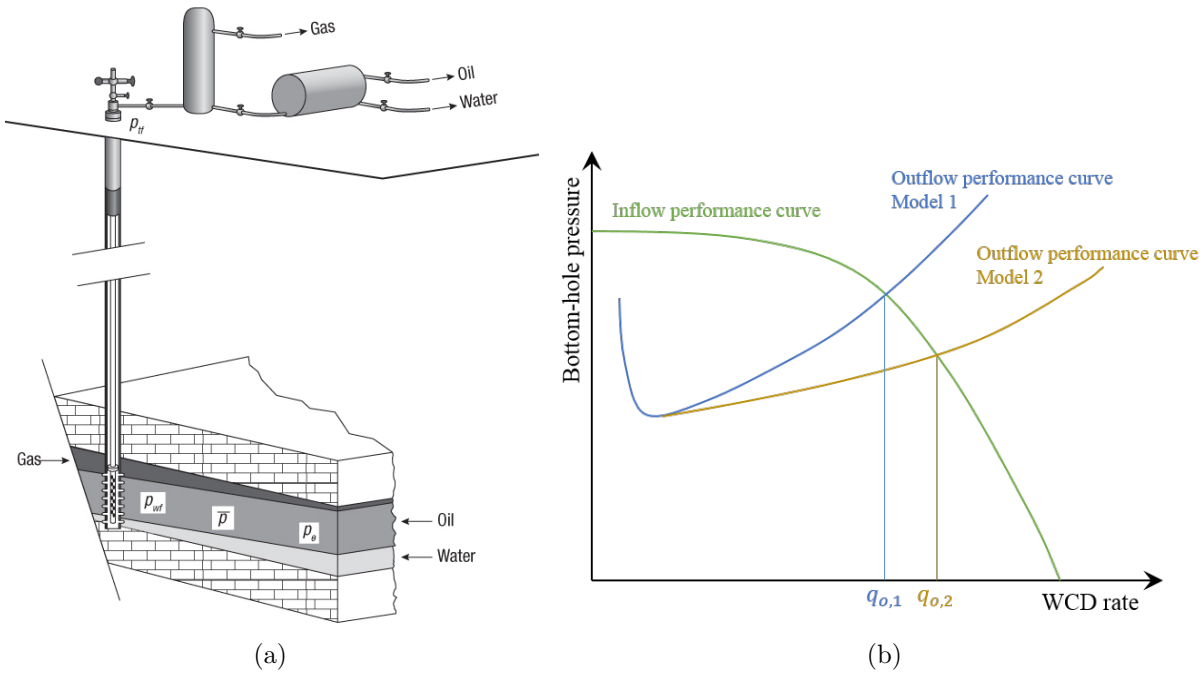


Figure 1.1. Elements required for the prediction of production rates, being (a) a schematic of a petroleum production system, including the reservoir, completion, well, wellhead assembly, and surface facilities [4], and (b) an example of a nodal analysis plot, including an inflow performance curve and two outflow performance curves, each one calculated using different models.

Petroleum production systems often deal with a relatively narrow range of wellbore pipe effective diameters, from 0.04 to 0.15 m (~ 1.5 to ~ 6 in), and liquid flow rates lower than 1,600 m³/day ($\sim 10,000$ bbl/day) [5]. On the other hand, WCD conditions involve higher liquid flow rates (possibly higher than 16,000 m³/day, or 100,000 bbl/day) and mostly larger pipe diameters (up to 0.50 m or ~ 20 in). Some recent studies [6, 7, 8] reported relevant differences concerning the multiphase flow dynamics in pipes with diameters larger than

0.10 m (~ 4 in). When not considered, flow behavior for larger diameters can be translated into erroneous predictions of pressure drops for the wellbore. These errors will appear as differences in the flow rate calculations, as shown in Figure 1.1.b. Thus, as the wellbore models (i.e., TPRs) used for WCD rate calculations were developed to calculate the outflow performance curves based on production conditions (being tested and verified only for lower rates and smaller diameters) the reliability of these models is still questionable [1].

Waltrich et al. [9] tested several different models used in WCD calculations against experimental pressure gradient data for vertical upward two-phase flow in large diameter pipes. Most models showed errors higher than 50% for the pressure gradient predictions. Thus, tracking the elements that could be driving those models to this high levels of errors is essential.

The present work will focus on one of the elements of wellbore flow modeling that may be causing the errors reported by Waltrich et al. [9]. One of the sources of the errors is possibly related to the flow regime prediction. Figure 1.2 presents a simplified diagram for the calculation of WCD rates. As shown in the figure, flow regime predictions can have a direct impact on WCD rate estimation.

1.2 Two-phase flow regimes in vertical pipes

The definition of flow regimes (sometimes called flow patterns) is an essential part of two-phase flow analysis [10]. Many multiphase flow models are flow regime dependent [11, 12, 13, 14]. Two-phase flow regime is described by Shoham [10] as a group of similar geometrical distribution of the gas and liquid phases in a pipe during a two-phase flow. Although it is possible to find several different vertical upward two-phase flow regimes characterizations throughout the literature (depending on the author), four flow regimes are most commonly defined, as shown in Figure 1.3.

These flow regimes can be described as [4, 15, 10]:

- Bubble flow: continuous liquid-phase upward stream, with dispersed gas phase flowing upward in the form of discrete bubbles.

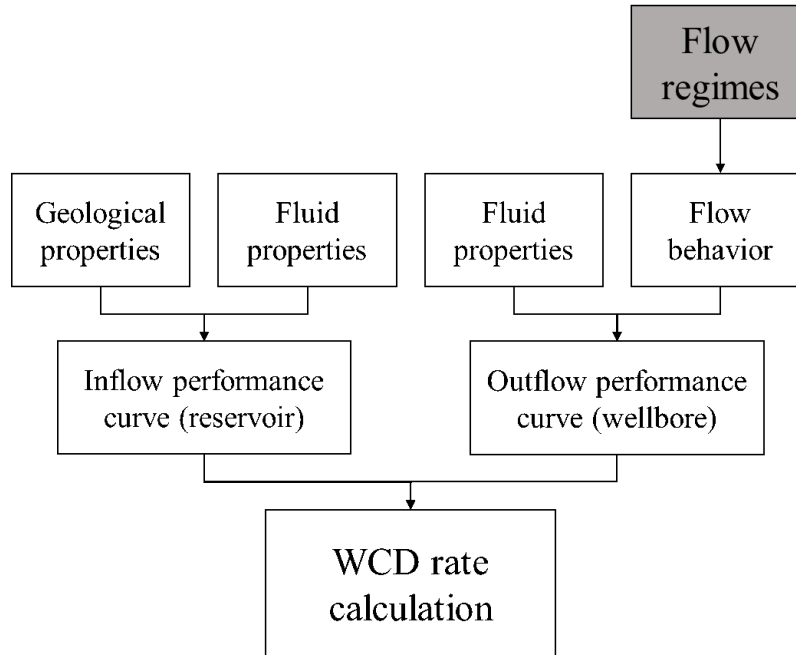


Figure 1.2. Simplified diagram for WCD rate calculation.

- Slug flow: a series of slug units characterize this flow. Each slug unit includes (i) a bullet shaped, axially symmetrical, gas pocket that occupies almost the entire diameter of the pipe, often called “Taylor bubble”; (ii) a liquid film flowing downward between the Taylor bubble and the pipe wall; and (iii) a liquid-phase plug below the Taylor bubble, with some smaller entrained gas bubbles.
- Churn flow: At intermediate gas flow rates, it becomes impossible for large bubbles to stay stable. Thus, Taylor bubbles breakdown and a very turbulent mixed flow are created, with no continuous phase, and highly oscillatory.
- Annular flow: gas-phase is converged into a continuous fast-moving gas core with some liquid-phase droplets entrained, while the liquid-phase forms a continuous film on the pipe wall, flowing upwards.

Flow regime maps are constructed to graphically determine the different flow regimes and their respective transition boundaries based on flow conditions. These maps usually are created based on the liquid and gas velocities or using dimensionless numbers, function

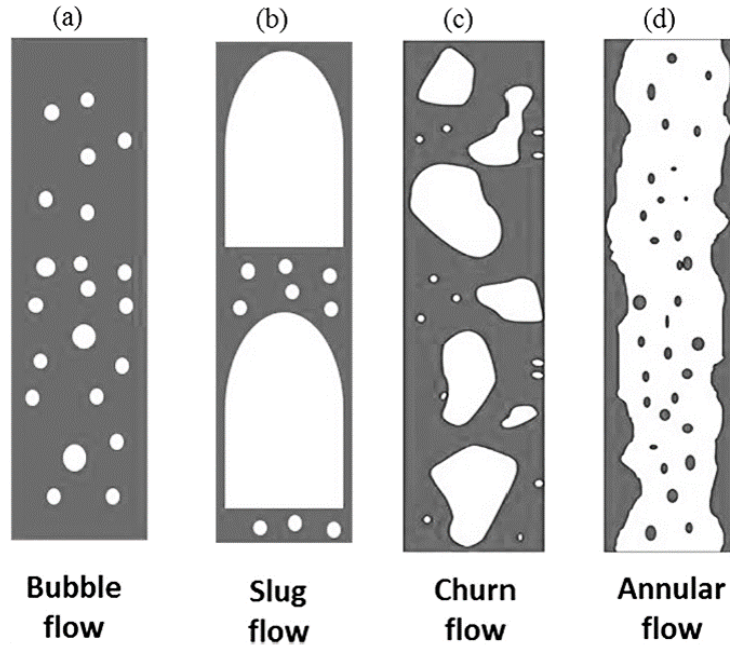


Figure 1.3. Visual representation of the four central flow regimes during upward flow in a vertical pipe, namely (a) bubble flow, (b) slug flow, (c) churn flow, and (d) annular flow (extracted from [16])

of liquid and gas velocities and other fluid properties or pipe characteristics. Figure 1.4 presents two relevant flow regime maps often cited on the literature, being (a) an empirical flow regime map developed by Aziz et al. [17], and (b) a mechanistic flow regime map proposed by Taitel et al. [18].

Flow regimes and their respective transitions are influenced by pipe geometry (diameters and inclination), fluid properties, and flow conditions [16]. Most flow regime maps [11, 18, 19, 20] developed for vertical two-phase flow in pipes are based on experimental and field data for small diameter pipes (e.g., ID < 0.10 m – or ~4 in) and low liquid flow velocities (liquid velocities typically lower than 1 m/s) [21, 22]. Thus, the applicability of such maps to flowing conditions involving large diameter and high flow velocities is still questionable. Therefore, studies are still needed on the evaluation of flow regime prediction models and proposing improvements for its application on WCD calculations.

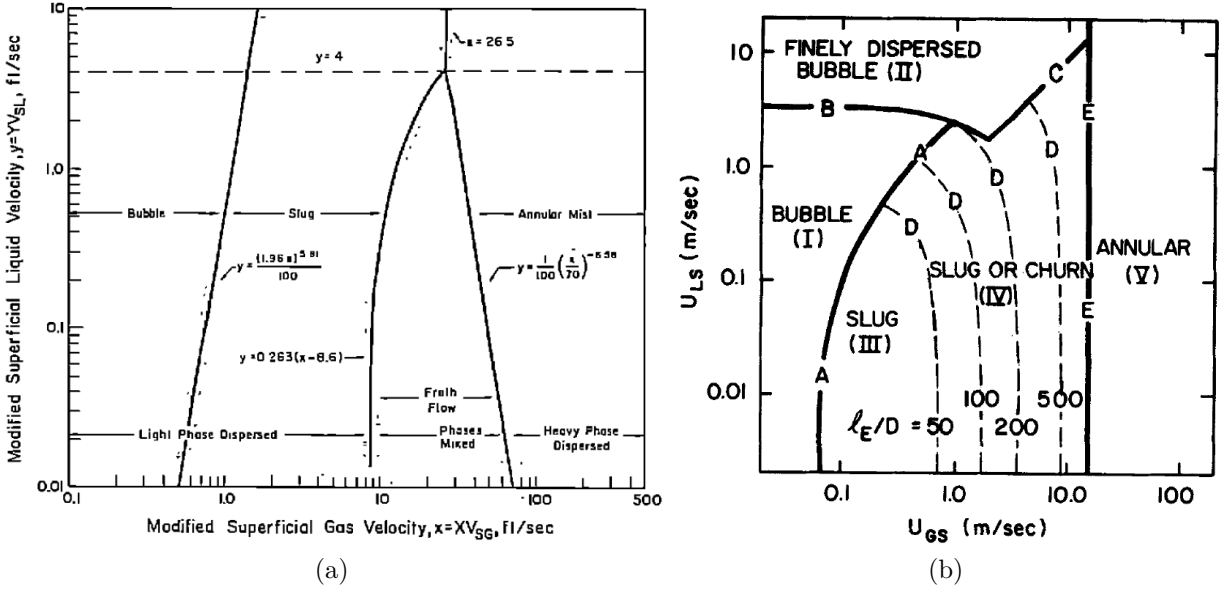


Figure 1.4. Flow regime maps: (a) Aziz et al. [17] empirical map, and (b) Taitel et al. [18].

1.3 Influence of pipe diameter on two-phase flow regimes

Some recent studies pointed out significant differences for flow regimes between large and small diameter pipes [23, 24, 16]. Among the main differences, the inexistence of slug flow in diameters larger than 0.10 m (~ 4 in) is reported by many authors [25, 26, 27, 23, 28, 6, 24, 16, 29].

Kataoka and Ishii [25] defined a dimensionless hydraulic diameter considering the surface tension and gas-liquid densities, which can be used to estimate the maximum possible hydraulic diameter for slug flow to occur in vertical two-phase flow in pipes. This dimensionless hydraulic diameter that defines the maximum diameter for stable Taylor bubbles is given by Kataoka and Ishii [25] as:

$$D_H^* = \frac{D_H}{\sqrt{\frac{\sigma}{g\Delta\rho}}} \quad (1.1)$$

where D_H is the hydraulic diameter, σ is the surface tension, and $\Delta\rho$ is the difference between the liquid and gas densities. This dimensionless diameter represents the force balance between the surface tension of the two interacting fluids and the pressure of the

liquid phase over the bubble, as shown in Figure 1.5.

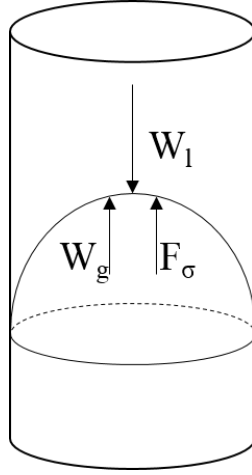


Figure 1.5. Force balance sustained in a Taylor bubble.

Kataoka and Ishii [25] claims that $D_H^* = 40$ is the maximum dimensionless diameter at which a Taylor bubble can be sustained, and slug flow can exist. This way, in this work, a large diameter pipe is defined as those with $D_H^* > 40$.

One interesting fact that should be noticed is how this dimensionless diameter behaves at larger pressures. Figure 1.6 shows the valued of D_H for $D_H^* = 40$ plotted as a function of pressure. When considering water and air at standard conditions, D_H is approximately 0.10 m (~ 4 in) for $D_H^* = 40$, and with higher pressures, D_H will slightly increase. However, when considering oil and gas, due to the decrease of oil surface tension with pressure, D_H will decrease with increasing pressure for $D_H^* = 40$, becoming as small as 0.025 m (~ 1 in) at about 10 MPa ($\sim 1,450$ psi). It should also be noticed that at atmospheric pressure D_H is approximately 7.5 cm (~ 3 in). Thus, when considering deepwater wells in the Gulf of Mexico, by definition, the sea floor is at least 330 m (1,000 ft) underwater [30], where pressures would be of about 3.2 MPa (~ 460 psi). Therefore, as it is highly unlikely to find production casings smaller than 0.07 m (~ 2.75 in) in the GoM, most will probably have large-diameter pipes without the existence of slug flow during WCD rate calculations. Although it might be counterintuitive, relevant experimental investigations in the literature also indicate the non-observation of slug flow in large diameters using the concept proposed

by Kataoka and Ishii [25] for $D_H^* > 40$.

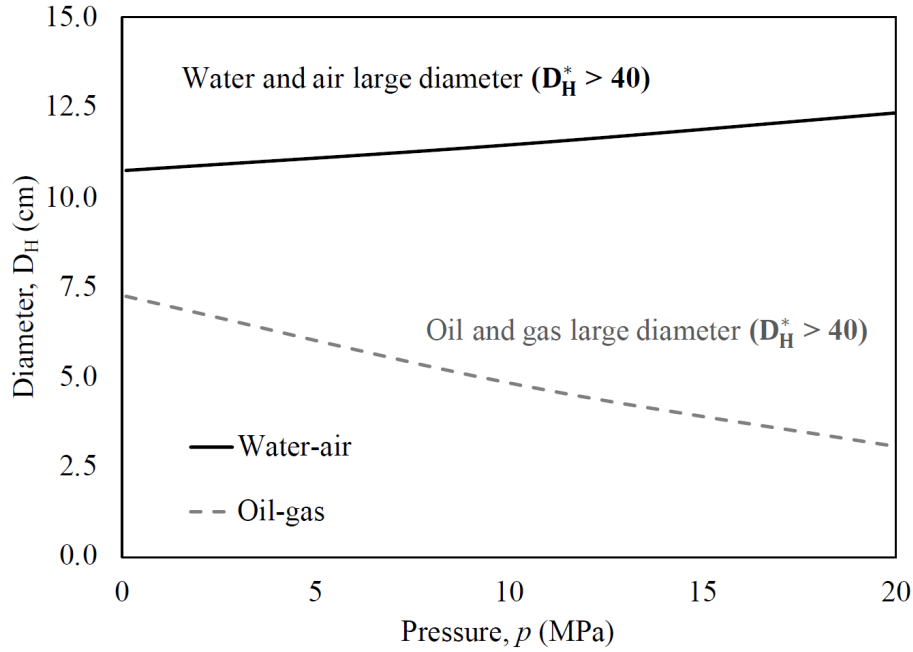


Figure 1.6. Separation of what is considered a large diameter pipe by Kataoka and Ishii [25] criteria. The area above the curves represent the diameters considered large.

For instance, Ros [31] carried out experiments for pipe diameters from 0.03 to 0.14 m (~ 1 and ~ 5.5 in), using air and diesel oil as working fluids, under atmospheric pressure. In his work, he refers to slug flow as the result of the collapsing of bullet-shaped gas bubbles, and even considers their so-called “slug flow” to directly precede the mist flow (equivalent to annular flow). They also report that the bullet-shaped bubbles were only visible for liquid superficial velocities lower than 40 cm/s (~ 15.7 in/s).

Some authors reported that under conditions at which slug flow would exist, in larger diameter pipe it will be replaced by a flow regime characterized by large deformed bubbles flowing upwards or sideways. This flow regime has been commonly referred to as cap-bubble flow [23, 32, 24]. This flow regime definition will be used throughout this work.

A schematic of the cap-bubble flow is presented in Figure 1.7. This flow regime is defined as [23]:

- Cap-bubble flow: bubbles larger than those seen on bubble flow start to form, but never occupying the entire pipe diameter. These bubbles generate flow recirculation

and increased turbulence

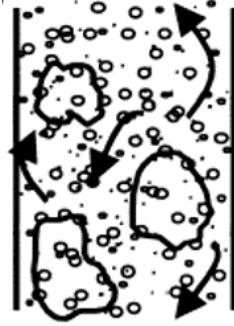


Figure 1.7. Cap-bubble flow, adapted from Ohnuki and Akimoto [23].

Considering that the highest errors found on the simulations calculated by Waltrich et al. [9] were for flows on conditions where slug flow would typically exist in smaller diameter pipes, it is inevitable to think that the use of slug flow models where cap-bubble flow exist could be one of the sources of the error reported in that work. Therefore, this study will investigate the effect of include cap-bubble flow regimes on calculations of wellbore flow for WCD conditions (e.g., for large diameters and high-velocity flows, using hydrocarbon oil and gas at high pressures).

1.4 Statement of the problem and objectives

With the development of deepwater offshore oil explorations and new safety requirements, it became imperative to understand two-phase flow in large diameter pipes and high-velocity flows for oil-and-gas in wellbores. Considering that the current models developed to predict two-phase flow behavior are mostly based on small diameter pipes, and their accuracy in large diameter pipes is not well known (Waltrich et al., [9]), it is necessary that studies are carried out to investigate the sources of errors and improve or create new and more adequate wellbore flow models for WCD rate estimation.

Waltrich et al. [9] noticed that one of the possible sources of errors is the use of inaccurate flow regime maps and flow regime transition models. It has been shown in the literature that some of the differences between flows in large and small diameters, including the inexistence of slug flow and three-dimensional effects, can drastically change flow regime

determination [25, 23, 14, 8, 29].

As mentioned before, flow regimes are dependent on fluid properties and have an essential dependence on the gas-liquid volume fraction in the flowing mixture. The gas-liquid-ratio will strongly influence the pressure drop of the flow. Consequently, flow-regime dependent models will calculate the pressure gradient in different ways for different flow regimes. For example, a flow regime with low gas-liquid-ratio will have a higher density than a flow regime with high gas-liquid-ratio and therefore, will cause a higher pressure drop due to gravitational forces. On the other hand, in flow regimes with high gas-liquid-ratio, the tendency is that the flow is at a higher velocity (due to the gas expansion tendency with reducing pressure), and will present a higher pressure drop due to friction. This way, a right prediction of flow regime is essential when calculating the pressure gradient for vertical upward two-phase flow.

Figure 1.8 shows a schematic of two-phase flow in a vertical pipe, including the expected pressure profiles considering different flow regimes. As fluid mixture flow upwards, the gas expands and increases its gas velocity (as a consequence of mass and momentum conservation). This increase in gas velocity will make the bubbles coalesce and cause flow regime transitions. If a model is considering erroneous flow regimes transition, there is a chance that the final calculated pressure drop is also wrong. As shown in Figure 1.8, changing the condition to which a flow regime will change, or the expected pressure drop for different flow regimes, as for flow regime maps 1 and 2, the final calculated pressure (in this case, the bottom-hole pressure) will be different. Hence, the more precisely you can predict the flow regime, the more accurate will be the final pressure calculation. It is interesting to notice that if using the criteria of large diameter by Kataoka and Ishi [25], it is possible to have a transition to from cap-bubble to slug in the same wellbore due to pressure drops with the upwards flows, even without changing the pipe diameter (see Figure 1.6). In other words, if the pressure drops enough, and the flow is in the right conditions, the pipe might “become” small enough for the existence of slug flow.

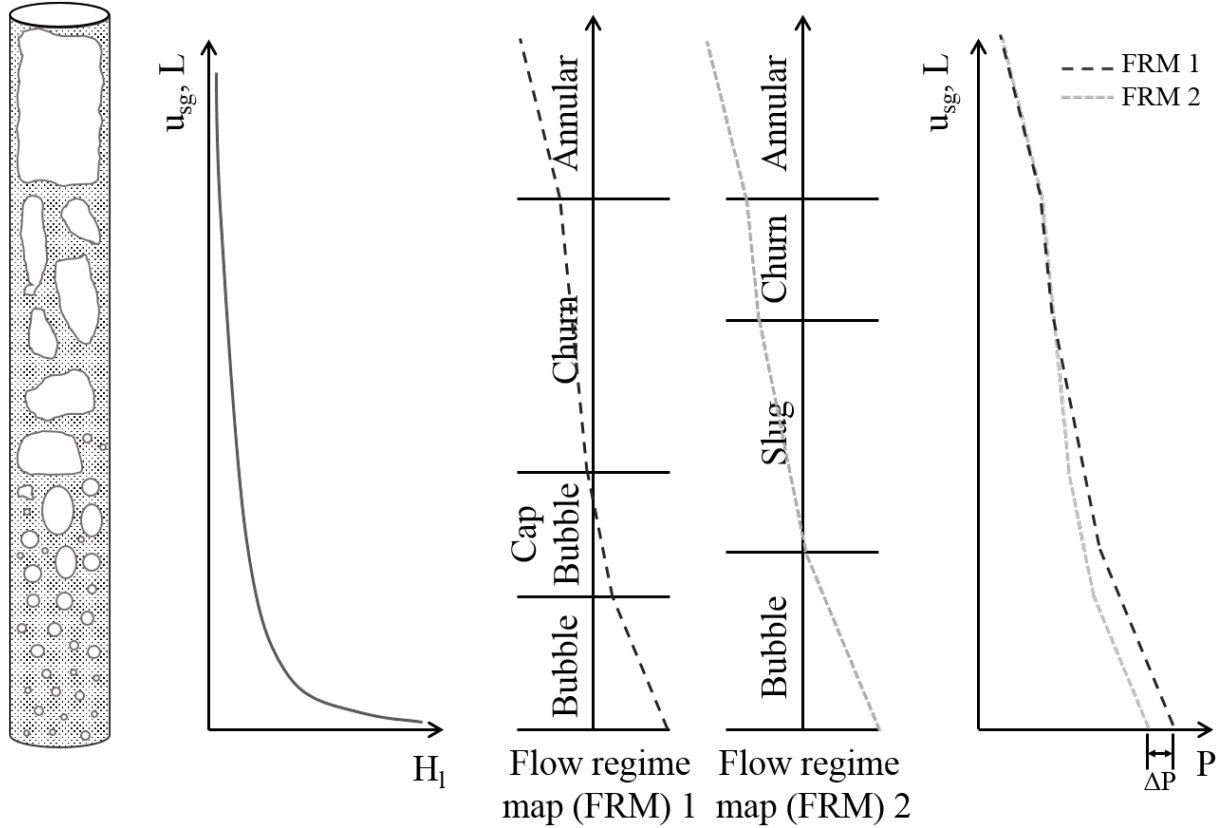


Figure 1.8. Flow regime progression with increasing height along the wellbore and estimated pressure profiles considering different flow regimes along the flow.

As there is not an agreement on the literature as which flow regime to use for WCD conditions (which include flows in large diameter and high velocities), the objective of this work is to investigate the use of flow regime maps and transition criteria for large diameter and high velocity flows. This primary objective is achieved by accomplishing five tasks:

1. Extract experimental data of two-phase flow in large diameter pipes characterization on a broad range of velocities from the literature, including data of flow regime observation and pressure gradient measurements;
2. Produce experimental data on two-phase flow in vertical pipes with $D_H^* > 40$ and high flow velocities;
3. Analyze existent flow regime maps and transition criteria;

4. Compare existent flow regime maps against experimental data flow in large diameter pipes and high flow-velocities;
5. Propose or develop an adequate flow regime map for large diameter pipes, and high velocity flows and test it in a model to evaluate if it improves or not the pressure drop estimation.

Chapter 2

Literature Review

2.1 Important parameters for two-phase flow in pipes

Some relevant parameters are unique in the analysis of two-phase flow phenomena. These parameters are defined below and will be used throughout this work [10]:

- Liquid holdup (H_l): can be defined in steady-state flows as the time-averaged volumetric fraction of liquid-phase in a pipe segment.
- Void fraction (α) or gas holdup ($H - g$): such as the liquid holdup, can be defined in steady-state flows as the time-averaged volumetric fraction of gas-phase in a pipe segment. The liquid holdup and void fraction can be correlated as:

$$\alpha + H_l = 1$$

- Pressure gradient (dp/dz): pressure variation along the axial direction in a pipe.
- Superficial velocity (u_{sl} for liquids and u_{sg} for gases): geometrical parameter correlation the injected volumetric flow rate and the pipe cross-section. Can be calculated as

$$u_{sn} = \frac{Q_n}{A}$$

where the subscripts s represents that the velocity u is superficial, and n refers to the considered fluid (replaced by l for liquids and g for gases), Q is the volumetric flow rate and A is the cross-section of the pipe.

- Mixture velocity (u_m): the sum of liquid and gas superficial velocities.
- Slip ratio (u_{sg}/u_{sl}): the ratio between gas and liquid superficial velocities.

2.2 Teles and Waltrich model [33] (or modified Pagan et al. [34])

A new wellbore two-phase flow model to estimate pressure gradient for the four classical flow regimes (bubble, slug, churn, and annular flow) in large diameter pipes has been developed at LSU and recently proposed in an interim report by LSU and submitted to BOEM [33].

The model herein called Teles and Waltrich [33] is a modification to the model proposed by Pagan et al. [34] for churn and annular flow, coupled with Duns and Ros [11] empirical correlations to calculate bubble and slug flow. Furthermore, this new model makes use of Eq. 1.1 to evaluate whether the pipe will be considered as large or not and, consequently, if it will present slug flow. The model also adds a criteria that for any flow with a slip ratio lower than 1, Duns and Ros [11] should be automatically selected, not mattering at which flow regime the flow is. The model is also adequate to calculate the pressure gradient in small diameter pipes, making use of Duns and Ros [11] model in such cases.

The flowchart shown in Figure 2.1 illustrates how the algorithm of this model works for the calculation of pressure in each section of the well, being deployed for each length increment from a known pressure. The initial conditions and input parameters are an initial conditions (wellhead pressure, fluids flow rates, temperatures), fluid properties (gas-liquid ratio, fluid densities), well parameters (inclination, diameter, vertical length), and the desired number of finite length increments.

This model was tested against other relevant models [11, 35, 36, 12, 13, 37] with good results, showing average absolute errors on the pressure gradient estimation comparable to all these other relevant models. A comparative between the error from the calculation of the pressure gradient by Teles and Waltrich model and others is presented in Figure 2.2. The data used for these simulations can be found in the Appendix, in Table A.1. A full review of these results and more is reported in the Interim report from LSU to BOEM [33].

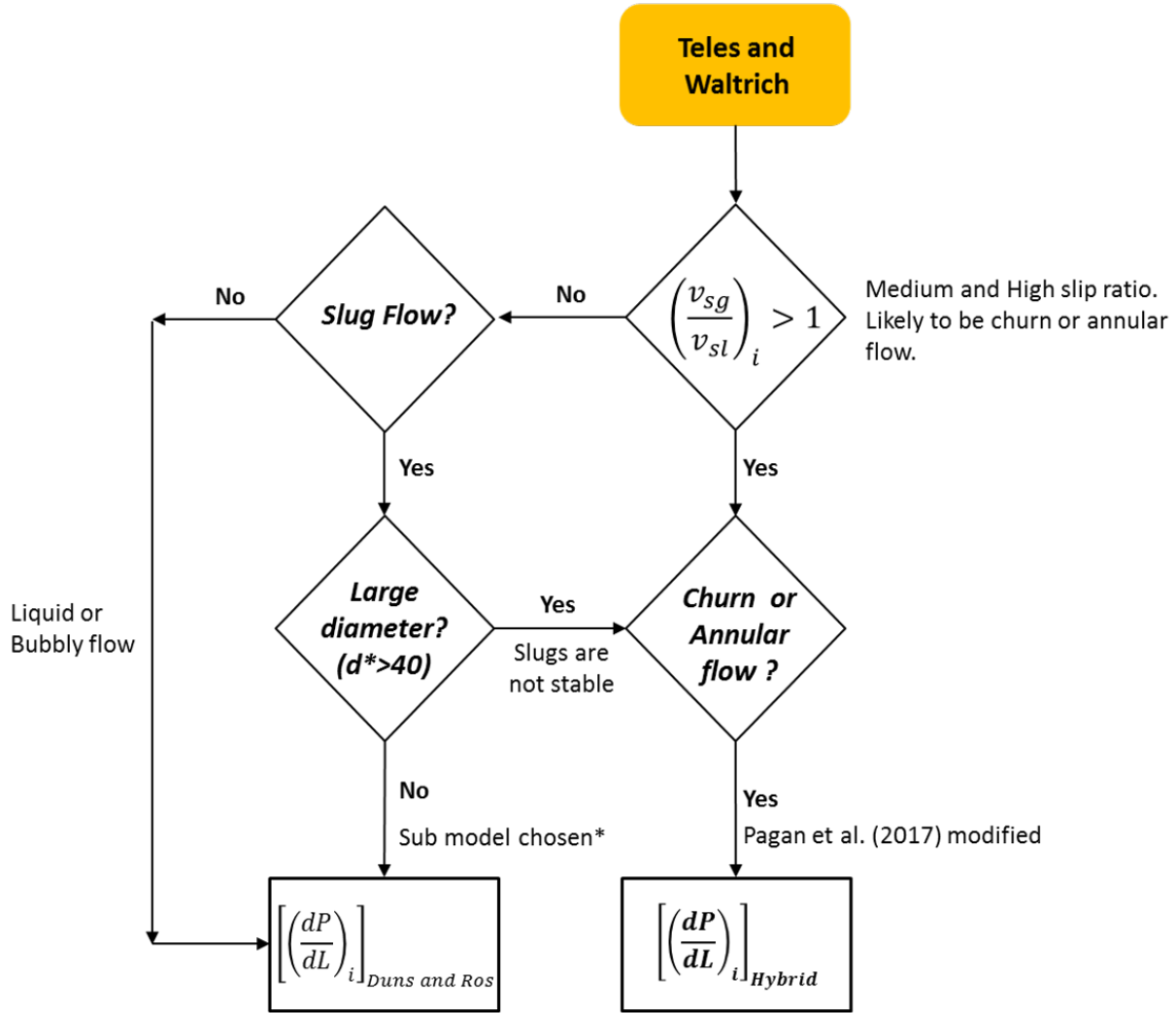


Figure 2.1. Teles and Waltrich model workflow [33].

2.3 Pagan et al. [34] model

The model proposed by Pagan et al. [34] was developed to calculate the pressure gradient for churn and annular flow, based on an approach first proposed by Jayanti and Brauner [39]. The latter model was validated for pipes with $D_H^* < 40$. The approach considers the phases separately, with a gas core centered within a control volume. The pressure drop is calculated as the result of the force balance on a gas core with length dl and cross-sectional area A_c , as presented in Figure 2.3: Force balance for a pipe segment for churn and annular flow regimes on (a) gas core and (b) total cross-sectional area (including liquid film and gas core).

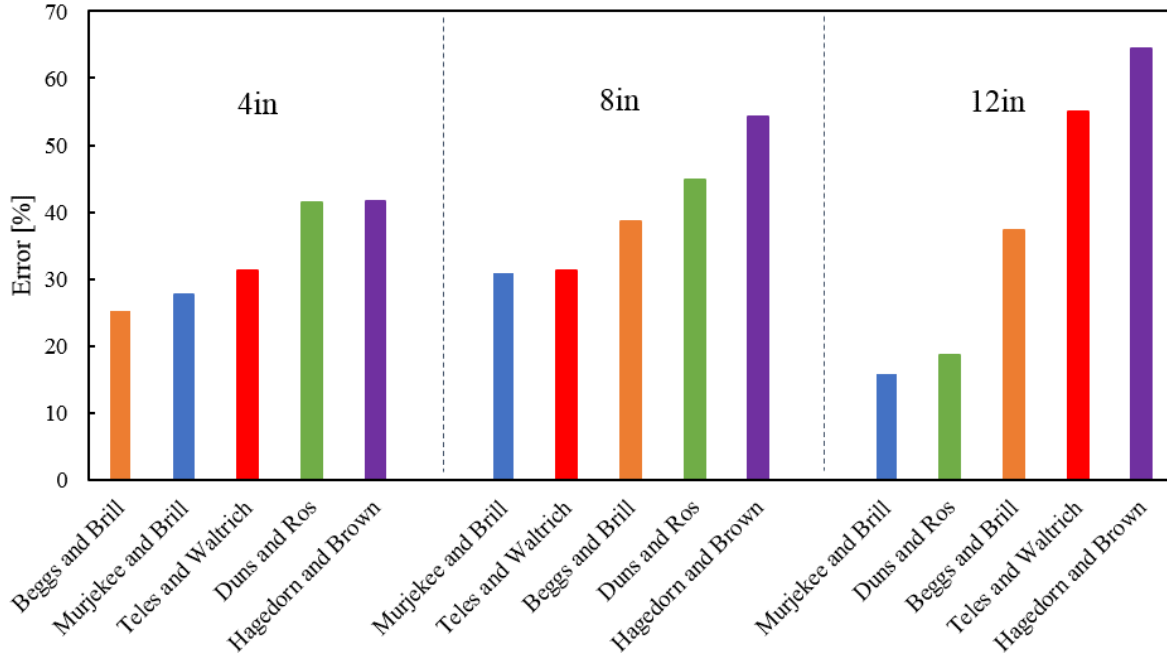


Figure 2.2. Average Absolute Error of pressure gradient in % for Teles and Waltrich [33], Duns and Ros [11], Beggs and Brill [36], Murkherjee and Brill [38], and Hagedorn and Brown [35] models for 0.10, 0.20, and 0.30 m ID pipes for the LSU/PERTT Lab experimental data reported by Waltrich et al. [9]. Figure extracted from [33].

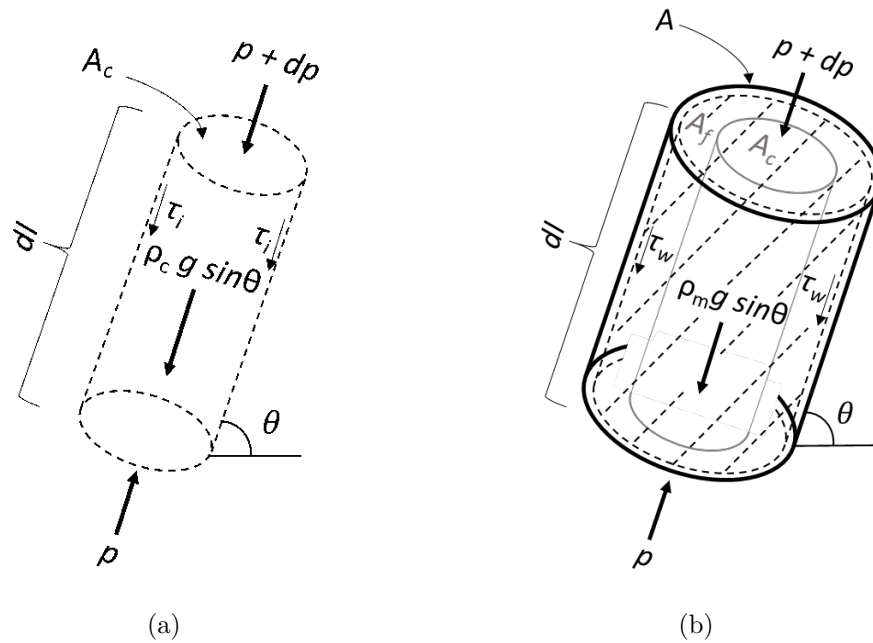


Figure 2.3. Force balance for a pipe segment for churn and annular flow regimes on (a) gas core and (b) total cross-sectional area (including liquid film and gas core).

In the churn flow regime, strong oscillation is expected. Nevertheless, the net liquid rate is upward. Differently than in churn flow, during annular flow, it is assumed only upward flow for both gas and liquid phases. For this reason, Jayanti and Brauner [39] proposed that the average wall shear stress should be calculated based on the net liquid flow rate, neglecting the liquid flow variation with time. Therefore, Pagan et al. [34] assumes that both phases flow upwards, with the shear stress, τ_i , at the gas-liquid interface representing the interaction between the phases and the wall shear stress (see Figure 2.3.a), τ_w , representing the force acting between the liquid phase and the pipe wall (see Figure 2.3.b). Neglecting the kinetic energy term, the momentum balance equation of these components is given by Jayanti and Brauner [39] as:

$$-\frac{dp}{dL} = \frac{4\tau_i}{D\sqrt{\alpha}} + \rho_g g \sin \theta \quad (2.1)$$

and

$$-\frac{dp}{dL} = \frac{4\tau_w}{D} + [\rho_g \alpha + \rho_l(1 - \alpha)]g \sin \theta \quad (2.2)$$

where dp/dL is the pressure gradient for the pipe segment dL , g is the gravitational acceleration, D is the diameter of the section, θ is the inclination angle with the horizontal, α is the void fraction, ρ_g and ρ_l are the gas and liquid densities. It is possible to solve Eqs. 2.1 and 2.2 for dp/dL and α .

The wall shear stress, τ_w , is calculated from the following relationship for both annular and churn flow regimes,

$$\tau_w = \frac{1}{2}\rho_l f_l \left(\frac{u_{sl}}{1 - \alpha} \right)^2 \quad (2.3)$$

where u_{sl} is the superficial liquid velocity, and f_l is the friction factor of the liquid film. Eq. 4 represents the wall shear stress for single-phase flow, considering that only the liquid

phase is in contact with the pipe wall.

The liquid film friction factor can be considered as Fanning friction factor, f , which can be calculated by a Blasius-type equation, as

$$f = CRe_{lf}^{-n} \quad (2.4)$$

where Re_{lf} is the Reynolds number of the liquid film, and n and C are constants dependent on flow conditions, i.e., if it is turbulent or laminar. The flow will be considered laminar if the Reynolds number is smaller than 2,100, and turbulent if it is greater than 2,100. This way, $n = 1$ and $C = 16$ for laminar flow, and $n = 0.2$ and $C = 0.046$ for turbulent flow.

The Reynolds number for the liquid film can be calculated as:

$$Re_{lf} = \frac{\rho_l u_{lf} D}{\mu_l} \quad (2.5)$$

where D is the pipe diameter, μ_l is the liquid viscosity, and u_{lf} is the liquid film velocity given by:

$$u_{lf} = \frac{u_{sl}}{1 - \alpha} \quad (2.6)$$

The interfacial shear stress between the gas core and the liquid film shown in Figure 2.3.a is calculated as:

$$\tau_i = \frac{1}{2} \rho_g f_i \left(\frac{u_{sg}}{\alpha} \right)^2 \quad (2.7)$$

where u_{sg} is the superficial gas velocity. Eq. 2.7 neglects the liquid superficial velocity component for considering that the superficial gas velocity is much higher during churn or annular flows. This way τ_i is calculated considering a single-phase gas flow.

Pagan et al. [34] calculate the interfacial friction factor as proposed by Jayanti and Brauner [39] as:

$$f_i = \frac{1}{2}(f_{i,W} + f_{i,B}) \quad (2.8)$$

A correlation suggested by Alves [40] is used to calculate $f_{i,B}$, given by:

$$f_{i,B} = 0.005 + 10^{\left(-0.56 + \frac{9.07}{D_H^*}\right)} \left[\frac{D_H^*(1 - \alpha)}{4} \right]^{\left(1.63 + \frac{4.74}{D_H^*}\right)} \quad (2.9)$$

where D_H^* is the dimensionless diameter calculated by Eq. 1.1. Pagan et al. [34] suggest the calculation of $f_{i,W}$ using the general equation for interfacial friction factor introduced by Wallis [41] as:

$$f_{i,W} = 0.005 \left(1 + 300 \frac{\delta}{D} \right) \quad (2.10)$$

where δ/D is the dimensionless liquid film thickness. The latter term on the RHS can be represented in terms of α , as it can be calculated as the ratio between the cross-sectional area of the gas core, A_c , and the cross-sectional area of the pipe A. Thus, this study proposes Wallis [41] modified interfacial friction factor without assumption of thin liquid film in pipes for churn flow regime, given by:

$$f_{i,W} = 0.005 + 0.75(1 - \sqrt{\alpha}) \quad (2.11)$$

Wallis [41] modified interfacial friction factor equation with the assumption of the thin liquid film is used only for annular flow regime, and is given by:

$$f_{i,W} = 0.005 + 0.375(1 - \alpha) \quad (2.12)$$

2.4 Duns and Ros [11] model

Duns and Ros [11] developed an empirical model, based on a proprietary flow regime map. Duns and Ros [11] empirical map separate flow regimes into three regions (see Figure 2.4), sometimes englobing more than one flow regime at a time. These regions are

categorized based on the dominant fluid phase of the flow, and are defined as:

- Region I: continuous liquid-phase. This region includes the classical flow regimes of bubble and part of churn, while also containing the so-called plug flow regime, which will be considered equivalent to cap bubble flow regime in this work;
- Region II: alternating liquid and gas-phases. An unstable and pulsating character describes the flow conditions in this region. This region includes the rest of churn flow and slug flow regimes; Transition region: the area between Region II and III, where no dominance by any of the two is seen. Duns and Ros [11] says its properties are an interpolation between Region II and III.
- Region III: continuous gas-phase. This region includes the annular flow regime.

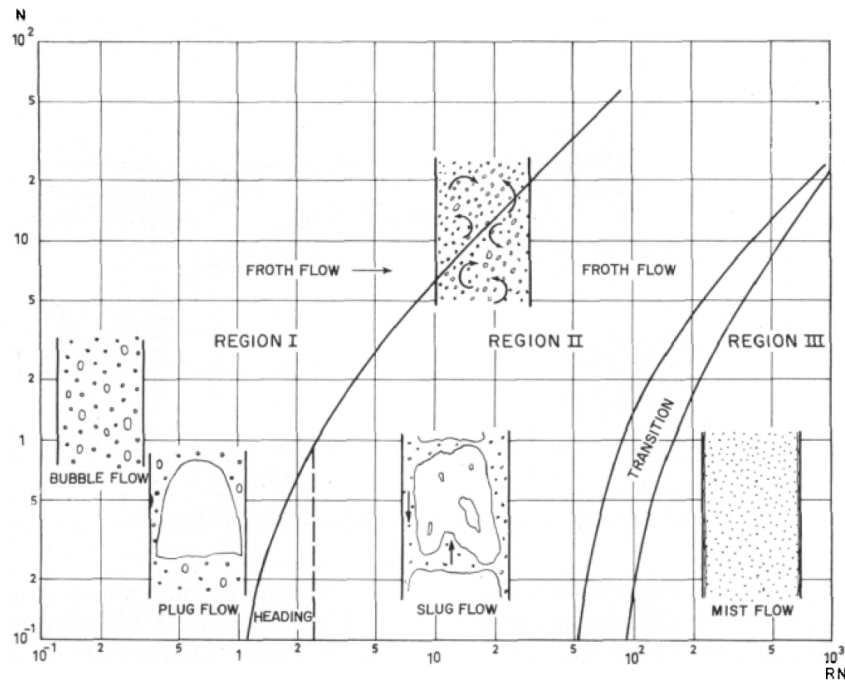


Figure 2.4. Empirical flow regime map by Duns and Ros [11]

Duns and Ros [11] two-phase flow empirical model for pressure drop along the wellbore is a result of an exhaustive laboratory study of 4,000 two-phase flow tests. The experiments were carried out in vertical pipes with diameters ranging from 1.26 to 5.60 inches for

gas-water flow [15], and gas-diesel oil flows. The modified Pagan et al. [34] model, herein called Teles and Waltrich model makes use of Duns and Ros [11] correlations for bubble and slug flow due to its good accuracy on predicting pressure drop in these flow regimes for air-water and gas-oil fluids, for a wide range of pipe diameters.

To account for fluid and flow conditions, Duns and Ros [11] make use of dimensionless numbers to place the flow into the flow regime map. The dimensionless liquid and gas velocity numbers are respectively defined as:

$$RN = u_{sg}\sqrt{\rho_l/(g\sigma)} \quad (2.13)$$

$$N = u_{sl}\sqrt{\rho_l/(g\sigma)} \quad (2.14)$$

where ρ_l is the liquid density.

The map is then built plotting RN as the x-axis and N as the y-axis, and the transition boundaries are empirically placed.

The Region I to Region II transition describes the change from a continuous liquid flow to intermittent flow. The boundary between these two regions can be calculated as:

$$RN = L_1 + L_2N \quad (2.15)$$

Where L_1 and L_2 are graphically given in Figure 2.5 and dependent on a dimensionless diameter number, defined as:

$$N_d = D\sqrt{\rho_l g/\sigma} \quad (2.16)$$

The next transition with increasing gas flow rates happens from Region II to transition zone when:

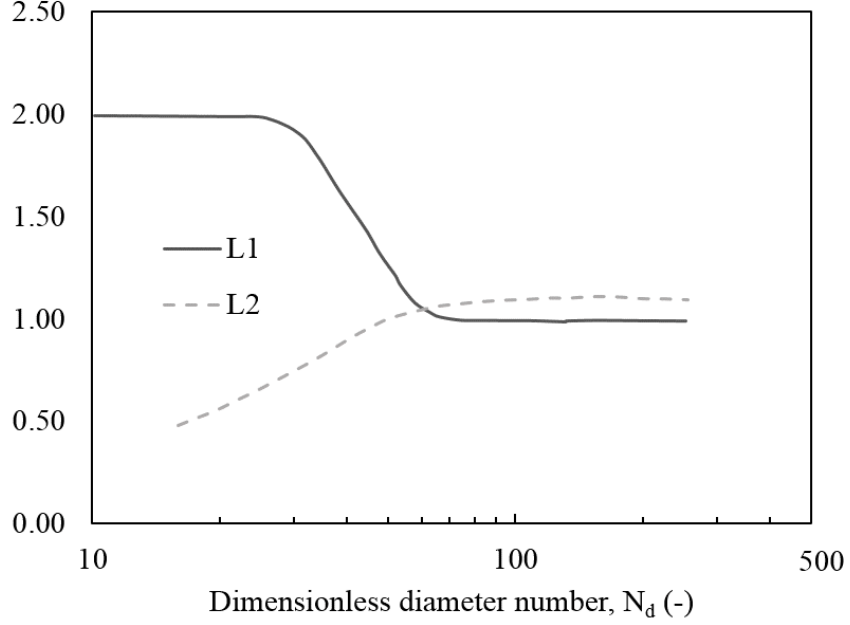


Figure 2.5. L1 and L2 factors versus dimensionless diameter number (N_d) [11].

$$RN = 50 + 36N \quad (2.17)$$

Finally, with a higher gas flow rate, the flow leaves the transition zone to Region III when:

$$RN = 75 + 84N^{0.75} \quad (2.18)$$

Duns and Ros [11] model calculates the pressure gradient for the flow depending in which region the flow is placed in their map. The pressure gradient as calculated by Duns and Ros as the sum of a static and f friction gradients, as:

$$G = G_{st} + G_{fr} \quad (2.19)$$

where G_{st} and G_{fr} are the static and friction gradients, respectively.

The G_{st} is dependent on the liquid holdup, and can be calculated as:

$$G_{st} = \frac{1}{\rho_l g} \left(\frac{dp}{dz} \right)_{st} = H_l + (1 - H_l) \frac{\rho_g}{\rho_l} \quad (2.20)$$

The liquid holdup is proportional to the slip velocity, u_s , defined as the difference between the actual gas and liquid velocities, defined as:

$$u_s = \frac{u_{sg}}{1 - H_l} - \frac{u_{sl}}{H_l} \quad (2.21)$$

This slip velocity can be non-dimensionalized, as the other groups as:

$$S = u_s \sqrt{\rho_l / (g\sigma)} \quad (2.22)$$

Therefore, by defining S it is possible to calculate H_l and, consequently, G_{st} .

Duns and Ros [11] propose an empirical formula to calculate S according to the different Regions in their map.

The empirical formula for Region I is:

$$S = F_1 + F_2 N + F'_3 \left(\frac{RN}{1 + N} \right)^2 \quad (2.23)$$

This formula correlates the empirical F-factors with the dimensionless liquid and gas velocities N and RN, respectively. The F-factors for this region can be obtained from Figure 2.6 using the dimensionless liquid viscosity number defined as $N_l = \mu_l \sqrt{\rho_l / (g\sigma^3)}$. It is important to notice that F_3 is given in the plot, but F'_3 can be calculated as:

$$F'_3 = F_3 - \frac{F_4}{N_d} \quad (2.24)$$

For Region II, the empirical correlation for the dimensionless slip velocity number can be had as:

$$S = (1 + F_5) \frac{(RN)^{0.982} + F_6}{(1 + F_7 N)^2} \quad (2.25)$$

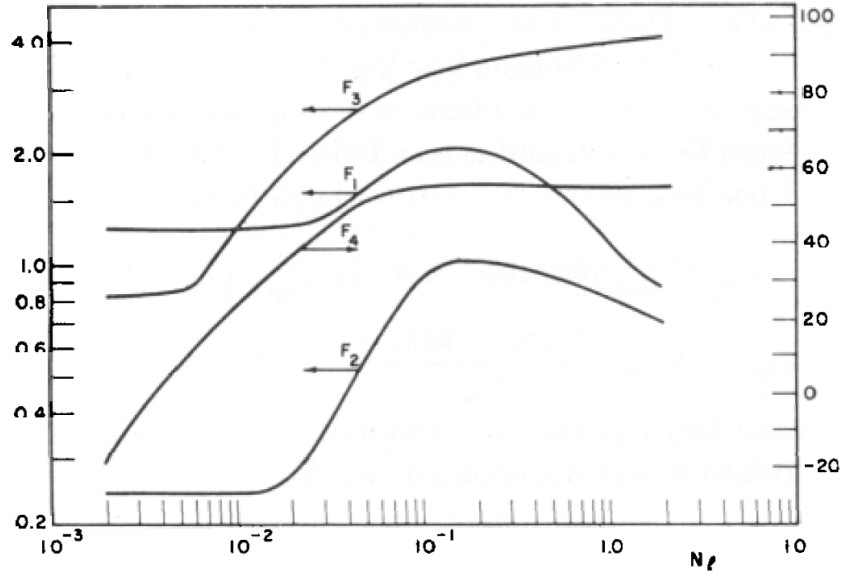


Figure 2.6. F-factor numbers for Region I, based on the dimensionless viscosity number N_l [11].

As for the previous region, the F-factors can be had from a plot according to N_l . This plot is presented in Figure 2.7.

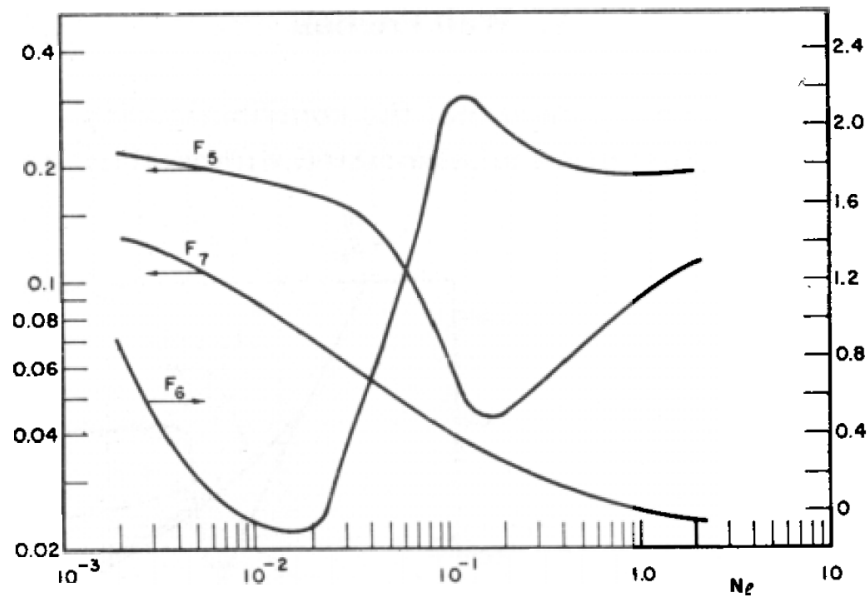


Figure 2.7. F-factor numbers for Region II, based on the dimensionless viscosity number N_l [11].

The parameter F'_6 will be calculated from F_6 as:

$$F'_6 = 0.029N_d + F_6 \quad (2.26)$$

For Region III it is considered that the liquid is being mainly transported as small droplets by the continuous gas phase. Therefore, $S = 0$.

The friction gradient, G_{fr} , for Regions I and II can be had as:

$$G_{fr} = \frac{1}{\rho_l g} \left(\frac{dp}{dz} \right)_{fr} = 4f_w \frac{u_{sg}^2}{2gD} \left(1 + \frac{u_{sg}}{u_{sl}} \right) = 2f_w \frac{N(N + RN)}{N_d} \quad (2.27)$$

where f_w is a empirical friction factor defined as:

$$f_w = f_1 \frac{f_2}{f_3} \quad (2.28)$$

and the f-factors are a function of Re_l . The factor f_1 is given in Figure 2.8.

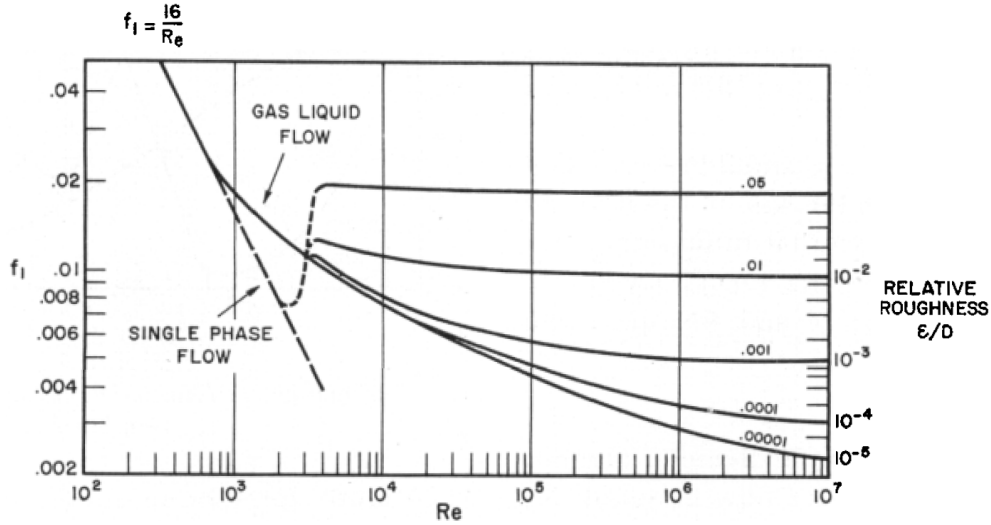


Figure 2.8. Dimensionless f_1 factor as a function of Re and relative roughness ε/D [11].

The factor f_2 is a correction for the in-situ gas-liquid ratio, $R = u_{sg}/u_{sl}$, and is given in Figure 2.9 as a function of the group $f_1 RN_d^{2/3}$

The dimensionless factor f_3 is a farther correction for both liquid viscosity and in-situ gas-liquid ratio and can be calculated as:

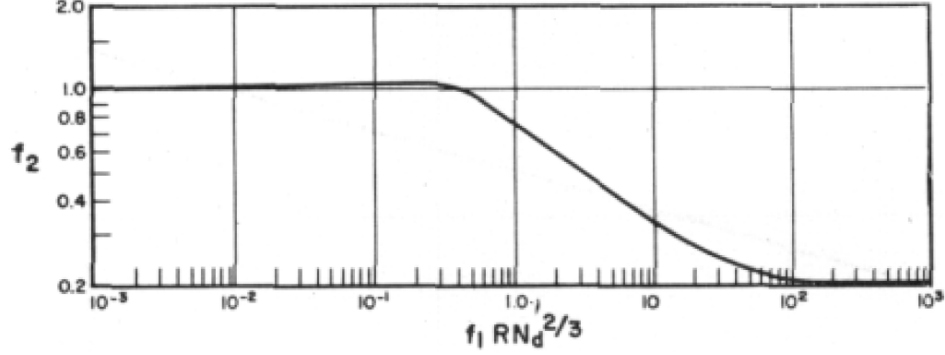


Figure 2.9. Dimensionless f_2 factor as a function of the group $f_1 RN_d^{2/3}$ [11].

$$f_3 = 1 + f_1 \sqrt{R/50} \quad (2.29)$$

For region III, the friction gradient is calculated as:

$$G_{fr} = \frac{1}{\rho_l g} \left(\frac{dp}{dz} \right)_{fr} = 4f_w \frac{\rho_g}{\rho_l} \frac{u_{sg}^2}{2gD} = 2f_w N_\rho \frac{(RN)^2}{N_d} \quad (2.30)$$

Now, however, the slip is absent and will be given as:

$$f_w = f_1 \quad (2.31)$$

with f_1 coming from Figure 2.8. Nevertheless, the input parameter roughness ε , in Figure 2.8 will be the roughness of the liquid film that covers the wall of the pipe. This roughness can be calculated by the use of the Weber number, We , given as:

$$We = \frac{\rho_g u_{sg}^2 \varepsilon}{\sigma} \quad (2.32)$$

and Figure 2.10.

2.5 Flow regime maps

A variety of flow regime maps are available in the literature, but most of them were developed for small diameter pipes (e.g., $D_H^* < 40$).

Wu et al. [16] carried a comprehensive critical review of factors that influence flow

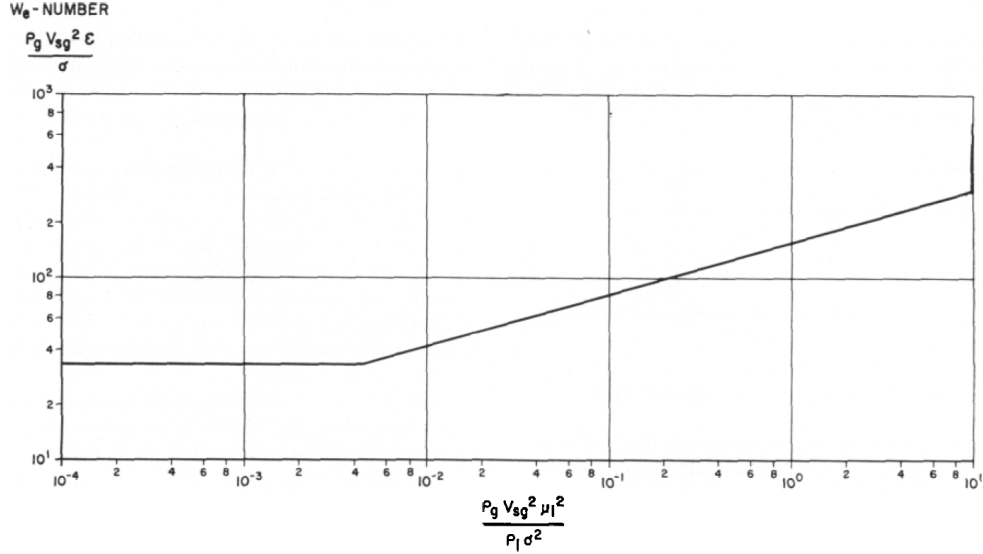


Figure 2.10. Correlation for the film-thickness ε under mist-flow conditions [11].

regimes in multiphase flows. They examine the effect of pipe diameters and deviation from the vertical direction, viscosity, and salinity of the mixture. They also evaluate current flow regime maps using 2,500 experimental data points from 29 experimental studies considering pipe diameters between 0.01 and 0.07 m (0.48 and 2.63 in) in upward flows in pipe and annuli.

To evaluate the different flow regime maps, Wu et al. [16] determined the number of conforming and non-conforming points for each transition boundary for each of the tried flow regime maps. Figure 2.11 shows a step-by-step representation of this method. In order to assess each experimental data point, it will be characterized according to its liquid and gas superficial velocity (Figure 2.11.a). After, a threshold superficial velocity of one of the phases is calculated with the criterion proposed by each of the examined flow regime maps for a given superficial velocity of the other fluid. For example, in Figure 2.11.b a threshold gas superficial velocity, $u_{sg,t}$, is calculated using one of the flow regime models analyzed, considering the same u_{sl} and other conditions as diameter and fluid properties the same as the experimental data point. In this case, the calculated $u_{sg,t}$ is greater than the experimental u_{sg} . This way, the observed flow regime is compared to the flow regime predicted, i.e., Flow Regime (FR) 1 if $u_{sg} < u_{sg,t}$ or FR 2 in the opposite case. This way,

the data point was deemed conforming if the predicted flow regime matches the observed flow regime (Figure 2.11.c) or non-conforming if it differs (Figure 2.11.d).

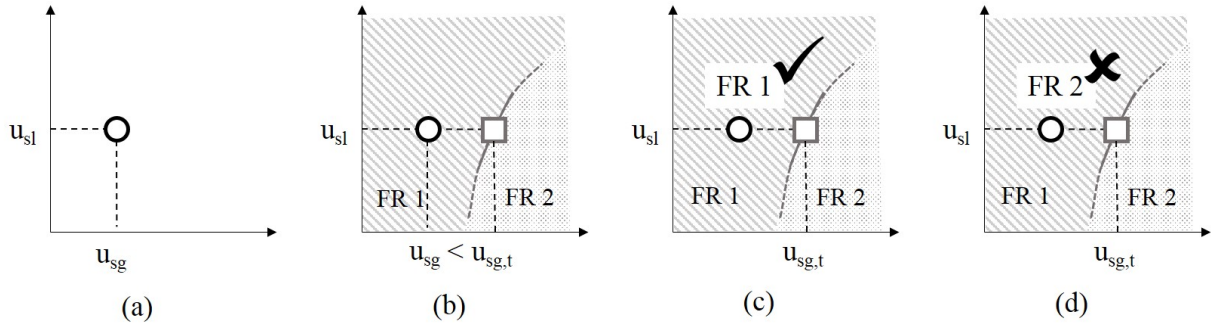


Figure 2.11. Representation of Wu et al. [16] method to evaluate accuracy of flow regime map, where (a) is an experimental data point with observed flow regime, plotted according to its gas and liquid superficial velocities; (b) is a threshold point, calculated using a selected flow regime prediction model, considering the same u_{sl} as the experimental data point, dividing the plot into two different flow regimes; (c) is the case if the observed data point has the same flow regime as predicted by the threshold point, therefore a conforming case; and (d) is the case if the observed flow regime differs to that predicted by the model, thus a non-conforming data point.

The most appropriate transition boundaries proposed by Wu et al. [16] is shown in Figure 2.12. The approach used by Wu et al. [16] will be adopted in this research, adjusting the research for $D_H^* > 40$.

The following sections show a literature review on different flow regime maps and their transition boundaries.

Empirical flow regime maps

Empirical flow regime maps are based on experimental observations. Empirical flow regime maps were popular before the 80's decade, after when more robust mechanistic flow regime maps started to be preferred [18, 19, 42, 43, 20, 44, 45, 46]. Empirical flow regime maps propose a two-dimensional transition boundary empirically located – using dimensional coordinates, such as superficial velocities, or momentum flux, or other dimensionless coordinates – but they lack suitable physical models [18]. Even though the input parameter may be comparable, there is no evidence that the boundaries between flow regimes will still hold the same form for different conditions, such as various fluid types, pressures, and

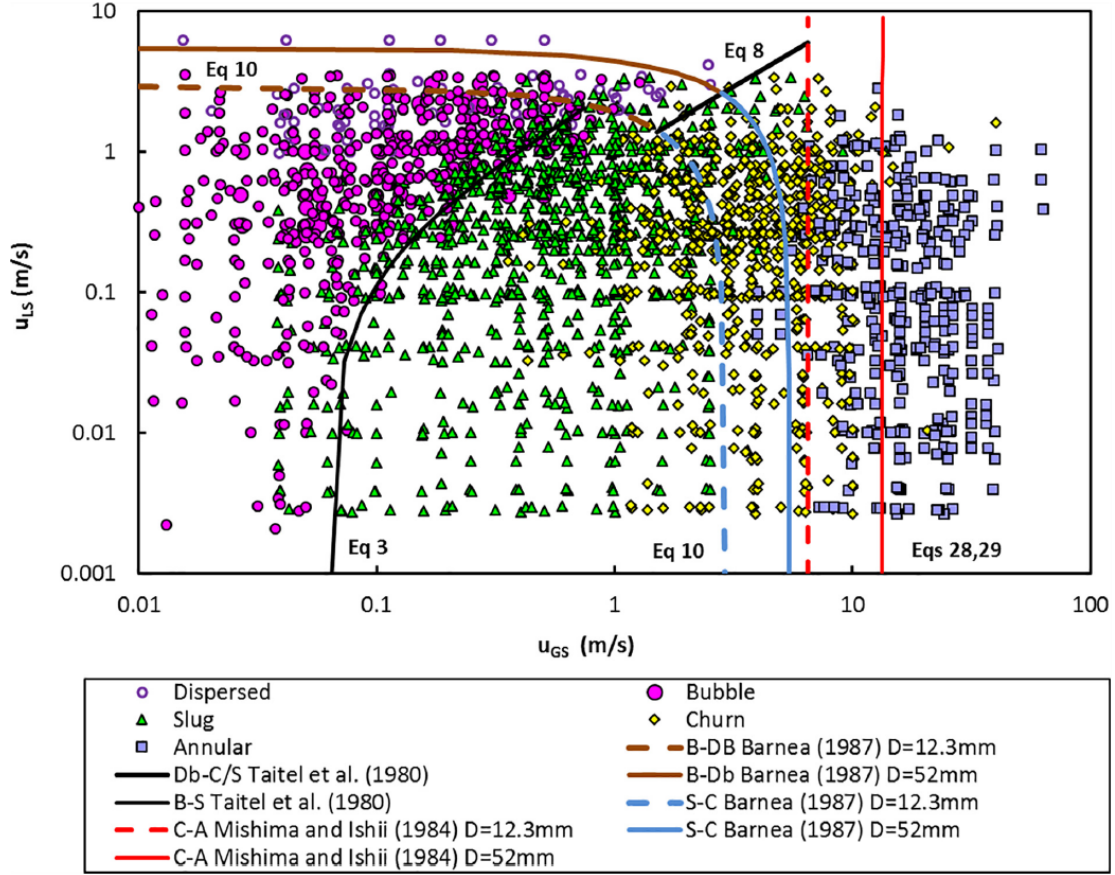


Figure 2.12. Comparative between different flow regime transitions models and experimental observations for pipe diameters between 12.3 and 67 mm [16].

pipe geometries and configurations. For this reason, Taitel et al. [18] considered empirical flow regime maps to be unreliable to be used under conditions different to those their development was based.

Two examples of some of the most popular empirical flow regime maps are those developed by Duns and Ros [11] and Aziz et al. [17]. The flow regime map of Duns and Ros [11] is presented in Section 2.4.

Aziz et al. [17] developed a flow regime map making use of dimensional coordinates –a modified fluid superficial velocity, dependent on fluids specific gravity and specific surface tension. These coordinates are calculated as:

$$Xu_{sg} = \left(\frac{\rho_g}{\rho_a} \right)^{1/3} \left(\frac{\rho_l \sigma_{wa}}{\rho_w \sigma} \right)^{1/4} u_{sg} \quad (2.33)$$

$$Y_{u_{sl}} = \left(\frac{\rho_l \sigma_{wa}}{\rho_w \sigma} \right)^{1/4} u_{sl} \quad (2.34)$$

where the subscripts a and w represent air and water, respectively.

The flow regimes defined by Aziz et al. [17] are a bubble, slug, froth, and annular mist flow. The transition boundaries are calculated as:

- Bubble to slug transition:

$$Y_{u_{sl}} = 0.01(1.96Xu_{sg})^5.81 \quad (2.35)$$

- Slug to froth transition

$$Y_{u_{sl}} = 0.263(Xu_{sg} - 8.61) \quad \text{for } Y_{u_{sl}} \leq 4 \quad (2.36)$$

for $Y_{u_{sl}} > 4$, $Xu_{sg} = 26.5$

- Froth to annular mist transition

$$Y_{u_{sl}} = \frac{1}{100} \left(\frac{Xu_{sg}}{70} \right)^{-6.18} \quad (2.37)$$

The experiments to develop this map were carried out for oil and gas producing wells with diameters of ~ 0.06 m (2.4 in).

Mechanistic flow regime maps

Mechanistic flow regime maps describe transition boundaries based on conservation principles, force balances, and drift-flux approach. The authors of these flow regime maps develop equations that will represent the transition criteria between flow regimes. For example, traditional principles for the transition of bubble flow to slug/cap-bubble flow is the maximum bubble size before its coalescence. Therefore, a geometrical parameter will be

correlated to a given property, in this case, the void fraction, so it is possible to model the transition.

Table 1 shows the main advantages and limitations of relevant mechanistic flow-regime transition models. The next section will briefly describe each of these relevant mechanistic flow-regime transition models.

- **Taitel et al. flow regime map**

Taitel et al. [18] state that no empirical flow regime map produced before their study could be extrapolated to conditions outside of those that they were developed for, due to insufficient physical basis. The authors also point out that these maps differ among them in absolute value and trend for the transition boundaries.

To address this limitation in the literature, Taitel et al. [18] developed a mechanistic flow regime map, defining mechanistic transition boundaries dependent on fluid properties, the velocity of the phases, and pipe geometry. Besides the flow regimes previously identified in this thesis, the authors proposed the so-called dispersed bubble flow, which is characterized by small-diameter spherical gas bubbles dispersed in the liquid phase.

Taitel et al. [18] claim that the transition from bubble to slug flow requires a process of agglomeration or coalescence. Both of these processes can be achieved with increasing gas flow rate, which increases the bubble density and thus shortens the space between bubbles, increasing the coalescence rate. On the other hand, the increase of liquid flow rate increase the turbulent fluctuations, which can break larger diameter bubbles (sustaining smaller bubbles in the flow) and make impossible the recoalescence of the bubbles. Therefore, the transition from bubble flow needs to be separated into two different conditions: where dispersion forces are dominant – i.e., high liquid flow rates – and where they are not.

Under the condition at which the liquid rate is not high enough to not cause this disturbance, the increase of gas flow rate reaches a point at which the bubble density is high enough so that the bubbles are very tightly packed. This proximity results in many collisions and the small bubbles will agglomerate into larger bubbles, which is when the

Table 2.1. Summary of pros and cons of the flow regime maps considered in this study.

Flow regime map	Pros	Cons
Taitel et al. [18]	<ul style="list-style-type: none"> • Widely accepted flow regime map • Introduced a more thorough physical interpretation of the flow regime transitions 	<ul style="list-style-type: none"> • Considers churn flow as an entrance effect • Developed considering diameters only up to 0.05 m; Bases transition criteria on superficial velocities
Mishima and Ishii [19]	<ul style="list-style-type: none"> • Widely accepted flow regime map • Bases transition assumptions on more direct geometrical parameters than superficial velocities (i.e., void-fraction) 	<ul style="list-style-type: none"> • Used experimental results from smaller diameter pipes to verify flow regime transitions
McQuillan and Whalley [43]	<ul style="list-style-type: none"> • Shows improvement in accuracy over Taitel et al. [18] flow regime map 	<ul style="list-style-type: none"> • Very much based on Taitel et al. [18] flow regime map • Had its accuracy tested only against small diameter ($D_H^* < 40$) pipes
Schlegel et al. [32]	<ul style="list-style-type: none"> • Developed for large diameter pipes • Proposes simplifications from Mishima and Ishii [19] assumptions • Includes cap-bubble flow regime 	<ul style="list-style-type: none"> • Very much based on Mishima and Ishii [19] flow regime map

transition to slug flow takes place. The authors define a void fraction (α) of 0.25 for when this will happen and calculate this transition boundary as a function of the fluids superficial velocities, and fluid properties as:

$$u_{sl} = 3.0u_{sg} - 1.15 \left[\frac{g(\rho_l - \rho_g)\sigma}{\rho_l^2} \right]^{1/4} \quad (2.38)$$

where u_{sl} and u_{sg} are the liquid and the superficial gas velocities respectively, g is the gravitational acceleration constant, ρ_l and ρ_g are the liquid and gas densities, and σ is the superficial tension between the gas and the liquid.

Next, Taitel et al. [18] claim that the turbulent forces can break the bubbles – even when the void fraction is higher than 0.25 – when the dispersion forces are dominant. That will only happen if the bubble size can remain small enough to maintain the spherical shape. If this criterion is met, then the bubble flow will become dispersed bubble flow. The equation proposed by the authors for this transition boundary correlates the rate of energy dissipation per unit mass for a turbulent pipe flow and the critical diameter to which the bubble can remain spherical, defined as:

$$u_{sl} + u_{sg} = 4.0 \frac{D^{0.429} \left(\frac{\sigma}{\rho_l}\right)^{0.089}}{(\nu_l^{0.072}) [g(\rho_l - \rho_g)\sigma/\rho_l]^{0.446}} \quad (2.39)$$

where D is the pipe diameter, and ν_l is the kinematic viscosity of the liquid. The authors assert that the maximum allowable packing of the bubbles is a cubic lattice formation, at which the void fraction will be of 0.52. Therefore, once the flow reaches that void fraction, it will transition to another regime, out of dispersed bubble flow. The authors also noticed that for this region, the liquid flow rate is high enough so that the slip velocity between the phases may be neglect, and hence allowing the calculation of the void fraction as only:

$$\alpha = \lambda_g = \frac{u_{sg}}{u_{sg} + u_{sl}} \quad (2.40)$$

Therefore, the transition from dispersed bubble flow can be calculated substituting α for 0.52 in Eq. 2.40.

Taitel et al. [18] assume that churn flow is an entrance flow regime, occurring before slug bubbles can reach a stable state. They propose that before the formation of steady

Taylor bubbles, smaller unstable bubbles are produced. These will collapse and fall down the tube, coalescing with the next smaller bubble rising. Then, a larger bubble that can retain its identity for a longer time will be created. This effect will keep happening until a stable slug can be formed. For this reason, the authors assume that churn flow will be dependent on flow position in the tube, thus depending on the pipe length. The criteria proposed by Taitel et al. [18] for the transition from slug to churn flow is defined as:

$$l_E/D = 40.6 \left(\frac{u_m}{\sqrt{gD}} + 0.22 \right) \quad (2.41)$$

where l_E is the entrance length.

Finally, the authors define the condition for annular flow to exist as the minimum velocity at which the gas velocity is sufficient to lift entrained droplets. Therefore, the transition boundary will be independent of liquid flow rate and pipe diameter. The criteria for the transition to annular flow, as defined by Taitel et al. [18] is based on the Kutateladze number as:

$$\frac{u_{sg} \rho_a g^{0.5}}{[\sigma g (\rho_l - \rho_g)]^{0.25}} = 3.1 \quad (2.42)$$

Taitel et al. [18] found considerable disagreement between the flow regime transition criteria proposed by previous works, but remark the physical base they used to define their transition boundary equations. They also point out the good agreement with experimental data generated for pipe diameters of 25 and 50 mm (~ 1 and ~ 2 in, respectively).

- **Mishima and Ishii flow regime map**

Mishima and Ishii [19] claim that traditional two-phase flow regime criteria based on the fluids superficial velocities might not be suitable for analyses such as rapid transient or entrance flow by the two-phase flow model. Instead, the authors propose the use of more direct geometrical parameters, such as void fraction, as a more reliable method to define the flow regime transition boundaries. The authors state that this method is more versatile,

once void fraction can also be correlated to superficial velocities when under steady-state fully developed conditions.

Mishima and Ishii [19] define a void fraction of 0.3 as the criteria for the transition from bubble flow to slug flow. This number comes from the hypothesis that the bubbles are positioned in a tetrahedral lattice pattern and that when the maximum possible gap between the bubbles becomes less than a bubble diameter, the number of collisions and coalescence will be very high. Therefore, considering the geometrical positioning of the gas bubbles, it is verified that this void fraction will be of $(2/3)^2 = 0.296 \approx 0.3$. Then, to convert that void fraction into a conventional form based on superficial velocity, a relationship between u_{sg} and u_{sl} may be derived from the drift-flux velocity for bubble flow in round tubes as [47]:

$$u_{sl} = \left(\frac{3.33}{C_0} - 1 \right) u_{sg} - \frac{0.76}{C_0} \left(\frac{\sigma g \Delta \rho}{\rho_l^2} \right)^{0.25} \quad (2.43)$$

where $\Delta \rho = \rho_l - \rho_g$ and C_0 can be calculated for flows in a round tube as [47]:

$$C_0 = 1.2 - 0.2 \sqrt{\rho_g / \rho_l} \quad (2.44)$$

Mishima and Ishii [19] assume the wake effect as the cause for the transition from slug to churn flow. This effect is described as the increased proximity that happens due to the mean void fraction over the entire section exceeding that over the slug-bubble region. This proximity will collapse the Taylor bubbles, transitioning the slug flow to a churned flow. The authors define the transition criterion as:

$$\alpha \geq 1 - 0.813 \left[\frac{((C_0 - 1)u_m + 0.35 \sqrt{\frac{\Delta \rho g D}{\rho_l}})}{u_m + 0.75 \sqrt{\frac{\Delta \rho g D}{\rho_l}} \left(\frac{\Delta \rho g D^3}{\rho_l \nu_l^2} \right)^{1/18}} \right]^{0.75} \quad (2.45)$$

The void fraction can be calculated as:

$$\alpha = \frac{u_{sg}}{C_0 u_m + 0.35 \left(\frac{\Delta \rho g D}{\rho_l} \right)} \quad (2.46)$$

For the transitions from churn to annular flow, the authors defined two mechanisms that could lead the flow to change from churn to annular, namely (i) flow reversal in the liquid film around large bubbles, and (ii) destruction of the liquid slug or large wave that can be sustained as small droplets in a gas core. As for large diameter pipes that fit the inequality

$$D > \frac{\sqrt{\sigma/(g\Delta\rho)}N_{\mu l}^{-0.4}}{[(1 - 0.11 * C_0)/C_0]^2} \quad (2.47)$$

where $N_{\mu l}$ is a dimensionless viscous number, defined as

$$N_{\mu l} = \frac{\mu_l}{\left(\rho_l \sigma \sqrt{\frac{\sigma}{g\Delta\rho}}\right)^{1/2}} \quad (2.48)$$

For water and air at standard conditions, this diameter is of 0.06 m (2-3/8 in). Therefore, for all the pipes considered in this work, the transition to annular flow can be modelled according to Mishima and Ishii [19] as:

$$u_{sg} > N_{\mu l}^{-0.2} \frac{\sigma_g \Delta\rho}{\rho_g}^{1/4} \quad (2.49)$$

The authors compared their flow regime map with other empirical maps and claimed that despite apparent differences in trend and values, considering the subjectivity of visual characterization of flow regimes and transition zones instead of evident transition curves, the agreement is good. They also compared their flow regime map with the one developed by Taitel et al. [18] and found good agreement.

- **McQuillan and Whalley flow regime map**

McQuillan and Whalley [43] developed a hybrid flow regime map, making use of mechanistic and semi-empirical equations defined by other authors, and developed a new equation to explain the transition from slug to churn flow. The authors assumed Taitel et al. [18] equation for the transition from bubble to slug flow.

For the boundary between non-dispersed to dispersed bubble flow, they adopted the correlation defined by Weisman et al. [48], calculated as:

$$u_{sl} \geq \frac{6.8}{\rho_l^{0.444}} (gD\Delta\rho)^{0.278} \left(\frac{D}{\mu_l}\right)^{0.112} \quad (2.50)$$

This correlation was empirically adapted (for a broader range of diameters) from Taitel and Dukler [49] relationship for horizontal tubes. To apply it for vertical tube flows, they assumed that the liquid velocities under consideration were high enough so that the effect of slip between the two phases are negligible and that the turbulence is caused by the bulk flow alone, without the influence of the tube inclination. The correlation developed by Weisman et al. [48] differs from the one produced by Taitel et al. [18] by having a smaller tube diameter effect than the latter.

For the transition from dispersed bubble to churn or annular flow, the authors consider that this flow regime limit is set when the bubbles are in a close-packed lattice formation – opposed to the cubic lattice formation assumed by Taitel et al. [18]. In this formation, the void fraction is $\alpha = 0.74$. It is important to notice that at the flow velocity considered for dispersed bubble flow, there is no slip between the phases. Therefore, the void fraction can be calculated by Eq. 2.40. The following equation gives the transition boundary:

$$u_{sg} = 0.74(u_{sg} + u_{sl}) \quad (2.51)$$

and will begin at the end of the transition curve from bubble to slug flow.

McQuillan and Whalley [43] claimed that the requirement of knowledge of the length of the tube to calculate the transition from slug to churn flow proposed by Taitel et al. [18] are rare to be given in experimental reports. They also questioned the assumption by Mishima and Ishii [19] that the length of the gas plug is the distance between the top of the Taylor bubble and the point at which the film thickness is equal to the Nusselt film thickness. The authors also point out the Mishima and Ishii [19] used Bernoulli's equation

for their modeling, even though the flow is unsteady, which could lead to errors. Thus, McQuillan and Whalley [43] propose a new method to predict the transition boundary from slug to churn flow: the flooding of the falling liquid film surrounding the Taylor bubble. To calculate the transition boundary, they propose the use of a semi-empirical equation to predict the flooding gas and liquid flowrates developed by Wallis [41], substituting the superficial gas and liquid velocities in the equation by the plug and liquid film velocities, which yields:

$$u_{sg}^* + u_{sl}^* = C \quad (2.52)$$

where C is a constant and u_P^* and u_f^* are the dimensionless plug and liquid film velocities, defined as:

$$u_{sg}^* = u_P \rho_g^{1/2} [gD(\rho_l - \rho_g)]^{-1/2} \quad (2.53)$$

$$u_{sl}^* = u_f \rho_l^{1/2} [gD(\rho_l - \rho_g)]^{-1/2} \quad (2.54)$$

The superficial plug flow (u_P) and superficial liquid film velocities (u_f) can be calculated by iteratively solving the equations

$$u_P = \left(1 - \frac{4\delta}{D}\right) \left[1.2u_m + 0.35 \left(\frac{gD\Delta\rho}{\rho_l}\right)^{1/2}\right] \quad (2.55)$$

$$\delta = \left(\frac{3D\mu_l u_f}{4g\rho_l}\right)^{1/3} \quad (2.56)$$

$$Q_P = Q_f + (Q_g + Q_l) \iff u_P = u_f + u_m \quad (2.57)$$

Lastly, the boundary to the transition to annular flow is correlated to a modified Froude

number as

$$u_{sg} \sqrt{\frac{\rho_g}{gD(\rho_l - \rho_g)}} \geq 1 \quad (2.58)$$

The authors use Hewitt and Wallis [50] and Bennett et al. [51] work to corroborate that when this modified Froude number is bigger than 1, the inertia forces of the flow will overcome the gravitational effects, and so the flow will become annular.

The flow regime map developed by the authors present a good agreement with experimental observations – 70.1 % of the 1399 evaluated points were in agreement with the experimentally observed flow regimes, and 84.1 % were in accordance with the intermittent vs. continuous nature of the flow. Thus they conclude that their flow regime map is a more robust option when compared to empirical flow regime maps. The authors also suggest farther studies in flow pattern observations in tubes larger than 0.05 m.

- **Schlegel et al. flow regime map for large diameter pipes**

Schlegel et al. [32] developed a flow regime map for large diameter pipes based on Mishima and Ishii [19] transition criteria, calculating the boundaries by the use of drift-flux models developed for large diameter pipes [25, 14]. The one-dimensional drift-flux model, making use of dimensionless numbers is calculated as:

$$\frac{u_{sg}}{\alpha} = \langle\langle u_g^+ \rangle\rangle = C_0 u_m^+ + V_{gj}^+ \quad (2.59)$$

where $\langle\langle \rangle\rangle$ represent the void-fraction weighted mean quantity; V_{gj}^+ is the dimensionless void-fraction-weighted mean drift velocity, defined according to flow conditions; and u_g^+ and u_m^+ are the gas and mixture velocity non-dimensionalized by a factor of $(\sigma g \Delta \rho / \rho_l^2)^{1/4}$, i.e.

$$u_g^+ = \frac{u_g}{(\sigma g \Delta \rho / \rho_l^2)^{1/4}} \quad (2.60)$$

$$u_m^+ = \frac{u_m}{(\sigma g \Delta \rho / \rho_l^2)^{1/4}} \quad (2.61)$$

Schlegel et al. [32] assumed that Mishima and Ishii [19] criteria for the bubble-to-slug transition is applicable as the transition from bubble to cap bubble flow in large diameter pipe. Thus, the change will happen once the maximum packing void fraction happens ($\alpha = 0.3$). Based on experimental observations, the author claims that the shift to cap-bubble flow starts when the void fraction is equal to 0.2 and ends when $\alpha = 0.3$. Thus, they assume the beginning of the change at $\alpha = 0.2$ (the flow is still in an entirely bubbly flow regime) and the end at $\alpha = 0.3$ (completely cap-bubbly flow). They use Hibiki and Ishii [14] drift-flux model to calculate the transition boundary for bubbly flow and the Kataoka and Ishii [25] drift-flux model to estimate the boundary when the flow is cap-bubbly. The boundary transition can be calculated as:

$$u_{sg}^+ = 0.3(C_0 u_m^+ + V_{gj}^+) \quad (2.62)$$

where u_{sg}^+ is the superficial gas velocity non-dimensionalized by a factor of $(\sigma g \Delta \rho / \rho_l^2)^{1/4}$ (analogously to Eqs. 2.60 and 2.61), and C_0 can be calculate as [14]:

$$C_0 = \exp \left[0.475 * \left(\frac{u_{sg}^+}{u_m^+} \right)^{1.69} \right] \left(1 - \sqrt{\frac{\rho_g}{\rho_l}} \right) + \sqrt{\frac{u_{sg}^+}{u_m^+}}, \text{ for } 0 \leq \frac{u_{sg}^+}{u_m^+} \leq 0.9 \quad (2.63)$$

and if > 0.9 , C_0 can be calculated by Eq. 2.44. V_{gj}^+ can be calculated by [25]:

$$\left\{ \begin{array}{l} \text{Low viscous case: } N_{\mu l} \leq 2.25 \times 10^{-3} \\ V_{gj}^+ = 0.0019 D_H^{*0.809} \left(\frac{\rho_g}{\rho_l} \right)^{-0.157} N_{\mu l}^{-0.562}, \text{ for } D_H^* \leq 30 \\ V_{gj}^+ = 0.030 \left(\frac{\rho_g}{\rho_l} \right)^{-0.157} N_{\mu l}^{-0.562}, \text{ for } D_H^* > 30 \\ \text{High viscous case: } N_{\mu l} > 2.25 \times 10^{-3} \\ V_{gj}^+ = 0.92 \left(\frac{\rho_g}{\rho_l} \right)^{-0.157}, \text{ for } D_H^* > 30 \end{array} \right. \quad (2.64)$$

where $N_{\mu l}$ can be calculated with Eq. 2.48 and V_{gj}^+ is the dimensionless drift velocity, given by:

$$V_{gj}^+ = \frac{\langle\langle V_{gj} \rangle\rangle}{\left(\frac{\sigma g \Delta \rho}{\rho_l^2}\right)^{1/4}} \quad (2.65)$$

The transition from cap-bubbly to turbulent-churn is described by Schlegel et al. [32] similarly to the transition from slug to churn-flow by Mishima and Ishii [19], i.e., the shift occurring when the void fraction on the liquid phase is equal to the void fraction in the cap bubbles. That void fraction is 0.51, which is considered the criteria for the transition from cap-bubbly to turbulent flow. In this case, Kataoka and Ishii [25] model can be used to calculate the transition boundary in the u_{sg} x u_{sl} coordinate, i.e., Eqs. 2.59 and 2.64.

Finally, the transition to annular flow is modeled assuming the entrainment of the liquid into the gas flow, as reported by Mishima and Ishii [19].

The authors report good agreement with experimental data produced by them in a pipe with a diameter of 0.15 m, for air and water superficial velocities ranging from 0.1 to 5.1 m/s and 0.01 to 2.0 m/s, respectively. They also reported good agreement with experimental data from the experiments in a 0.2 m diameter pipe carried out by Ohnuki and Akimoto [23] and the flow regime transition boundaries reported by Smith [52]. The authors recommend that additional experiments should be carried out to investigate more thoroughly flow regimes in large diameter pipes, especially for conditions of liquid velocity higher than 1 m/s. It is also important to notice that for large diameter pipes ($D_H^* \geq 30$), Schlegel et al. [32] flow regime map is independent of the diameter size.

2.6 Critical flow transition

Single-phase critical flow is defined as the condition when the downstream flow rate is independent of the upstream conditions. It happens when molecular relaxation phenomena are sufficiently rapid for the gas to be considered under thermodynamic equilibrium. This equilibrium is usually achieved when Mach number is equal to 1 at the most constricted

cross-section (i.e., when the flow reaches sonic velocity). In two-phase critical-flow, however, the analysis becomes more complex, with the critical flow being dependent on the whole “critical region” of rapid property change. Some mathematical methods were defined to predict conditions for criticality at one location, but in two-phase flows, this analysis cannot be constrained to one specific location [53].

Most critical flow models were developed for small orifices [54, 55, 56, 57, 58] more focused on valves and orifices plates. Nevertheless, Beck et al. [59] tested for pipes with diameters ranging from 0.02 to 0.05 m (0.92 and 1.94 in) the correlations by Wallis [41] and Fortunati [60]. Their results presented a good agreement for engineering purposes for the flows in these pipe diameters. Later, Beck et al. [61] tested Wallis [41] correlation for a 0.12 m (4.9 in) diameter pipe. The larger diameter introduced high errors to the calculation. Beck et al. [61] proposed an empirical modification of the Wallis [41] model to fit their data, reaching an acceptable error for engineering calculations.

Beck et al. [59] noticed that both Wallis [41] and Fortunati [60] equations predict a minimum critical velocity for flows with void fraction around to 0.5 and give approximately the same critical flow velocity. Therefore, due to ease of use and to having available a comparison against experimental data for a 0.12 m diameter pipe, only the model by Wallis [41] will be considered from now on.

Wallis [41] model is a Homogeneous Equilibrium Model (HEM) for critical two-phase flow prediction. It approaches the critical flow problem by assuming the two-phase mixture as a pseudo-fluid, described by the same equations as a single-phase flow. Therefore, this approach is based on the ideal case of complete interphase equilibrium, neglecting effects such as nucleation, interphase heat exchange, mass and momentum transfer, and multi-dimensional effects and developing two-phase flow patterns [53]. This type of approach is adequate for long pipes, with sufficient length to achieve equilibrium and flow patterns favorable for interphase forces repressing relative motion. Therefore, it is deemed adequate for the application on black-oil wells. The critical two-phase flow velocity described by

Wallis [41] correlates the no-slip liquid holdup of the phases and their respective sonic velocities as:

$$u_{m,c} = \left[(\lambda_g \rho_g + \lambda_l \rho_l) \left(\frac{\lambda_g}{\rho_g u_{g,c}^2} + \frac{\lambda_l}{\rho_l u_{l,c}^2} \right) \right]^{-0.5} \quad (2.66)$$

where λ_g and λ_l are the no-slip liquid and gas holdups (see Eq. 2.40) and $u_{l,c}$, and $u_{g,c}$ are the critical velocity in the liquid and gas phases, respectively:

$$u_{l,c} = \sqrt{\frac{1}{\rho_l C_l}} \quad (2.67)$$

$$u_{l,g} = \sqrt{kZRT} = 16.94 \sqrt{\frac{kZT}{\gamma_g}} \quad (2.68)$$

where C_l is the liquid compressibility, k is the adiabatic compression/expansion factor (ratio of specific heats ($k = c_p/c_v$)), and R is the individual gas constant.

Beck et al. [61] reported that Wallis [41] model tends to under-predict the critical conditions. To fix this issue, they proposed an empirical modification to the calculation of the critical flow rate by the addition of a multiplicative factor of $3.017D^{0.29}$. The authors reported that the addition of this parameter improved the model accuracy when predicting the critical flow rate in the 0.12 m diameter pipe, while not affecting the prediction in the 0.05 and 0.02 m diameter pipes. Figure 2.13 shows the experimental data by Beck et al. [61] for the 0.12 m pipe and the critical flow criteria curves by Wallis [41] and its modification proposed by Beck et al. [61], calculated for the experimental conditions. The dotted region is everything that is considered to be in critical condition according to Wallis [41] criteria; the hachured area is considered to be in critical condition according to the modified criteria with the diameter dependent multiplier.

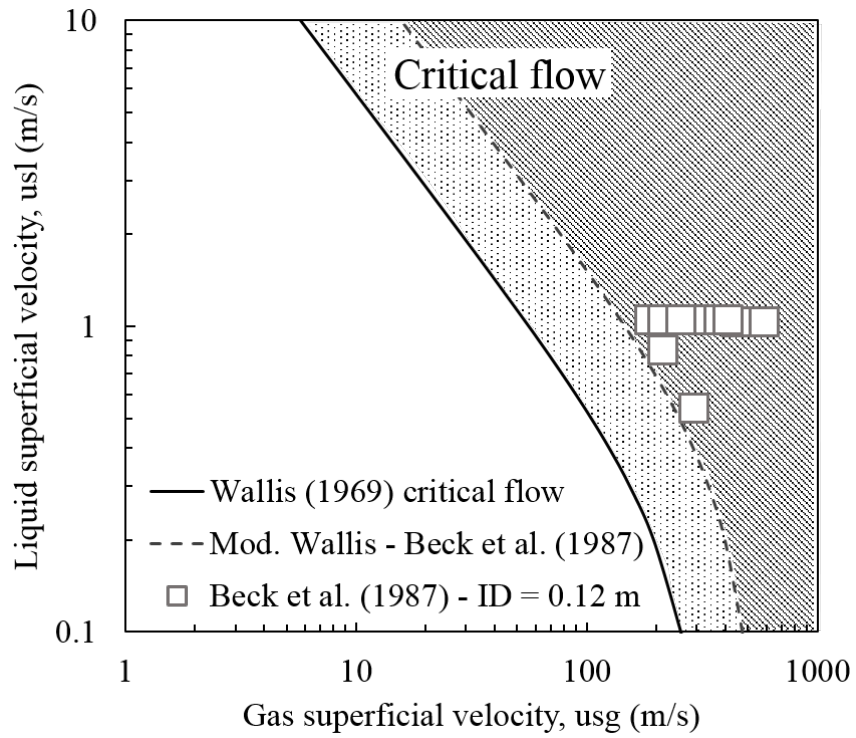


Figure 2.13. Experimental results reported by Beck et al. [61] for experimental two-phase flow in a pipe with a 0.12 m diameter and Wallis [41] calculated for their experimental conditions.

Chapter 3

Experimental Data

To evaluate flow regime maps, relevant data on the conditions of interest is necessary. In the case of this work, data covering large diameters and a wide range of flow velocities will be used. Flow data from both field and lab were collected from the literature. Experimental data was also collected at LSU, covering a gap left in the literature involving larger diameter pipes (up to 0.30 m) and high flow velocities.

3.1 Experimental data from literature

Eight studies on two-phase flow in large diameter vertical pipes that provide flow regime characterization are summarized in Table 3.1. This table presents information about the working fluids, pipe diameters, superficial liquid and gas velocities, and relevant measured parameters (pressure gradient, liquid holdup, and flow regime) of each respective study. This table is used as the starting point for the comprehensive literature review to gather data and empirical observations on vertical two-phase flows in large diameter pipes for a wide range of gas-liquid velocities. Most flow regime maps were evaluated with experimental data with water and air. The exception is Oddie et al. [62] data, who used nitrogen and water as working fluids. In this case, to simplify the analysis, the properties of air were considered instead of the properties of Nitrogen, as air is composed of more than 70% of Nitrogen and the experimental conditions do not include high pressures or temperatures. The ideal gas law is also considered, and the specific gravity of nitrogen and air are approximately the same.

Most of the flow regime characterizations in Table 3.1 were obtained based on visual observations. The exception is the research carried out by Smith et al. [22]. They made use of a neural network classification system, coupled with an electrical impedance void-meter. Ali [7] also characterized the flow regimes visually but assisted their definition with the use of the statistical analysis of void fraction data calculated with the use of the pressure drop method. All of the authors unanimously claim the absence of slug flow in its classical

Table 3.1. Literature review on flow regime characterization of vertical upward two-phase flows in large diameter pipes.

Researcher	Fluid system	ID (m)	u_{sg} (m/s) min-max	u_{sl} (m/s) min-max	$\frac{dp}{dz}$	α	FR
Ohnuki and Akimoto [63]	Air-water	0.48	0.02-0.87	0.01-0.20	✓	✓	✓
Ohnuki and Akimoto [23]	Air-water	0.20	0.03-4.68	0.06-1.06	✓	✓	✓
Oddie et al. [62]	N2-water [†]	0.15	0.05-0.98	0.03-1.57	✗	✓	✓
Ali [7] and Ali and Yeung [‡] [24]	Air-water	0.25	0.06-2.26	0.19-1.10	✓	✓	✓
Smith et al. [22]	Air-water	0.10	0.02-20.1	0.02-2.02	✗	✓	✓
Zabaras et al. [8]	Air-water	0.15	0.01-10.0	0.02-1.01	✗	✓	✓
Zabaras et al. [8]	Air-water	0.28	0.10-15.8	0.03-0.16	✓	✗	✓
Shen et al. [64]	Air-water	0.20	0.03-0.35	0.05-0.31	✓	✗	✓

[†] As air is composed of more than 70% of Nitrogen, the calculations for the fluid properties in this work were done considering air instead of pure Nitrogen.

[‡] Ali and Yeung [24] work present a continuation of the analysis from Ali [7] Ph.D. dissertation. Therefore the experimental data is the same for both works.

definition (as defined in Section 1.2).

In total, 695 data points with identified flow regime were collected. Gathering all experimental data points in a plot of gas superficial velocity versus liquid superficial velocity will result in Figure 3.1. Different authors characterize flow regimes by different names. In the present case, there are 17 different flow regime names, and even coincident names describing flow regimes with different features. Therefore, in order to create a flow regime map based on experimental data, it is mandatory to standardize all these flow regimes into a more limited group. Based on the description of the flow regimes by the authors, the data-points were re-categorized into the four main flow regimes considered in this work: bubble, cap-bubble, churn, and annular flow. Each of these flow regimes is identified by the dashed boxes around the legend. The blue box identifies bubble flow, yellow for cap-bubble, green for churn, and red for annular flow.

The superficial velocities for liquid and gas presented in Table 3.1 are plotted in a bar chart on Figure 3.2 for easier visualization. As shown in the figure, there is a lack of experimental data in the literature for pipe diameters larger than 0.10 m (~ 4 in), including superficial velocities of gas higher than 5 m/s (~ 15 ft/s), and superficial liquid velocities

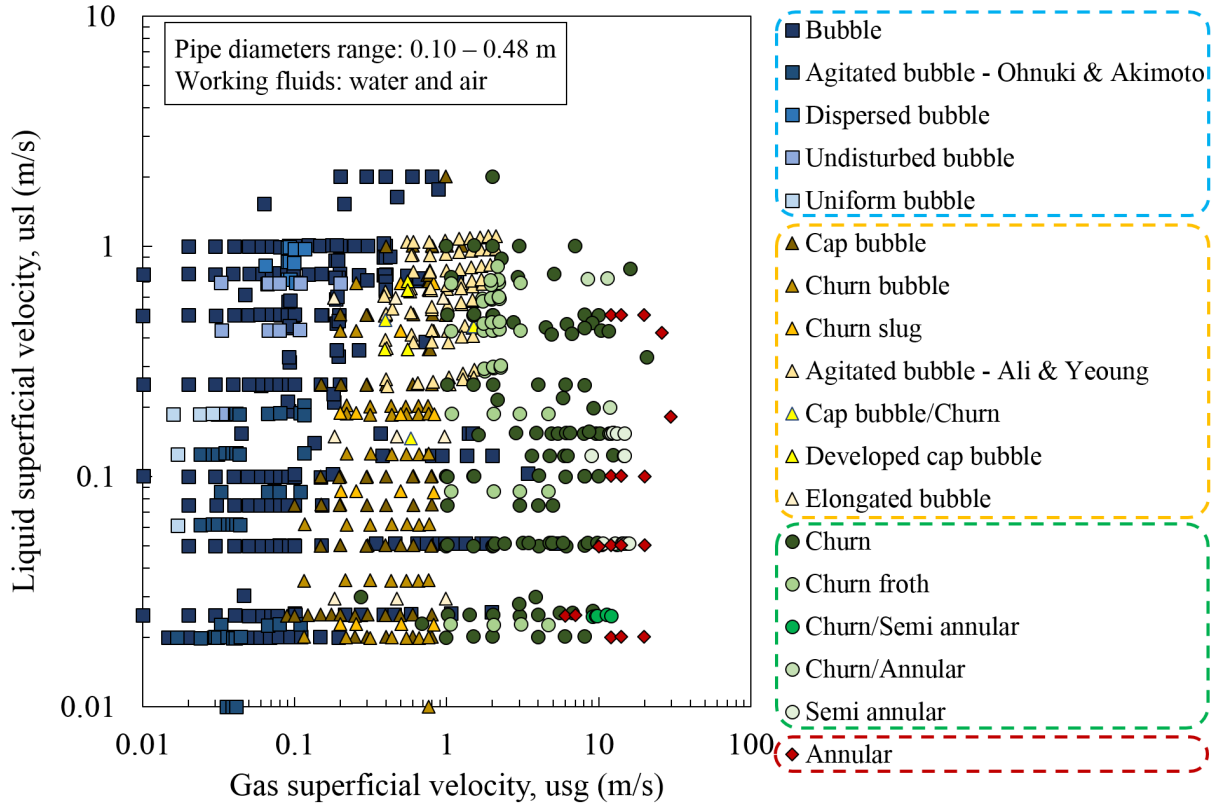


Figure 3.1. Different flow regimes for vertical upward two-phase flows in large diameter pipes of the experimental data considered in this study.

higher than 0.2 m/s (~ 0.6 ft/s). It should also be noticed that for diameters larger than 200 mm (~ 8 in), Zabararas et al. [8] reaches relatively high gas superficial velocities (16 m/s, or ~ 52.5 ft/s), but low liquid superficial velocities (0.15 m/s or ~ 0.5 ft/s). On the other hand, Ali [7] and Ohnuki and Akimoto [23] reach higher liquid flow rates of about 1.1 m/s (~ 3.61 ft/s), but only 2.6 and 3.1 m/s (~ 8.5 and ~ 10.2 ft/s) for superficial gas velocities, respectively.

The flow regime maps are also validated using field data. Flow regimes cannot be visually observed (as the flow occurs underground in the wellbore), but the flow regimes are indirectly correlated to the pressure gradient calculated using a flow model based on flow regimes. Field data reported by Asheim [65] used in this work is presented in Table 3.2. The work of Asheim [65] reported data of 37 wells from the Forties field. The oil rate ranged from 1,040 up to 4,356 m³/day (6540 – 27270 stb/day), and the gas rate ranged from 20,898

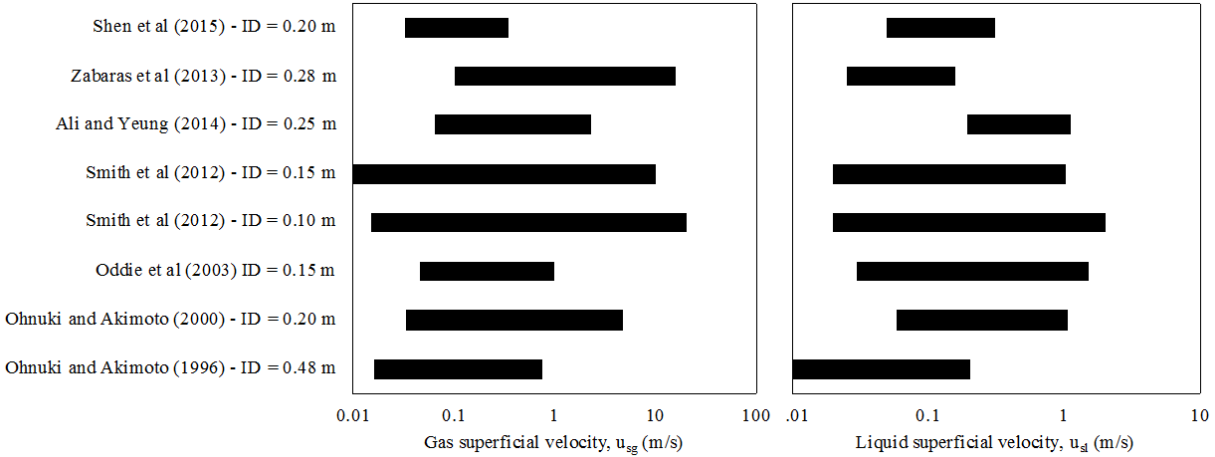


Figure 3.2. Literature review on works with characterized flow regimes for vertical upward two-phase flows in large diameter pipes.

to 260,061 m³/day (9,184 to 738 Mscf/day).

Table 3.2. Field data that provide information of pressure gradient.

Researcher	Fluid system	ID (m)	Q_g (m ³ /s) min-max	Q_l (m ³ /s) min-max	$\frac{dp}{dz}$	α	FR
Asheim [65]	Natural gas-oil	0.10-0.16	20,898-260,061	1,040-4,356	✓	✗	✗

3.2 LSU experiments from Waltrich et al. [9]

Experiments were carried out at Louisiana State University’s PERTT Lab to cover the gap from the literature, including large-diameter pipes and high liquid and gas superficial velocities. A flow-loop was explicitly designed to generate data for diameter up to 297 mm (11.7 in), liquid velocities up to 4.35 m/s (14 ft/s), and gas velocities up to 30 m/s (98 ft/s). The data collected from these experiments are reported on the work of Waltrich et al. [9]. The experimental rig constructed is shown in Figure 3.3, where a schematic of the experimental setup and actual pictures of the installation are presented. More details about the experimental setup and procedure can be found in Waltrich et al. [9].

Experimental data

A summary of the complete experimental dataset generated at LSU is presented in the Appendix, in Table A.1. Information is given on superficial liquid and gas velocities,

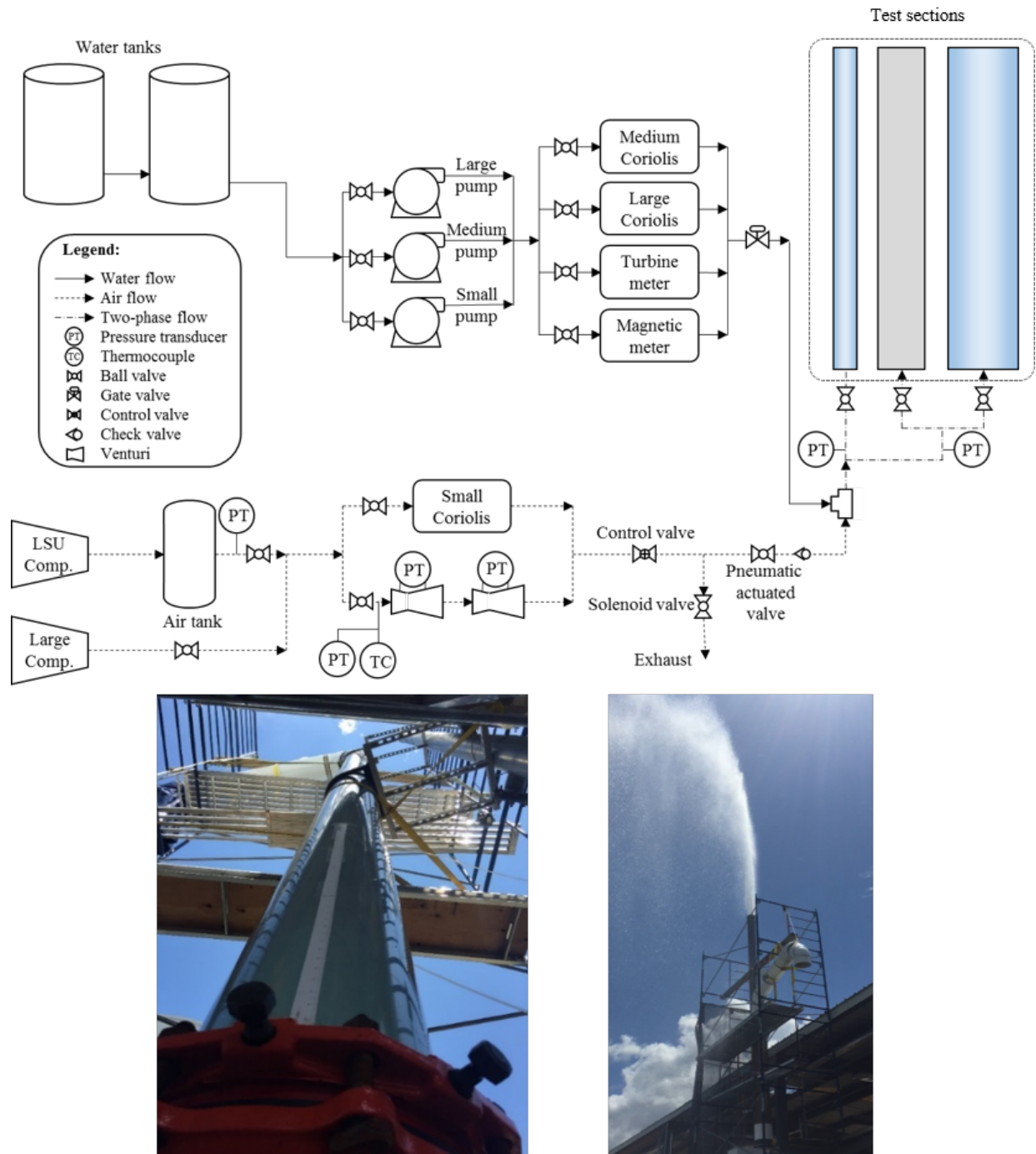


Figure 3.3. Schematic diagram of the experimental apparatus and pictures of the test sections (0.30 m – 11.7 in – ID on the left, and 0.20 m – 7.80 in – ID on the right) [9].

pressure gradient, visually observed flow regime, and liquid holdup. Nevertheless, most of the test runs carried out at LSU do not have flow regime observations available, due to the difficulty of visualizing the flow regimes for large diameters at high velocities. For large

diameters, the flow features (such as bubbles, liquid and gas movement) is only noticeable near the pipe wall. Because of the high velocities and highly turbulent flow, a large amount of small bubbles is also created, adding even more complexity to flow regime observation, even using high-speed cameras. Therefore, for the scope of this work, it is decided that the test runs that have observed flow regimes are used in the development of the flow regime map. Furthermore, the rest of the data will be used for the validation of this flow regime map, comparing the experimental pressure gradient to the simulated pressure gradient using the proposed flow regime map. The test runs that include the experimentally observed flow regime are shown in Figure 3.4.

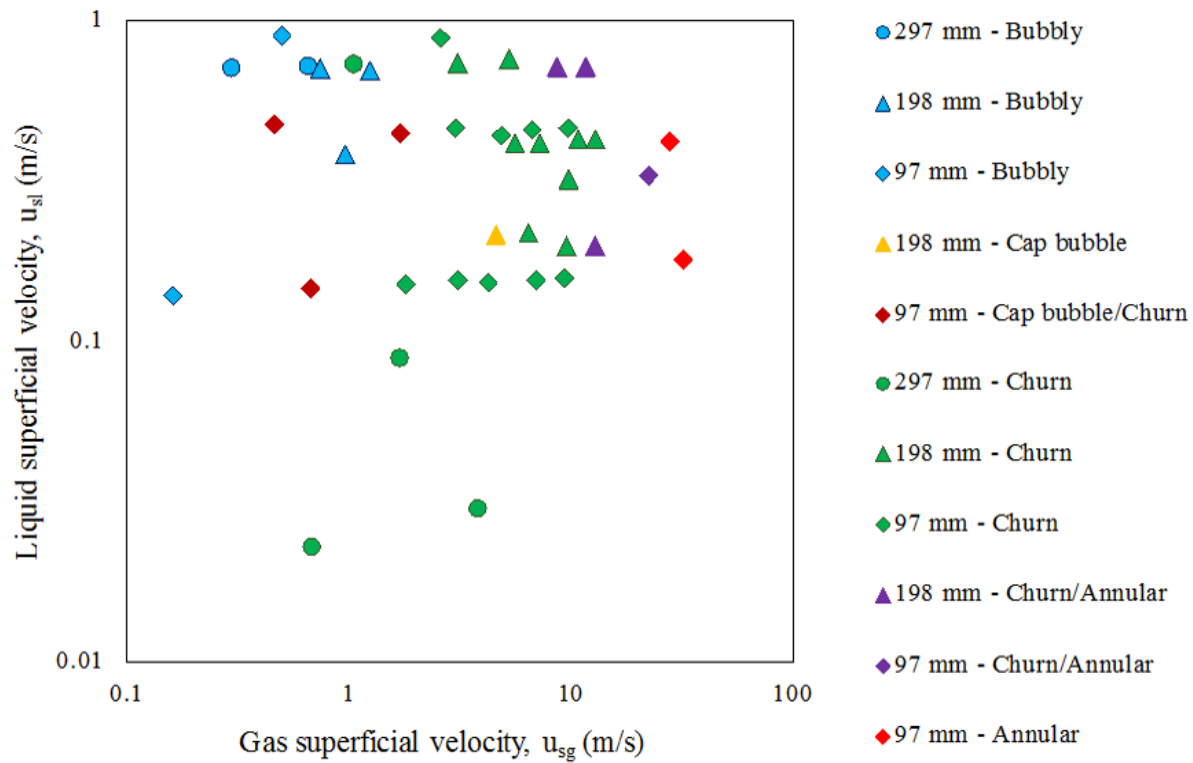


Figure 3.4. LSU data points with the final visual observation of flow regimes.

Figure 3.5 shows a similar bar plot as seen in Figure 3.2, completed with the experimental data produced at LSU. The black blocks represent the data that have observed flow regimes and will be used in the development of the flow regime map. The white blocks represent the range of experimental points that will be used in the evaluation of the flow regime maps.

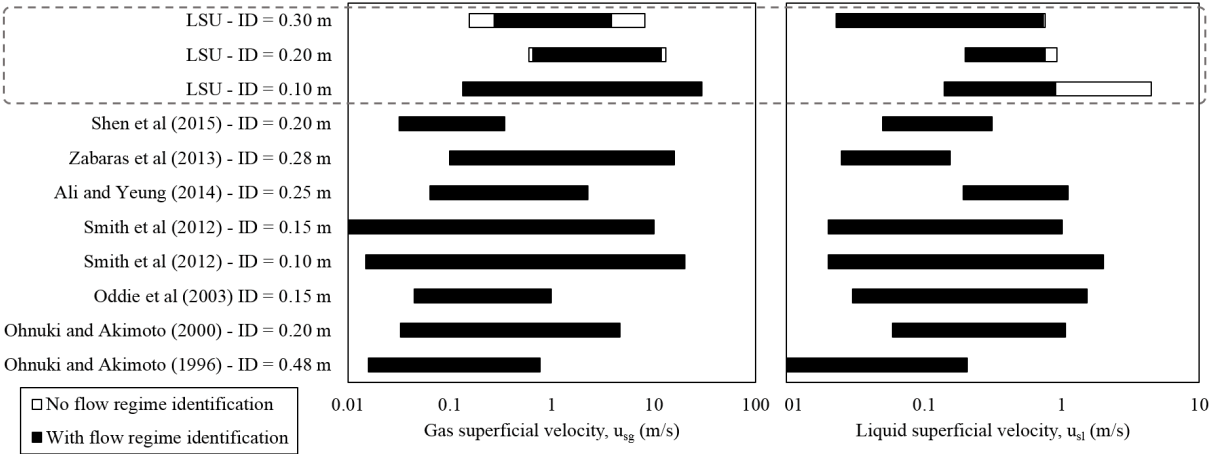


Figure 3.5. Superficial fluid velocity ranges for the data considered in this work, including data produced at LSU. The black blocks represent data that had a direct flow regime observation, while the white blocks represent the data that did not had direct flow regime observation, but will be used for the flow regime map validation.

Chapter 4

Results and Discussions

4.1 Evaluation of current flow regime maps

A critical remark from the observed flow regimes is the absence of slug flow noted in all the experimental works on pipes with $D_H^* > 40$ considered in this work. Thus, considering this absence and that most of the flow regime maps evaluated in this work predict slug flow, this flow regime is replaced by cap-bubble flow in these analysis.

The flow regimes are re-categorized into only four flow regimes to evaluate the flow regime maps, based on the description provided in each work. The selected flow regimes are bubble, cap-bubble, churn, and annular. The characteristics of each of these flow regimes are as described in Chapter 1.

The observed flow regimes data points were tested based on its flow and fluid properties against four different flow regime maps: Duns and Ros [11] and Aziz et al. [17] empirical flow regime maps, and Mishima and Ishii [19] and Schlegel et al. [32] mechanistic flow regime maps. Figure 4.1 shows all the 695 experimental observations of flow regimes already re-categorized into the four flow regimes. The legends of the transition boundaries are included by the name of the author who described them, followed by the transition which it represents. The transitions are abbreviated as:

- B-S: Bubble to Slug flow
- S-C: Slug to Churn flow
- C-A: Churn to Annular flow
- B-CB: Bubble to Cap bubble flow
- CB-C: Cap bubble to Churn flow
- -A: Transition to Annular flow
- I-II: Transition from Region I to Region II, by Duns and Ros [11]

- II-T: Transition from Region II to Transition Zone, by Duns and Ros [11]
- T-III: Transition from Transition Zone to Region III, by Duns and Ros [11]

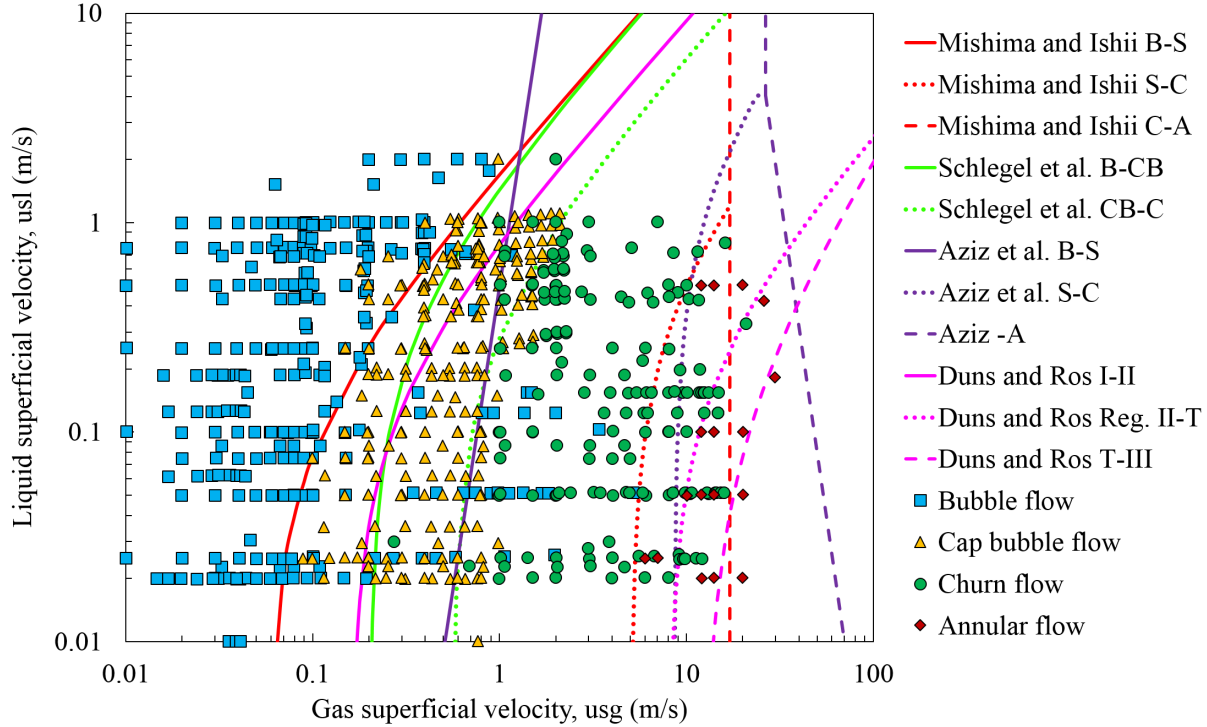


Figure 4.1. Flow regimes of 695 experimental data points plotted against transition curves of flow regime maps by Duns and Ros [11], Aziz et al. [17], Mishima and Ishii [19], and Schlegel et al. [32].

The flow regime map by Taitel et al. [49] was left out of this analysis due to a few reasons. First, the criteria used by Taitel et al. [49] for the transition from bubble to slug flow is similar to the criteria adopted by Mishima and Ishii [19]. However, the criteria by Mishima and Ishii [19] has a stronger physical explanation, basing the $\alpha = 0.30$ as a limit based on geometrical distribution. The second reason is due to the slug to churn transition boundary, which assumes churn flow as an entrance effect, the fact that has been already debated and rejected on the literature [66, 67]. Next, Taitel [18] propose the dispersed bubble flow regime, which is not considered in this analysis because only Ali and Yeung (2014) claim to have observed this flow regime, and reported by Taitel et al. [18] flow regime map as inaccurate on its prediction.

McQuillan and Whalley [43] flow regime map were also not included in this analysis. The authors base their flow regime map on Taitel et al. [18], adopting the same transition criteria for bubble to slug, and churn to annular. The novelty they bring to Taitel et al. [18] approach is the suggestion to calculate the transition from bubble to dispersed bubble flow, which will not be considered in this work, and propose a new method to calculate the transition from slug to churn flow. This criterion is based on the flooding of the liquid film around the Taylor bubble during the slug flow. However, as noted before, no slug flow was observed in the studies considered in this work, and slug flow is not expected for $D_H^* > 40$.

Wu et al. [16] evaluate the flow regimes boundaries by the amount of conforming and non-conforming points to each transition boundary. The authors consider pairs of flow regimes at a time and assess if the observed data point will match the predicted flow regime or not (stay on the other side of the boundary). Then, they evaluate the amount of incorrectly predicted points by the boundary and the number of points that match the anticipated flow regime.

The analysis conducted in this study is similar to that carried out by Wu et al. [16]. The results of the evaluation of the different flow regime maps against the experimental data for pipe with $D_H^* > 40$ is plotted in Table 4.1.

The results for the transition boundary from bubble to cap-bubble presented in Table 4.1 give a better index for the Schlegel et al. [32] criteria than for Mishima and Ishii [19] criteria. However, the difference between both is very small. Through visual inspection, it is possible to see that Mishima and Ishii [19] transition criteria does a better job predicting cap-bubble flow (less yellow markers outside of the delimited cap-bubble region). Therefore, considering that negligible difference between both transition boundaries from bubble to cap-bubble and the visually better performance on predicting cap-bubble flow, Mishima and Ishii [19] transition criteria for the transition from bubble to cap-bubble flow will be adopted for the flow regime map in this work.

Hence, the most appropriate transition boundaries are:

Table 4.1. Analysis of conforming and non-conforming experimental data points for different transition boundaries of different flow regime maps.

Transitions	Bubble to cap bubble	Cap bubble to churn	Churn to annular
Exp. Points analyzed	511	399	184
Non-conforming data points			
Duns and Ros [11]	-	132	14
Aziz et al. [17]	191	131	15
Mishima and Ishii [19]	69	115	12
Schlegel et al. [32]	68	44	12
Conforming data points (%)			
Duns and Ros [11]	-	66.92	92.39
Aziz et al. [17]	62.62	66.92	91.85
Mishima and Ishii [19]	86.50	71.18	93.48
Schlegel et al. [32]	86.69	88.97	93.48

- From bubble to cap-bubble: Mishima and Ishii [19]
- From cap-bubble to churn: Schlegel et al. [32]
- From churn to annular: Mishima and Ishii [19]

It is interesting to notice that the selected transition boundaries do not depend on the diameter, as the flow regime transition models of Mishima and Ishii [19] and Schlegel et al. [32] are not diameter dependent for $D_H^* > 30$.

The transitions to and from slug and cap-bubble flow present strong similarities. The transition from bubble to slug or cap-bubble occurs due to high coalescence of bubbles. The bubbles will coalesce and grow until it reaches a constraint, limiting its size. For small diameters, this constraint are pipe walls. Hence, a bullet-shaped bubble occupying the entire diameter is created. In large diameters, the bubble growth is constrained by the force balance between external forces and the surface tension keeping the bubble stable. After reaching this limit, the bubble collapses never reaching the pipe diameter size, but grows to larger sizes than the bubbles in bubble flow. The transition to churn flow in both large

and small diameter pipes, is based on the unsustainable growth of the bubbles, until the turbulence collapses the large bubbles. In other words, just like for very small diameters the pipe geometry makes the existence of bubble flow impossible, for large diameters it is impossible to exist slug flow, which is replaced by the cap-bubble flow. Therefore, the existence or not of slug or cap-bubble flow in a vertical two-phase flow is diameter dependent.

Figure 4.2 shows an exemplification of the process described. The Taylor bubble exists in the smaller diameter pipe, but once the wall constraints are removed, the bubble will grow only up to its next constraint, which is the force balance between the external forces and the surface tension. Considering that the transition mechanisms for both slug and cap-bubble flow are similar, it might be feasible that using the same flow regime map as proposed in this work, i.e., the criteria adopted, one could model a flow regime map that adapts to the diameter size. The transition selected for bubble to cap-bubble is already tried and tested for smaller diameters [19], and in this work proved to work well with large diameters. The transition from cap-bubble to churn is derived from a drift-flux approach and considers a drift velocity developed for cap-bubble flow. However if using a drift velocity developed for slug flow as the one proposed by Ishii [47], given as:

$$\langle\langle V_{gj} \rangle\rangle = 0.35 \sqrt{g D_H \left(\frac{\Delta \rho}{\rho_l} \right)} \quad (4.1)$$

to calculate the transition instead when the diameter is deemed small (i.e., $D_H^* < 40$), this flow regime map might adapt to smaller diameters as well.

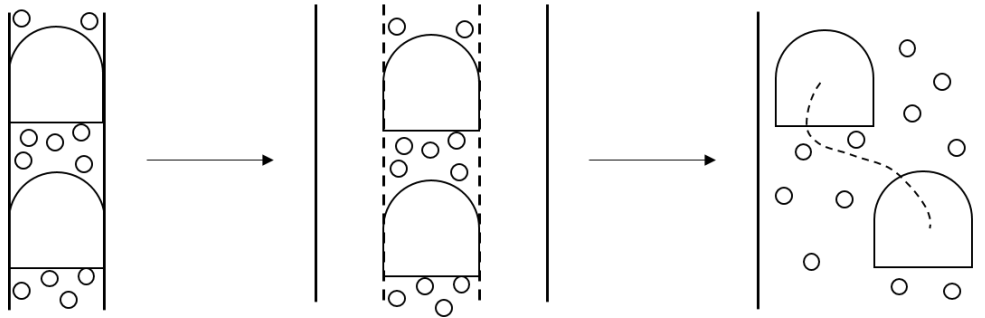


Figure 4.2. Slug flow development depending on pipe diameter.

Kataoka and Ishii [25] also notice from experimental results that for a flow of air and water at standard conditions, even in pipe diameters as small as 0.06 m the slug flow regime is better characterized by the drift-flux equation considering cap-bubble flow (Eq. 2.64).

4.2 Computational Fluid Dynamic (CFD) observations

Waltrich et al. [9] used Computational Fluid Dynamics (CFD) approach to calculate pressure gradient for a few experimental conditions from their own experimental data for the 0.30 m diameter pipe and for the 0.25 m diameter pipe from Ali and Yeung [24] study. The data considered is show in Table 4.2.

Table 4.2. Experimental data considered for calculation of pressure gradient with CFD on Waltrich et al. [9].

Author	ID (m)	Test	u_{sl} (m/s)	u_{sg} (m/s)
Ali and Yeung [24]	0.25 m	1	0.981	0.094
		2	1.036	0.774
		3	1.100	2.106
Waltrich et al. [9]	0.30 m	1	0.728	0.701
		2	0.732	3.438
		3	0.186	3.676
		4	0.030	3.728
		5	0.720	7.220
		6	0.418	7.480

Fig 4.3 presents these experimental data points on the newly defined flow regime map. The labels inside each data point in Fig 4.3 identify the respective test as shown in Table 4.2. As it is possible to see, most of the data from Waltrich et al. [9] appears on the churn flow regime region, while for Ali and Yeung [24] data, the experimental data points are more spread, with flows in bubble and cap-bubble flow regimes. The data-point with the highest gas superficial velocity appears to be almost in churn flow regime. The flow regime experimental observations for the points correspondent to test 1 and 4 for Waltrich et al. [9] data are bubble and churn flow, respectively.

Figs. 4.4 and 4.5 present frames of the CFD simulated flow visualization for the results

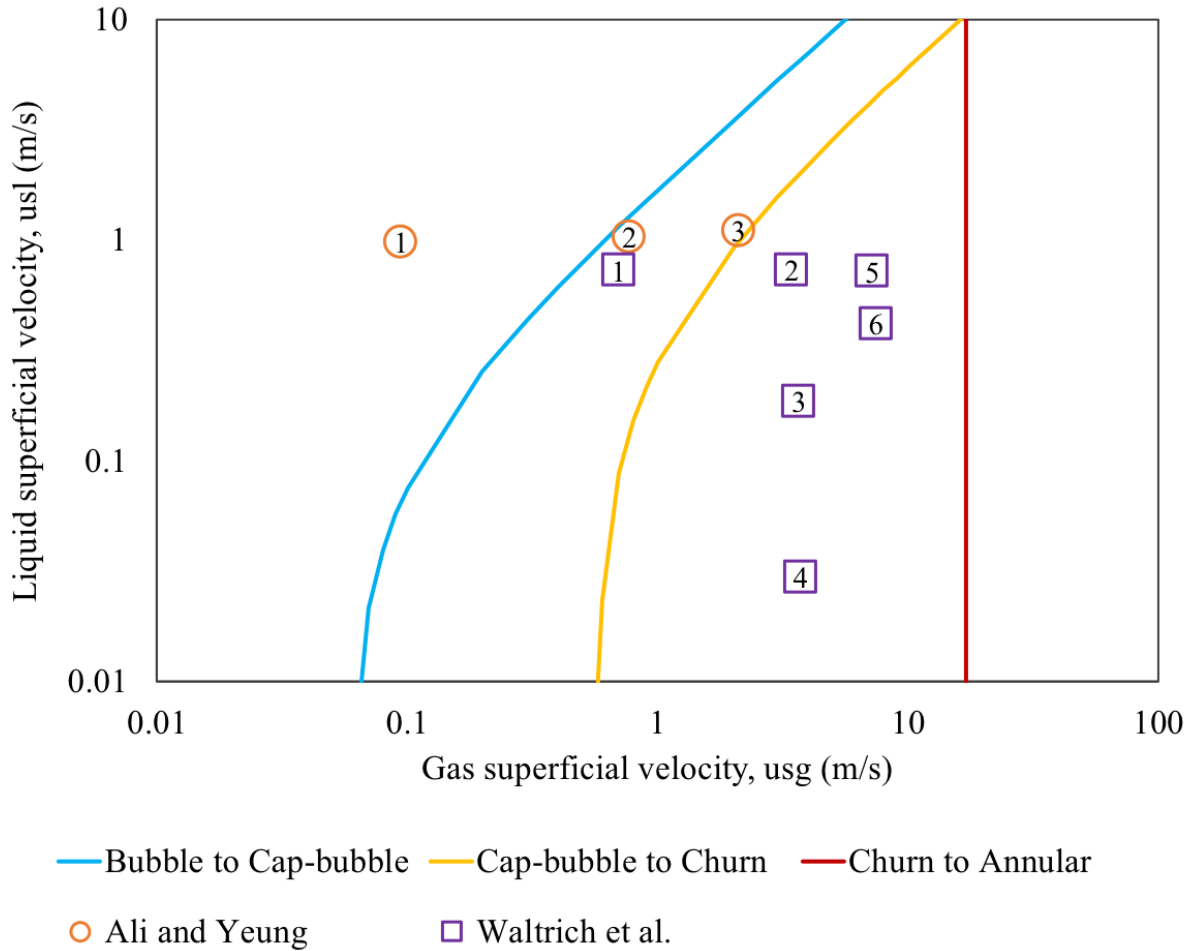


Figure 4.3. Data points evaluated with CFD on Waltrich et al. [9] work plotted on newly proposed flow regime map.

from Ali and Yeung [24] and Waltrich et al. [9] results. The numbering below each picture corresponds to the test identification, as shown in Table 4.2.

As it is possible to see in Fig. 4.4, the flows from Test 1 to 3 present increasing gas throughput. The first flow regime appears to have very little gas bubbles flowing upwards, concentrated in the center of the water column, characterizing bubble flow. As the gas injection increases, the bubbles in Test 2 start to grow bigger and coalesce while still flowing mainly upwards. These features characterize the cap-bubble flow. Finally, on Test 3, these bubbles grow to an even larger size, starting to become very unstable and generating strong flow oscillations. The flow becomes very turbulent. This condition defines the transition



Figure 4.4. CFD visualization of experimental data points reported by Ali and Yeung [24] presented in Table 4.2.

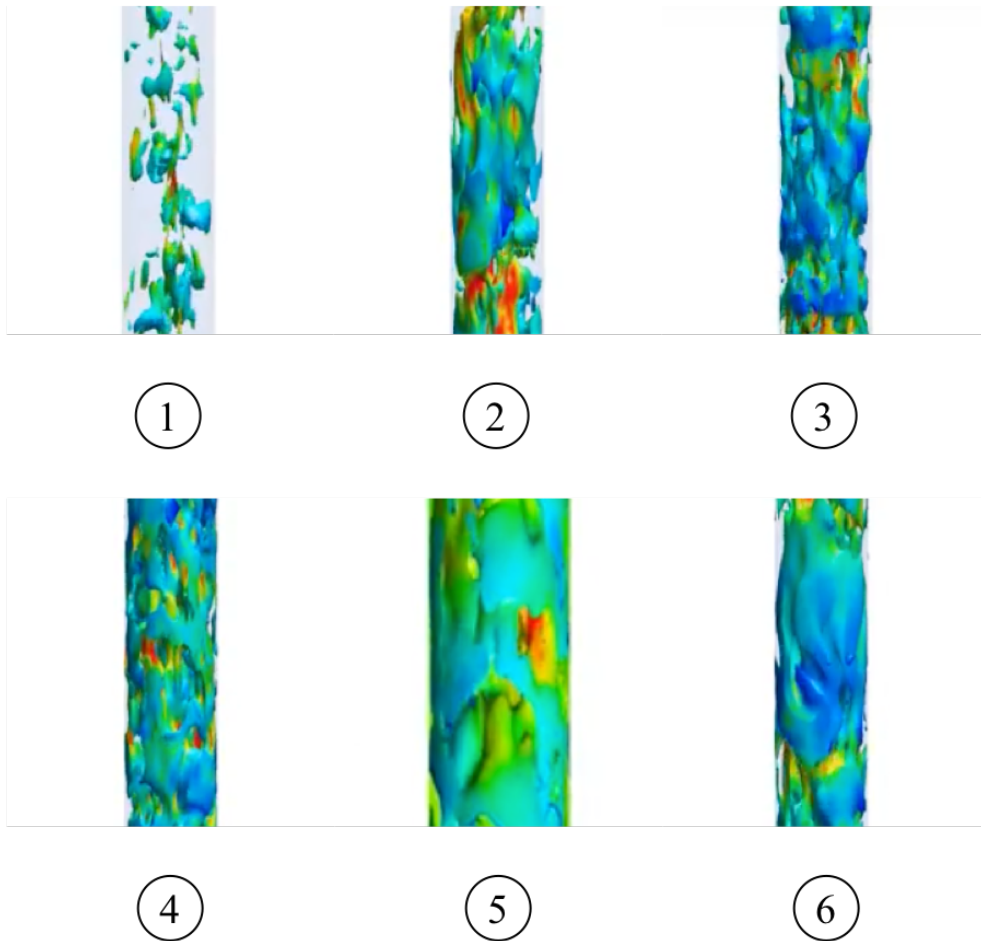


Figure 4.5. CFD visualization of experimental data points reported by Waltrich et al. [9] presented in Table 4.2.

between cap-bubble flow and churn flow.

In Fig 4.5, the frame captured from the CFD visualization for Test 1 presents a pattern very similar to that seen on Test 2 in Fig 4.4. Therefore, the flow regime is cap-bubble flow. It is important to notice here that although this differs from the experimental observation, it agrees very well with the flow regime map prediction. The disagreement with the experimental observation can be explained due to the difficulty of visually differentiating certain features between cap-bubble and bubble flow. Fig 4.6 presents a frame of the video recorded during the Test 1 experiment. As it is possible to see, the light penetration in the pipe is very poor and it is hard to assess how big the bubbles are. In these cases, the visual observation helped differentiating the flow from bubble (or cap-bubble) to churn, once it is flowing upwards.



Figure 4.6. Flow regime observation for Test 1 from Waltrich et al. [9] conditions.

Tests 2 through 6 in Fig 4.5 have strong characteristics of churn flow, with high turbulence levels and flow recirculation. In the case of Test 4, the visualization from the CFD simulation agrees very well with the experimental observation and the prediction from the flow regime map. All the CFD visualizations agree well with the flow regime map prediction.

4.3 Flow regime map validation

The flow regime map proposed in this work was tested with an adaptation of the model introduced in Chapter 2. Three cases were considered:

- LSU experimental data points, considering both every experimental data points available and only those that did not have identified flow regime (and thus were not used to test the transition boundaries for the flow regime map);
- The oil and gas case by Asheim [65], where the wells had low gas-oil-ratios
- The water and gas case by Reinicke and Remer [68], where the wells had high gas-oil ratios.

To validate the flow regime map proposed in this work, the model developed by Teles and Waltrich [33] will be used, along with a modified version of this model, adding the new flow regime map and the estimation of pressure gradient when the flow regime is considered to be of cap-bubble flow. A drift-flux model will be implemented to the numerical code to calculate this pressure gradient. Figure 4.7 represents the diagram of the adaptation proposed by this work for the calculation of two-phase flow in large diameter pipes. As it is possible to see, the structure is similar to the model proposed by Teles and Waltrich [33], with the addition of the new flow regime map and the calculation of the pressure gradient for the cap-bubble flow, predicted on the new map.

Drift flux model

The drift-flux models for two-phase flow are based on a constitutive relation to accounting for the relative motion between the liquid and gas phases.

When considering a one-dimensional drift-flux model, the relative velocity is given by [47]:

$$(1 - \alpha)u_r = (C_0 - 1)u_m + \langle\langle V_{gj} \rangle\rangle \quad (4.2)$$

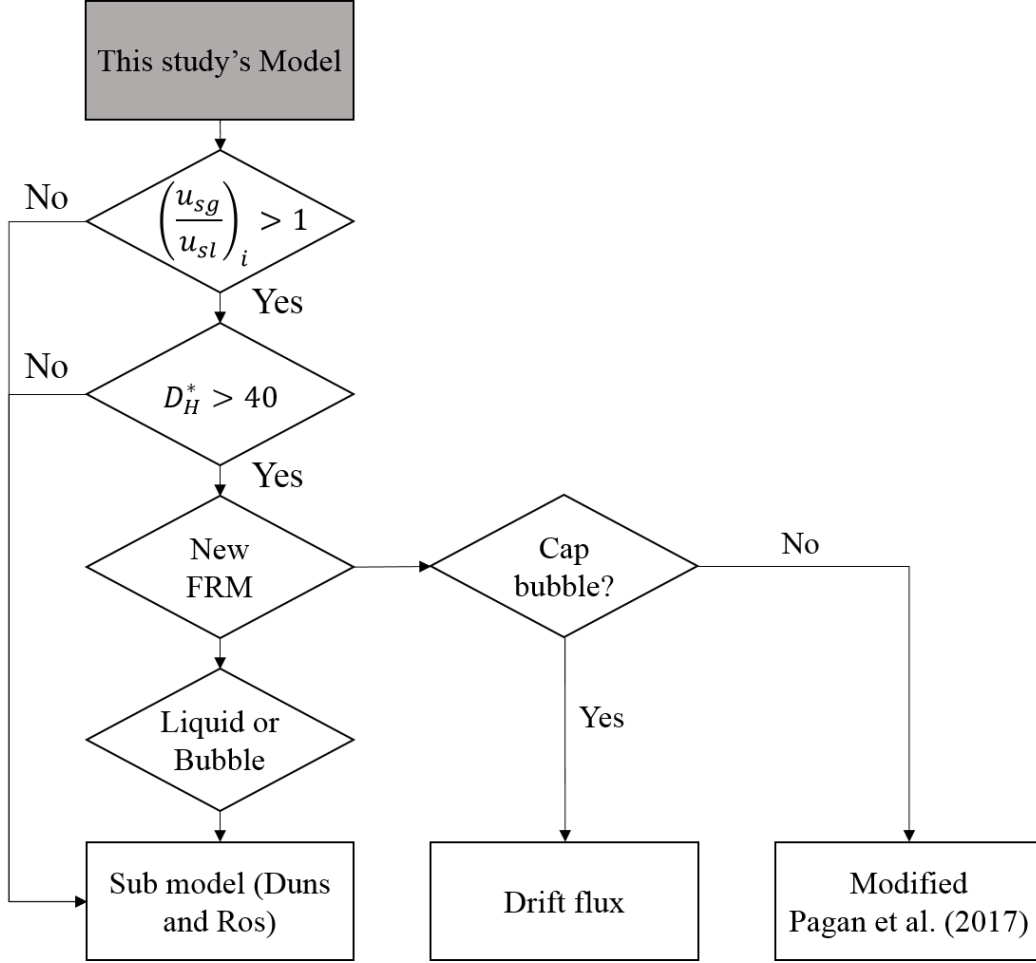


Figure 4.7. Modified diagram proposed by this work for the model developed by Teles and Waltrich.

where u_r is the relative velocity, C_0 is the distribution parameter, and $\langle\langle V_g j \rangle\rangle$ is the void-fraction weighted area average of the local drift velocity. The relative velocity, u_r can be calculated as:

$$u_r = u_g - u_l \quad (4.3)$$

The average gas and liquid velocities can be correlated to the void-fraction as:

$$u_g = \frac{u_s g}{\alpha} \quad (4.4)$$

and

$$u_l = \frac{u_s l}{1 - \alpha} \quad (4.5)$$

The void fraction can be calculated as:

$$\alpha = \frac{u_s g}{C_0 u_m + \langle \langle V_{g,j} \rangle \rangle} \quad (4.6)$$

Hibiki and Ishii [14] recommended the use of Kataoka and Ishii [25] drift-flux correlation for cap-bubble flow regime. According to Kataoka and Ishii [25], the drift velocity in large-diameter pipes is dependent on the diameter, pressure, gas flux, and fluid physical properties, and can be calculated by Eq. 2.64. The distribution factor C_0 , can be calculated with Eq. 2.44.

Once the void-fraction is calculated, it is possible to estimate the pressure drop. The pressure gradient equation for multiphase flow can be used by considering the fluids as a homogeneous mixture as (Shoham, 2006):

$$\frac{dp}{dL} = \left(\frac{dp}{dL} \right)_{gravitational} + \left(\frac{dp}{dL} \right)_{frictional} + \left(\frac{dp}{dL} \right)_{accelerational} \quad (4.7)$$

In general, the gravitational pressure gradient is based on the in-situ mixture density, ρ_m , as

$$\left(\frac{dp}{dL} \right)_{gravitational} = \rho_m g \sin \theta \quad (4.8)$$

The frictional pressure drop can be calculated based on the Fanning friction factor, f , as:

$$\left(\frac{dp}{dL} \right)_{frictional} = \frac{2f \rho_m u_m^2}{D} \quad (4.9)$$

The Reynolds number for a two-phase flow mixture can be calculated as:

$$\text{Re}_m = \frac{\rho_m u_m D}{\mu_m} \quad (4.10)$$

where ρ_m is the mixture density and μ_m is the two-phase viscosity, given respectively by:

$$\mu_m = \alpha \mu_g + (1 - \alpha) \mu_l \quad (4.11)$$

$$\rho_m = \alpha \rho_g + (1 - \alpha) \rho_l \quad (4.12)$$

Due to the low acceleration, the kinetic energy variation for flows far from critical velocity is negligible. Therefore the accelerational pressure gradient will be neglected in this approach. The pressure gradient will then be estimated as:

$$\frac{dp}{dL} = \rho_m g \sin \theta + \frac{2f \rho_m u_m^2}{D} \quad (4.13)$$

Error calculation method

The absolute error for the results is calculated by:

$$\varepsilon (\%) = \frac{1}{n} \left(\sum_{n=1}^n |\varepsilon_{R,i}| \times 100 \right) \quad (4.14)$$

where n is the number of measured data points the relative error is:

$$\varepsilon_{R,i} (\%) = \frac{|x|_{\text{simulated}} - |x|_{\text{measured}}}{|x|_{\text{measured}}} \quad (4.15)$$

where x is the variable of interest (pressure gradient). The standard deviation for the average absolute error for each scenario, which is calculated as,

$$\text{SDev} (\%) = \sum_{n=1}^n \sqrt{\frac{(\varepsilon - \varepsilon_{R,i})^2}{n}} \quad (4.16)$$

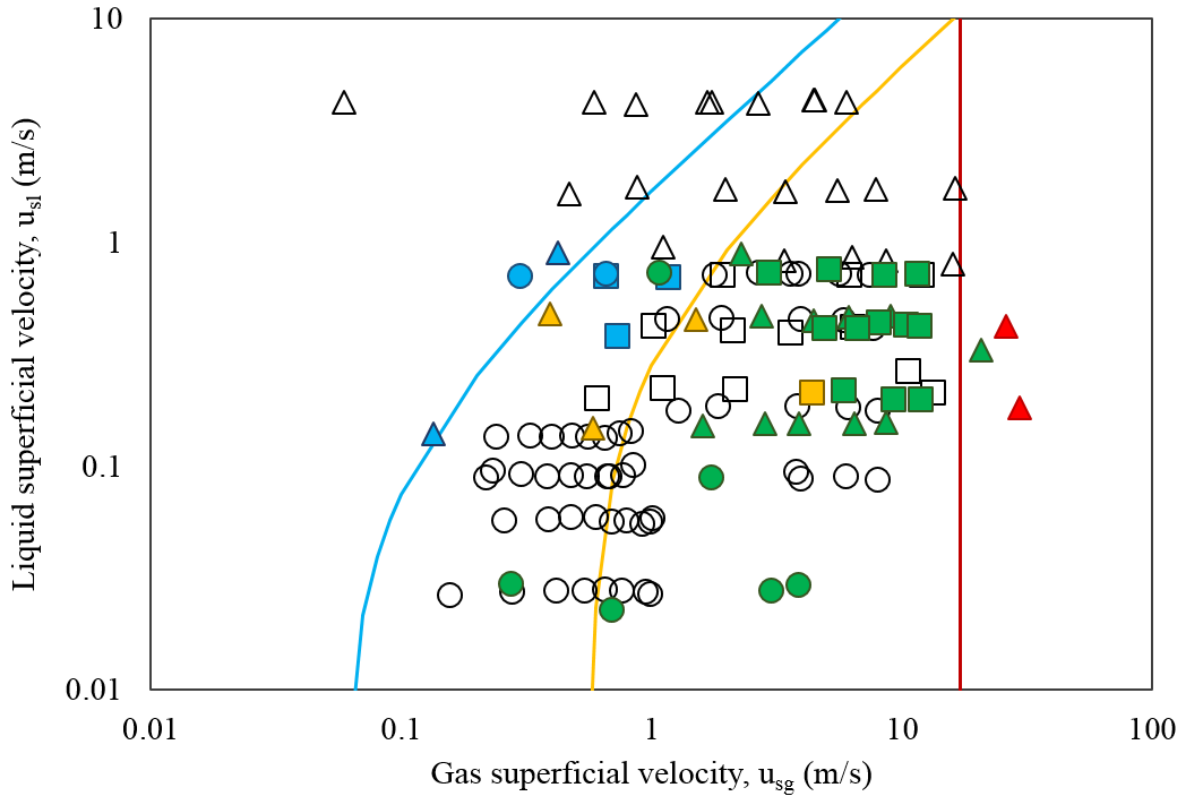
4.4 Water and air – Data from Waltrich et al. [9]

Figure 4.8 shows the experimental data extracted from Waltrich et al. [9] points plotted over the newly proposed flow regime map. As it is possible to see, the map matches well with the churn and annular flow observations. However, it only achieves 50 % of conforming cap-bubble and only about 43 % bubble flow prediction. This may be due to the difficulties of visually identifying flow regimes in large diameter pipes. As it is possible to see, for the 0.10 m pipe the predicted flow regime matches very well with the observed, while the highest errors are for the 0.20 m diameter pipe, which have metal walls and do not allow the direct visualization of the flow.

Figure 4.9 shows the absolute averaged error for the pressure gradients using the model presented in Figure 4.7 and the model by Teles and Waltrich [33]. The standard deviation of the absolute error is also plotted in the figure as the deviation bars. The results were compared only for the data points that are estimated as cap-bubble flow by the flow regime map proposed in this work. Conditions to which more than 10% of the total flow length was of a different flow regime were not considered in this comparison.

It is possible to see a considerable drop in the error for the cases where the new map considered cap-bubble – and that the pressure drop was calculated as such. It is also possible to notice that the error difference appears to be reduced with the increasing pipe diameter. One conceivable explanation is that due to the broader space that the flow has on the larger diameter, the cap-bubbles are not as relevant to the pressure drop and, once they grow to a size which has enough influence, the turbulence is already high enough so that the flow is already almost configured as churn flow. This conclusion might be biased once it is considered factors such as the different flow velocities of the data considered for each pipe diameter, or even the amount of data-points.

In order to reduce the bias of the previous analysis, it is important to compare the error for similar conditions. This way, a few data-points for each diameter under similar liquid and gas superficial velocities were selected. Two groups with data for the three different



- Bubble to Cap-bubble — Cap-bubble to Churn — Churn to Annular
- △ ID = 0.10 m - Unidentified □ ID = 0.20 m - Unidentified ○ ID = 0.30 m - Unidentified
- ▲ ID = 0.10 m - Bubble ■ ID = 0.20 m - Bubble ● ID = 0.30 m - Bubble
- ▲ ID = 0.10 m - Cap-bubble ■ ID = 0.20 m - Cap-bubble ● ID = 0.30 m - Churn
- ▲ ID = 0.10 m - Churn ■ ID = 0.20 m - Churn
- ▲ ID = 0.10 m - Annular

Figure 4.8. Proposed flow regime maps with all experimental data points produced at LSU, classified into the four flow regimes considered in this work, plus the data points without identified flow regimes. The different symbols represent the different pipe diameters: Δ represents the 0.10 m, \square represents the 0.20 m, and \circ represents the 0.30 m. The different colors represent the observed flow regime: blue is bubble flow, yellow is cap-bubble flow, green is churn flow, red is annular flow, and the shapes without fill represent the data points that did not have an identified flow regime. The lines represent the flow regime boundaries: the blue represents the transition from bubble to cap-bubble, the yellow from cap-bubble to churn, and the red is for churn to annular flow.

diameters were identified: (i) $u_{sl} \sim 0.7\text{-}0.9$ m/s and $u_{sg} \sim 1.75\text{-}2.30$ m/s; and (ii) $u_{sl} \sim 0.13\text{-}0.20$ m/s and $u_{sg} \sim 0.58\text{-}0.74$ m/s. The calculated absolute error for two groups by each of the two analyzed models is presented in Table 4.3. As can be seen, once more the error in the 0.30 m diameter pipe appear to be closer for the two different models than the

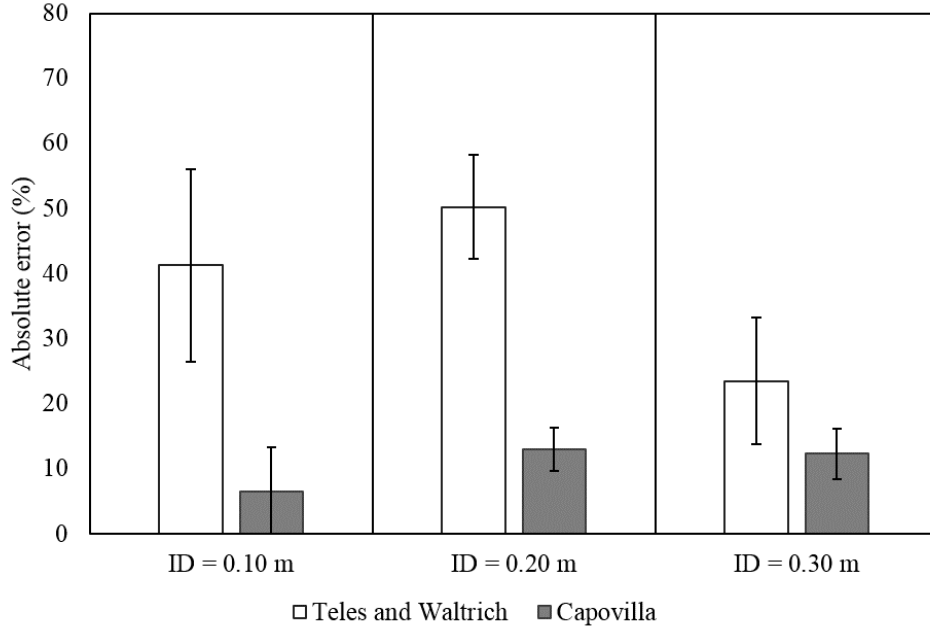


Figure 4.9. Comparison of errors in pressure gradient calculation for the experimental data reported by Waltrich et al. [9] predicted to be in cap-bubble flow by the flow regime map proposed in this work, simulated with the model proposed by Teles and Waltrich and with the modification proposed in this work. All data produced at LSU was considered in this comparison.

error in the 0.10 and 0.20 m pipes. The difference between the two models error also appear to be reducing with pipe diameter.

Table 4.3. Comparative of calculated absolute error with the model proposed in this work and the model by Teles and Waltrich for groups of data points with different diameters and similar conditions.

ID (m)	u_{sl} (m/s)	u_{sg} (m/s)	ε_{abs} - Capovilla	ε_{abs} - Teles and Waltrich
0.10	0.885	2.285	18.07	52.28
0.20	0.720	1.907	14.22	43.50
0.30	0.724	1.782	11.69	15.95
0.10	0.147	0.582	1.47	44.17
0.20	0.203	0.600	11.17	44.28
0.30	0.134	0.649	14.81	28.52
0.30	0.141	0.740	16.91	29.23

The absolute averaged error for the dp/dz was also plotted considering only the

experimental data not used on the development of the flow regime map, to eliminate biased results. The errors are plotted in Figure 4.10. As it is possible to see, the tendency seen in the previous plot is kept, and therefore it is considered that the results are not biased.

One of the criteria considered by Teles and Waltrich [33] to make use of the Duns and Ros [31] model to calculate the pressure gradient is that the slip ratio is less than 1, as shown in Figures 2.1 and 4.7. Most of the data presented for the 0.10 m pipe in Figure 4.8 in the cap-bubble flow region have slip-ratios around 1. Therefore, even though it appears that several data points for the 0.10 m diameter pipe are under cap-bubble flow conditions, the model only considers those with slip-ratio higher than 1 as something other than bubble. This way, only one point had its pressure gradient calculated by the cap-bubble model, and only this data is plotted in Figure 4.10. The rest of the data points with slip ratios lower than 1 were considered at bubble flow by the model. This explains the absence of a standard deviation bar on the plot for this pipe diameter.

The accuracy of the new model proposed in this study is compared against well accepted models in the industry in Fig 4.11. As it is possible to see, the addition of the cap-bubble flow regime to Teles and Waltrich [33] model significantly reduced the errors in the pressure gradient prediction, bringing it down to the same level as the best performer models evaluated here.

It is interesting to notice how Duns and Ros [11] model performs well in this region. Duns and Ros [11] flow regime map considers most of the region considered as cap-bubble in the newly proposed flow regime map as being in the liquid dominated region, which also applies to cap-bubble. The empirical conditions at which their model was developed also approximately matches with the conditions of the experiments in the two smaller diameters, which can explain the good agreement.

Hagerdorn and Brown [35] model also presents a very good accuracy. This model is an empirical flow regime independent model. The experimental conditions considered when

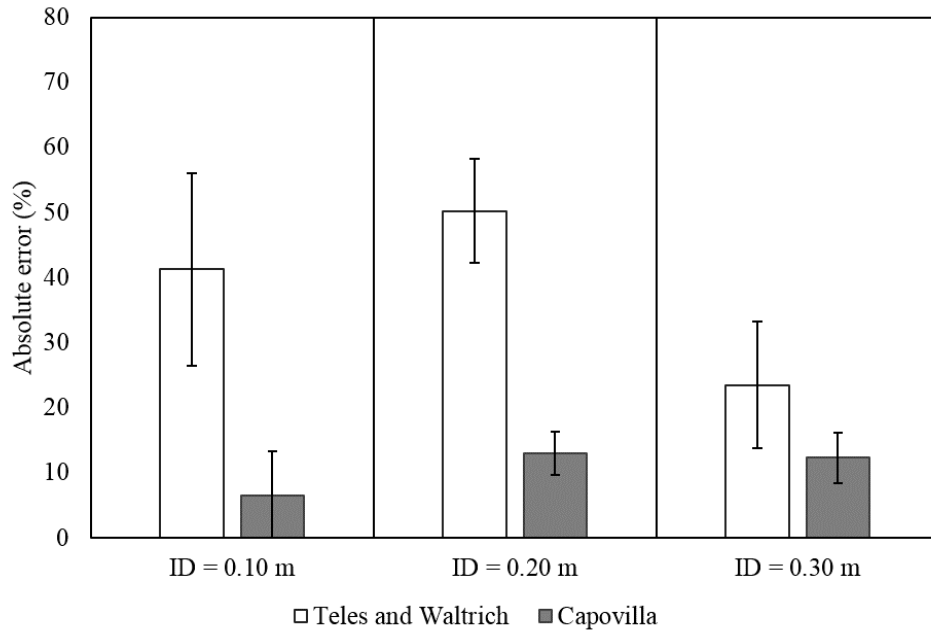


Figure 4.10. Comparison of errors in pressure gradient calculation for the experimental data reported by Waltrich et al. [9] predicted to be in cap-bubble flow by the flow regime map proposed in this work, simulated with the model proposed by Teles and Waltrich [33] and with the modification proposed in this work. Only data without identified flow regimes from LSU (i.e., that were not used to evaluate the flow regime transitions) were considered.

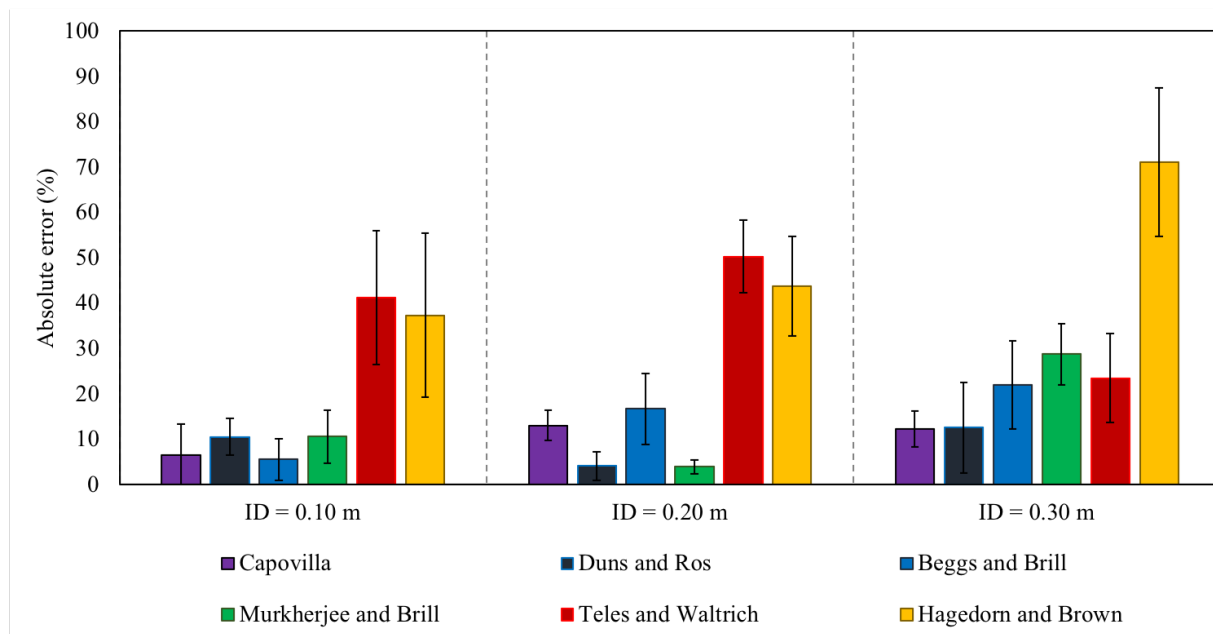


Figure 4.11. Comparison of pressure gradient prediction accuracy between renowned models and the new models by Teles and Waltrich [33] and the model proposed in this study for conditions predicted as cap-bubble flow in the newly proposed flow regime map.

developing this model included small diameter tubing (between 0.02 up to 0.04 m) flowing oil and gas or water and gas. Even though these conditions differ to those considered here, they might become similar due to the effect seen in Fig 1.6. The good agreement is an indicative that Kataoka and Ishii [25] criteria for large diameter and the existence of slug flow might be valid for oil and gas.

4.5 Oil and gas – Data from Asheim [65]

The pressure gradient for the 37 wells from Asheim [65] work was simulated using both Teles and Waltrich [33] model and the model modified in the present work. The averaged absolute error for each model is plotted in Figure 4.12. The error bars represent the standard deviation of the absolute error. As it is possible to see, the error for the simulations using the modification applied in this work is smaller than when using the standard model by Teles and Waltrich [33]. In Asheim [65] report there is no information about flow regimes, but the smaller error is a sound indication of a more accurate flow regime map.

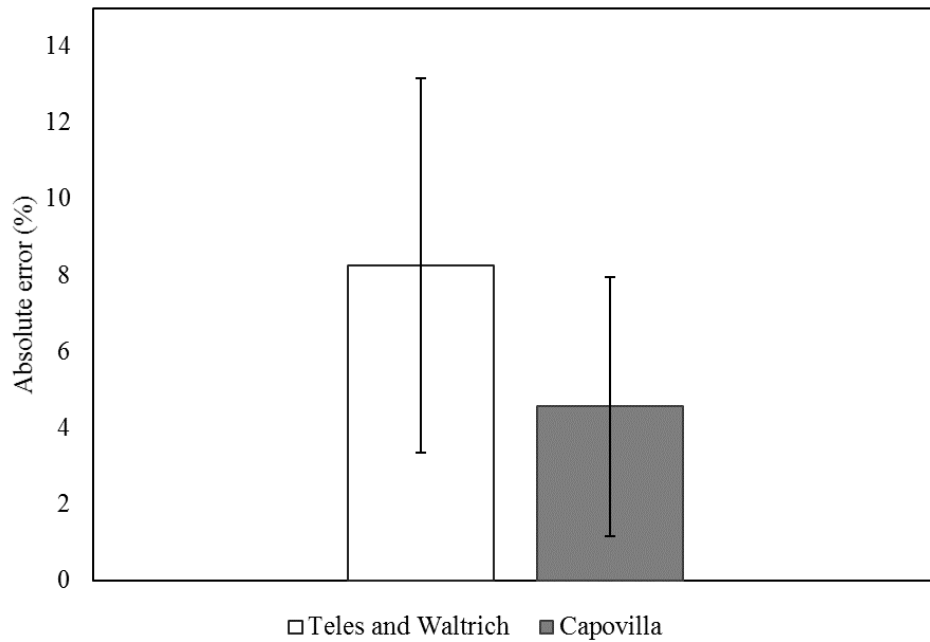


Figure 4.12. Comparison of errors in pressure gradient calculation for the data reported by Asheim [65], simulated with the model by Teles and Waltrich and with the modification proposed in this work.

As it is possible to see from Figure 4.12, for oil and gas the modified model proposed in

this work also performs well, presenting lower errors than Teles and Waltrich [33] model, which do not consider cap-bubble flow. Another relevant information is that most of the flow in the simulated wells was in liquid single-phase flow. Therefore, only part of the wells were estimated to be in cap-bubble flow.

4.6 Critical flow

The model proposed by Wallis [41] for the calculation of the critical flow mixture velocity for a two-phase flow was used to calculate the critical velocity for water-and-air and oil-and-gas mixtures. It used black oil correlations and natural gas with the composition presented in Table 4.4 to calculate the critical mixture velocity for oil-and-gas. Two different cases are considered: high and a low-pressure conditions. The high-pressure case for both mixtures (water-and-air and oil-and-natural gas) was of 9.62 MPa (1,395 psi), while the low pressure for oil-and-gas was of 206.8 kPa (30 psi) and for water-and-air, it was standard conditions. Figure 4.13 presents a comparison of the critical mixture velocity versus the liquid holdup for each fluid under the different pressures compared. When the void fraction is equal to zero, the critical velocity shown in the plots in Figuree 4.13 is equivalent to the liquid-phase critical velocity. Likewise, when the void fraction is 1, the critical velocity is equivalent to the gas-phase critical velocity.

Table 4.4. Natural gas composition considered for the calculation of the critical mixture velocity.

Component	Quantity (%)
Methane	96.5
Ethane	1.80
Propane	0.45
Iso-butane	0.10
n-Butane	0.10
Iso-pentane	0.05
n-Pentane	0.03
n-Hexane	0.07
Nitrogen	0.30
Carbon Dioxide	0.60

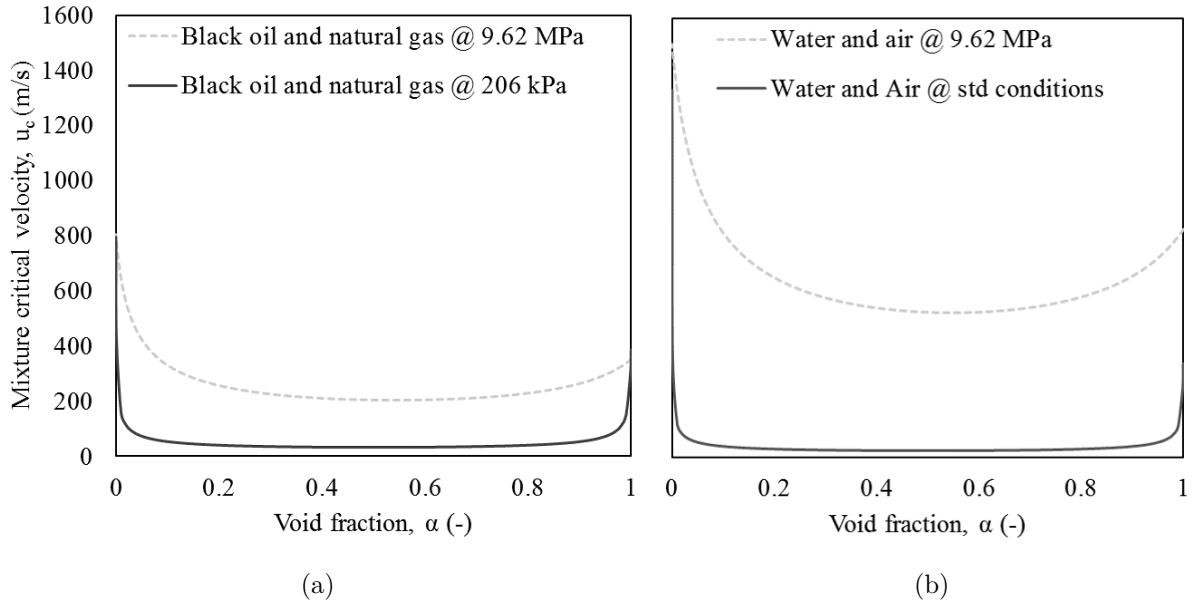


Figure 4.13. Comparative of the effect of pressure on the critical mixture velocity for mixtures of (a) black oil and natural gas, and (b) water and air.

Eq. 2.66 will be presented here again to make it easier to analyze the effect of its different parameters on the calculation of the critical mixture velocity.

$$u_{m,c} = \left[(\lambda_g \rho_g + \lambda_l \rho_l) \left(\frac{\lambda_g}{\rho_g u_{g,c}^2} + \frac{\lambda_l}{\rho_l u_{l,c}^2} \right) \right]^{-0.5}$$

The acoustic velocity in gases, fluids, and solids can be defined based on Hookes law as:

$$u_c = \sqrt{\frac{dp}{d\rho}} = \sqrt{\frac{K}{\rho}} \quad (4.17)$$

where K is the bulk modulus of elasticity. Rearranging Eq. 4.17 to solve for K, it will become:

$$K = \rho u_c^2 \quad (4.18)$$

Wallis [41] approach considers the mixture a single fluid with equivalent properties, as exemplified by Figure 4.14.

Therefore, looking at Eq. 2.66 it is possible to identify Eq. 4.17 format as:

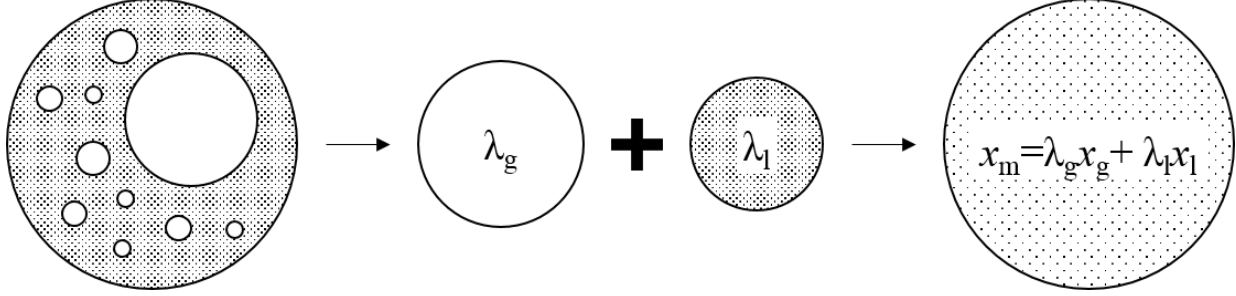


Figure 4.14. Example calculation of an equivalent property for a two-phase mixture being assumed as a homogeneous fluid.

$$u_{m,c} = \left(\frac{\text{Mixture density}}{\text{Mixture bulk modulus}} \right)^{-0.5} \quad (4.19)$$

$$\text{Mixture density} = \lambda_g \rho_g + \lambda_l \rho_l \quad (4.20)$$

$$\text{Mixture bulk modulus} = \frac{1}{\lambda_g} \rho_g u_{g,c}^2 + \frac{1}{\lambda_l} \rho_l u_{l,c}^2 \quad (4.21)$$

The bulk modulus is a property related to the compressibility of the material. It measures the amount of pressure required to change one unit of volume of this material. This explains why the bulk modulus is considered inversely proportional the fluid holdup in Eq. 2.66. It is proportional to the area that the fluid is occupying, which can be related to the respective fluid holdup.

Due to the mechanical wave nature of the sound, its propagation velocity in a material has strong influence of its density and bulk modulus. A higher density should reduce the critical velocity once more weight requires more energy to be moved by the wave. On the other hand, a higher bulk modulus means a higher acoustic velocity in a material, once the closer bounded particles facilitate its propagation. Therefore, it is expected that the critical mixture velocity will be at its lowest on intermediate void fractions, once the gas has a low bulk modulus, but a low density, and the liquid presents a higher bulk modulus, but also a higher density.

With pressure variations, the property that will be the most influenced in Eq. 2.66 is the gas density, due to its high compressibility (and consequent low bulk modulus). With the gas density increase, it would be expected a drop on the mixture critical velocity. However, the increase of the gas density will have a bigger impact on the mixture bulk modulus, strongly increasing it. As it is expected, the more compressed a fluid is the more difficult it will be to farther compress it. Hence, a higher bulk modulus is expected under higher pressures. WCD events and sub-sea releases will occur at high pressures. Therefore, the effect of pressure becomes very important, once the deeper the release, the higher the $u_{m,c}$. In other words, the deeper the discharge is, the more difficult it will be that the discharge is under critical flow conditions.

The effect of the difference on bulk modulus and fluids density can also be seen in Figure 4.15, where the critical mixture velocity as a function of the void fraction is compared to two different mixtures under the same high pressure (9.62 MPa). Because of the difference between natural gas and air densities, the water-air mixture have a higher critical mixture velocity than the oil-gas mixture. While the natural gas density for such conditions is of 82.7 kg/m^3 (5.16 lbm/ft^3), the air density is of 116 kg/m^3 (7.26 lbm/ft^3). Other factors such as the difference between the gas and liquid critical velocities (lower for both oil vs. water and natural gas vs. air comparisons), and oil density (also lower than water density) have influence on the difference seen in Figure 4.15 as well.

The work of Zulqarnain [3] presented a statistical study of a representative well for the Gulf of Mexico during a blowout. Figure 4.16.a provides the information of the statistically representative black oil well in the GoM from Zulqarnain [3] work. The figure also shows information on the flow velocities and exit pressure for a sub-sea and surface releases, represented by the subscripts SS and SR, respectively. A sub-sea release is a condition when the oil spill happens at the bottom of the sea, under high pressure exerted by the water hydrostatic, while a surface release is an event when the oil spill occurs at the surface (for instance, at the rig floor), under atmospheric pressure. Figure 4.16.b shows those velocities

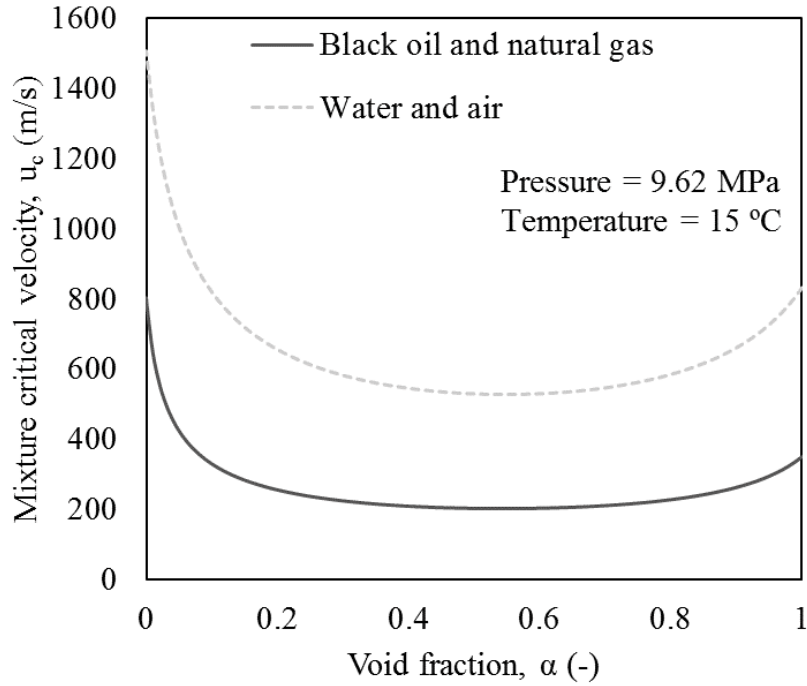


Figure 4.15. Mixture critical velocity and void fraction relation for black oil and natural gas, and water and air mixtures. The considered conditions are a 9.62 MPa pressure and 15 °C temperature.

and the critical flow transition boundary, calculated with Wallis [41] equation for the exit conditions for sub-sea release and for surface release. The dotted area represents the region where the flow would be considered critical for a surface release, while the hachured area represents the region where the flow would be considered critical for a sub-sea release. Each data point corresponds to the conditions given to the different diameters considered in the well. It should be noticed that for the calculation of the critical curve, it was considered that the discharge of any of the different diameter pipes is discharging at the exit pressure (e.g., 9.62 MPa for sub-sea and 206.8 kPa for the surface release). According to Beck et al. [61], Wallis [41] equation underestimates the critical flow conditions. Therefore, for a sub-sea release, the critical conditions for this representative case appears to be considerably far from the considered data points. However, for a surface release, the conditions are close to critical. In other words, the worst-case discharge condition may be very close to the critical flow, which would mean that any of the current pressure gradient prediction models

(to the knowledge of the author) are appropriate.

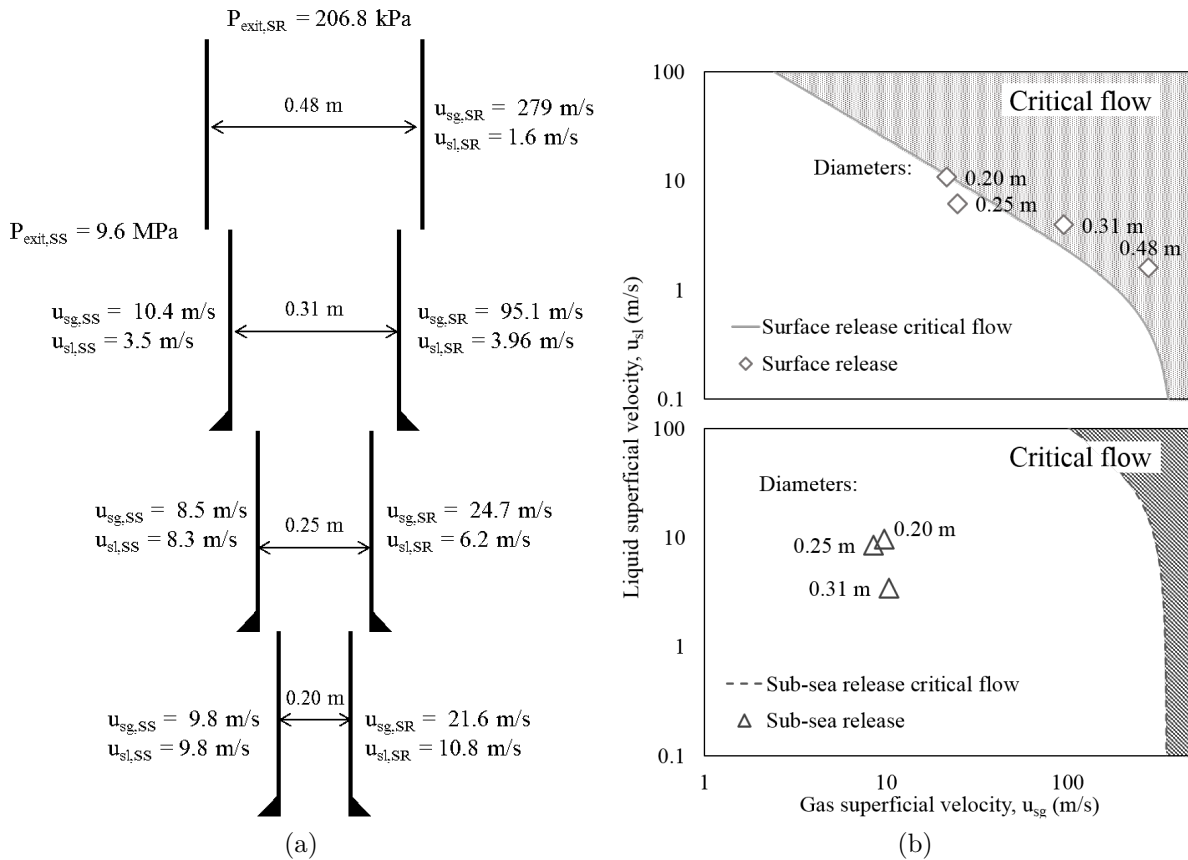


Figure 4.16. (a) Representative model well in the Gulf of Mexico region during a blowout (Zulqarnain [3]); and (b) critical flow transition boundary considering a surface (top) and sub-sea release (bottom).

Figure 4.17 shows the data by Zulqarnain [3] plotted against the critical transition criteria by Wallis [41] and its modification by Beck et al. [61]. The modified criteria by Beck et al. [61] was calculated for each different diameter. Each curve has its respective diameter displayed by its side. As it is possible to see, when considered the diameter dependent multiplier, the data points by Zulqarnain [3] appear in subcritical condition. However, this situation should be taken with caution, once the HEM model by Wallis [41] estimates that those flows would be in critical condition. As a safe rule of thumb, it is possible to say that if the flow is in subcritical condition according to Wallis [41] criteria, it most probably is subcritical. Conversely, if the flow is in critical condition according to the modified method proposed by Beck et al. [61], it should be indeed in critical conditions. The area between

these two criteria should be taken with discretion.

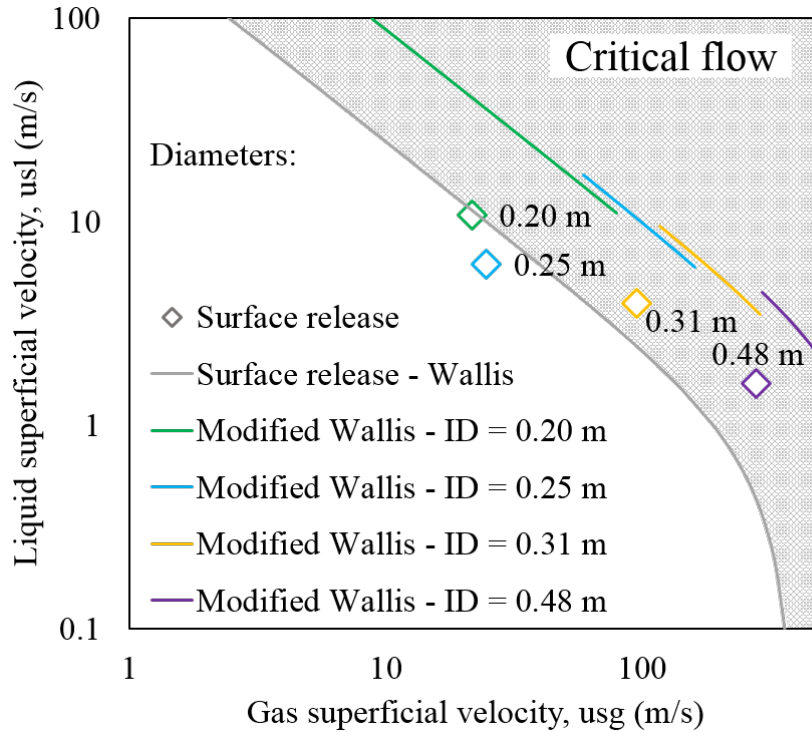


Figure 4.17. Surface release data points by Zulqarnain [3] plotted with Wallis [41] critical flow transition criteria and its modification by Beck et al. [61]. The respective diameter of each data point and for each modified critical velocity curve is displayed by its side.

One famous case that may be recalled when analyzing critical flows during WCD events is the Macondo well blowout. The Macondo well was drilled to a total depth of more than 5,580 m (~18,307 ft), including a water depth of more than 1,500 m (~5,000 ft). That water depth results in a 15.6 MPa (~2,300 psi) pressure on top of the wellhead. Referring to Figure 4.16.b, considering that the pressure for which the critical curve transition was calculated for was of less than 10 Mpa (~1,450 psi), it is only expected that the critical velocity transition boundary will shift to even higher velocities. Therefore, it is highly unlikely that the release at the sea floor from the Macondo well was at critical flow conditions.

Currently, the number of studies of two-phase flow in large diameter pipes is still limited. The research becomes even scarcer when considering very high liquid and gas velocities. As can be seen in Figure 4.18, most of the experimental observation of flow regimes considered in this study do not come close to the critical flow transition, while some are higher than

critical conditions. It should be noticed that the critical flow experimental data plotted in Figure 4.18 is that reported by Beck et al. [61] for water and natural gas two-phase flow, while the critical curve by Wallis [41] criteria was calculated considering water and air. Therefore, the transition is not accurate for the experimental data conditions. However, as this figure is only for demonstration purposes, and as most of the data presented are for air and water, it was considered adequate to calculate the critical flow transition for these fluids. In order to have a more direct comparison of the position of the critical flow experimental data with an accurate critical flow transition curve, please refer to Figure 2.13.

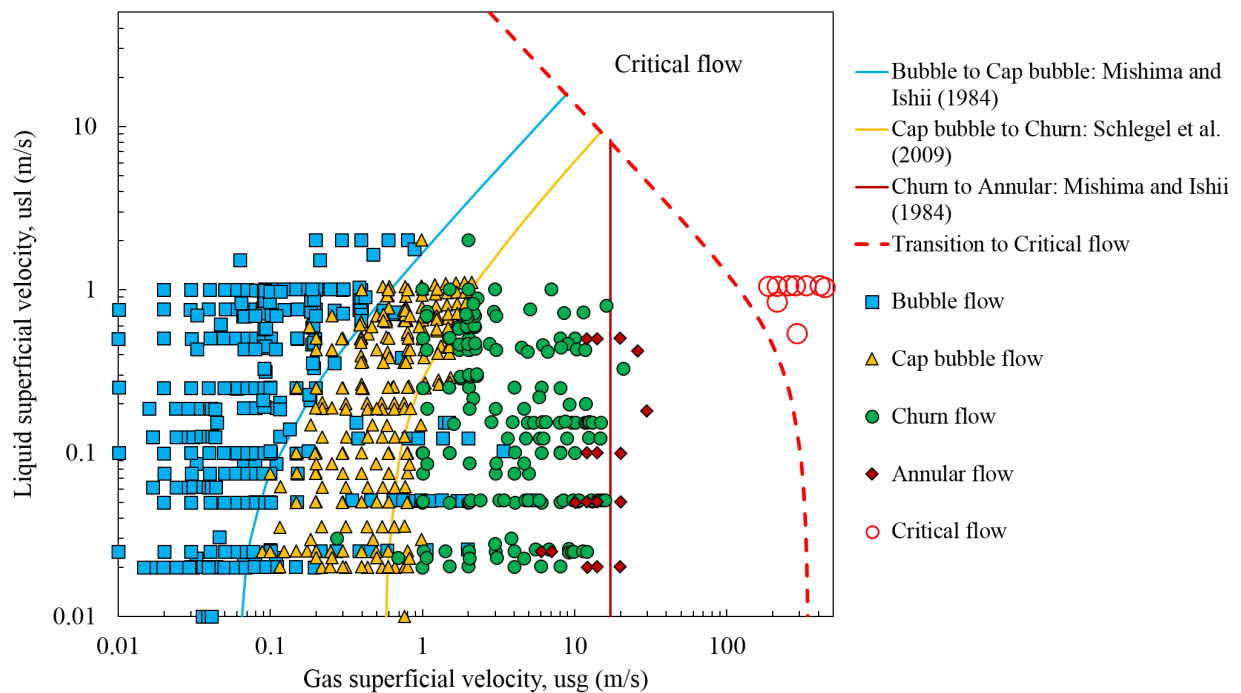


Figure 4.18. Proposed hybrid flow regime map with critical flow transition boundary.

The transition boundaries presented in Figure 4.18 are assumed to be valid for conditions close to the critical flow based on the mechanistic criteria that they were developed. However, it is known that when the flow gets close enough to critical conditions, some of those assumptions might be invalidated. As there is no available data (to the knowledge of the author) for the region between the critical flow boundary and the region delimited by the data reported in this work, it is difficult to predict how the flow will behave under such conditions. It should be noted that the flow regime transitions chosen for this map were

based on geometrical assumptions, which included for instance the idea that the bubbles would keep a spherical shape. Under the high turbulence expected on conditions close to critical flow, it is possible that these assumptions are invalid. Nevertheless, in the work published by Mishima and Ishii [19] and Schlegel et al. [32], the flow regime map are plotted to conditions of liquid superficial velocities up to 10 m/s (~ 33 ft/s), and gas superficial velocities of at least 100 m/s (~ 330 ft/s), without ever mentioning critical flow, as shown in Figure 4.19. Therefore, for the scope of this work, it is assumed that their assumptions are still valid up to that point.

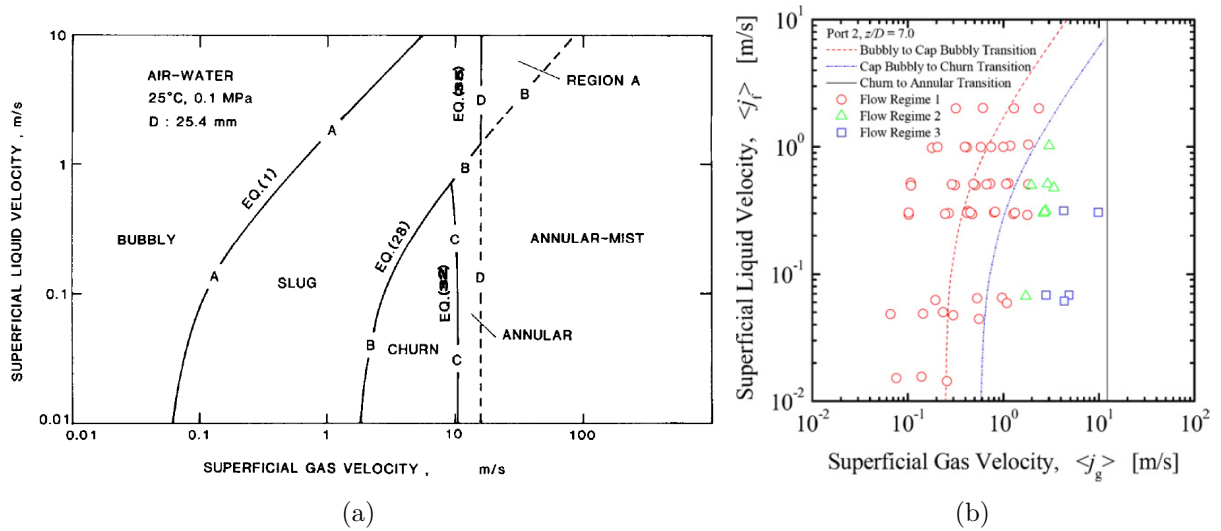


Figure 4.19. Flow regime maps by (a) Mishima and Ishii [19]; and (b) Schelegel et al. [32].

Chapter 5

Conclusions and Future Works

5.1 Summary and conclusions

1. Some recent studies pointed out significant differences for flow regimes between large and small diameter pipes. Among the main differences, the inexistence of slug flow in diameters larger than 0.10 m (~ 4 in) is reported by many authors. Thus, one of the sources of the errors is possibly related to the flow regime prediction, once most models were developed based on small diameter pipes. A criteria by Kataoka and Ishii [25] correlating the surface tension of the mixture and the pressure of the liquid phase over the bubble was used to define the largest diameter in which a Taylor bubble can be stable (i.e., slug flow is existent). It is considered that diameters larger than that should be considered large. It was noticed that while this diameter would increase with pressure for water-and-air mixtures, it would decrease for oil-and-gas mixtures.
2. Cap-bubble flow regime is proposed here under conditions at which slug flow would exist for $D_H^* > 40$. Cap-bubble flow regime is characterized by bubbles larger than the classical bubble flow, but these large bubbles never occupy the entire pipe diameter. These bubbles generate flow recirculation and increased turbulence.
3. A thorough literature review was carried out on six different flow regime maps – four mechanistic, and two empirical. Four flow regime maps were selected to be tested on predicting the flow regime for flows in large diameter pipes and relatively high fluid flow velocities: Duns and Ros [11], Aziz et al. [17], Mishima and Ishii [19], and Schlegel et al. [32].
4. A literature review was carried out on experiments for two-phase flow regime characterization of air and water flows in large diameter pipes. 695 data points of experimental flow regime observation were collected and used on the flow regime maps evaluation. Data from an experimental study carried out at LSU were presented in completeness

for the first time.

5. A new flow regime map was proposed after evaluating the different flow regime transition using Wu et al. [16] approach. It was proposed the existence of cap-bubble flow in large diameter pipe for conditions where slug flow would exist in smaller diameter pipes. The existence of this flow regime was considered an effect of the increasing pipe diameter size, with the former Taylor bubbles not being able to grow to the size of the pipe diameter, but reaching sizes larger than common bubbles in a classical bubble flow and being deformed because of instabilities due to turbulence.
6. A recent model proposed by Teles and Waltrich [33] was modified to adapt the use of the newly introduced flow regime map and the calculation of the pressure gradient under cap-bubble flow. The results from the simulations for the pressure gradient of the water and air experimental data and natural gas and oil field data presented improvements over the standard model. It was noticed for the calculation of pressure gradient of the air-and-water experimental data that the error difference between the standard and the modified model proposed in this work was tending to reduce with increasing diameter. This may be due to the diameter effect on the formation of bubbles, making their size less influent for lower gas throughput, and approaching its behavior more to churn flow with higher gas velocities.
7. Critical flow regime transition in large diameter was evaluated. A Homogeneous Equilibrium Model (HEM) by Wallis [41] was tested against data of a representative well in the GoM. An empirical model adapting the Wallis [41] for larger diameters was also evaluated. It was noticed that with increasing pressure, the parameter that affects the most on the critical flow velocities is the gas density. Under high pressures, the gas density will increase substantially, increasing the critical flow velocities. Because of this increase in critical velocities with pressure, it is unlikely that WCD on the sea floor will be in critical condition. However, when the discharge happens at lower

pressures, such as at atmospheric pressures at the rig floor, the flow might be in critical conditions. Therefore, it is recommended the addition of the critical flow transition in the new flow regime map.

8. Little is known about the effects of increasing velocity in the region between the end of the experimental data and the critical flow transition. It is estimated that the flow regime transition boundaries will be kept in such conditions because of their mechanistic nature. However, it is uncertain to affirm that they will indeed keep their form.

5.2 Recommendations for future work

For both experimental and numerical future work, the following recommendations are made.

1. In order to better understand the physics behind each flow regime and its particular characteristics, it is mandatory a better method to observe them. The visual characterization of flow regime is a limited method, and appears to be insufficient. Some authors correlate the void-fraction probabilistic density function (pdf) of a flow with different flow regimes, by the use of electrical impedance void-meters and artificial intelligence neural network. However, this method still do not give a good description of the physical phenomena happening during each flow regime. Other methods such as capturing the sound signature of flow regimes or works using wire mesh sensors are highly recommended.
2. The literature lacks experimental observations of flow regimes for oil and gas mixture flows under high pressure. Because of this, it is hard to prove the validity of Kataoka and Ishii [25] large diameter criteria for these fluids. This way, new experiments of two-phase flow with different diameter sizes, ranging from 0.02 to 0.08 m and high pressures are highly encouraged to evaluate the possible absence of slug flow by the classical definition under those conditions

3. Another important experimental investigation is on the effect of pipe inclination on flow regimes in large diameter pipes. By definition, slug flow in inclined pipes do not occupy its entire diameter. Therefore, it is possible that this flow is present in deviated wells and might highly influence the calculation of pressure gradients.
4. Due to the uncertainty about the flow behavior in conditions close to critical flow, it is recommended that new experimental studies are carried out for two-phase flow mixtures in velocities nearly around the predicted critical flow transition, ideally overlapping it. The flow regime identification and the flow behavior understanding under this conditions might be very important to predict surface release WCD.
5. It is recommended the evaluation of new critical flow transition models experimentally for diameters larger than 0.12 m to complement Beck et al. [61] work and develop better prediction methods for critical flow transition.

References

- [1] SPE, “Calculation of worst-case discharge (wcd),” tech. rep., Society of Petroleum Engineers, 2015.
- [2] K. Buchholz, A. Krieger, J. Rowe, D. S. Etkin, D. F. McCay, M. S. Gearon, M. Grennan, and J. Turner, “Oil spill response plan (osrp) equipment capabilities review - task 1: Worst case discharge analysis (volume i),” Tech. Rep. BPA No. E14PB00072, U.S. Department of the Interior Bureau of Safety and Environmental Enforcement (BSEE), 02 2016.
- [3] M. Zulqarnain, *Deepwater Gulf of Mexico oil spill scenarios development and their associated risk assessment*. PhD thesis, Louisiana State University, Craft & Hawking Petroleum Engineering Department, 2015.
- [4] M. J. Economides, A. D. Hill, C. Ehlig-Economides, and D. Zhu, *Petroleum Production Systems*. Prentice Hall, 2nd ed. ed., Oct. 2012.
- [5] G. Takacs, “Considerations on the selection of an optimum vertical multiphase pressure drop prediction model for oil wells,” in *SPE Production and Operations Symposium held in Oklahoma City, Oklahoma, 24–27 March 2001*, no. SPE-68361-MS, 2001.
- [6] N. Omebere-Iyari, B. Azzopardi, and Y. Ladam, “Two-phase flow patterns in large diameter vertical pipes at high pressures,” *AIChE J.*, vol. 53, pp. 2493–2504, 10 2007.
- [7] S. F. Ali, *Two phase flow in large diameter vertical riser*. PhD thesis, Cranfield University, School of Engineering, Department of Process and System Engineering, 2009.
- [8] G. Zabarar, R. Menon, W. Schoppa, and M. W. III, “Large diameter riser laboratory gas-lift tests,” in *Offshore Technology Conference held in Houston, Texas, USA*, no. OTC 23968, 2013.
- [9] P. Waltrich, M. S. Capovilla, W. Lee, P. C. de Souza, M. Zulqarnain, R. Hughes, M. Tyagi, W. Williams, S. Kam, A. Archer, J. Singh, H. Nguyen, J. Duhon, and C. Griffith, “Experimental evaluation of wellbore flow models applied to worst-case-discharge calculations,” in *SPE Health, Safety, Security, Environment & Social Responsibility Conference-North America*, no. SPE184444-MS, 04 2017.
- [10] O. Shoham, *Mechanistic modeling of gas-liquid two-phase flow in pipes*. Society of Petroleum Engineers, 2006.
- [11] H. J. Duns and N. Ros, “Vertical flow of gas and liquid mixtures in wells,” in *6th World Petroleum Congress*, no. WPC-10132, World Petroleum Congress, 06 1963.
- [12] H. Gray, *Vertical Flow Correlation in Gas Wells*. Appendix B, user’s manual for api

148 subsurface controlled safety valve sizing computer program ed., 1974.

- [13] A. Ansari, N. Sylvester, O. Shoham, J. Brill, *et al.*, “A comprehensive mechanistic model for upward two-phase flow in wellbores,” in *SPE Annual Technical Conference and Exhibition*, Society of Petroleum Engineers, 1990.
- [14] T. Hibiki and M. Ishii, “One-dimensional drift-flux model for two-phase flow in a large diameter pipe,” *International Journal of Heat and Mass Transfer*, vol. 46, no. 10, pp. 1773–1790, 2003.
- [15] J. Brill and H. Mukherjee, *Multiphase Flow in Wells, No. 17*. Society of Petroleum, 1999.
- [16] B. Wu, M. Firouzi, T. Mitchell, T. E. Rufford, C. Leonardi, and B. Towler, “A critical review of flow maps for gas-liquid flows in vertical pipes and annuli,” *Chemical Engineering Journal*, vol. 326, pp. 350–377, Oct. 2017.
- [17] K. Aziz, G. W. Govier, and M. Fogarasi, “Pressure drop in wells producing oil and gas,” *Journal of Canadian Petroleum Technology*, vol. 11, no. 03, 1972.
- [18] Y. Taitel, D. Barnea, and A. Dukler, “Modelling flow pattern transitions for steady upward gas-liquid flow in vertical tubes,” *AIChE J.*, vol. 26, pp. 345–354, 05 1980.
- [19] K. Mishima and M. Ishii, “Flow regime transition criteria for upward two-phase flow in vertical tubes,” *International Journal of Heat and Mass Transfer*, vol. 27, pp. 723–737, May 1984.
- [20] D. Barnea, “A unified model for predicting flow-pattern transitions for the whole range of pipe inclinations,” *Int. J. Multiphase Flow*, vol. 13, no. 1, pp. 1–12, 1987.
- [21] N. Omebere-Iyari, B. Azzopardi, D. Lucas, M. Beyer, and H.-M. Prasser, “The characteristics of gas/liquid flow in large risers at high pressures,” *Int. J. Multiphase Flow*, vol. 34, pp. 461–476, 2008.
- [22] T. Smith, J. Schlegel, T. Hibiki, and M. Ishii, “Two-phase flow structure in large diameter pipes,” *Int. J. Heat Fluid Flow*, vol. 33, pp. 156–167, 2012.
- [23] A. Ohnuki and H. Akimoto, “Experimental study on transition of flow pattern and phase distribution in upward air-water two-phase flow along a large vertical pipe,” *Int. J. Multiphase Flow*, vol. 26, pp. 367–386, 2000.
- [24] S. F. Ali and H. Yeung, “Two-phase flow patterns in large diameter vertical pipes,” *Asia-Pacific Journal of Chemical Engineering*, vol. 9, pp. 105–116, June 2014.
- [25] I. Kataoka and M. Ishii, “Drift flux model for large diameter pipe and new correlation for pool void fraction,” *Int. J. Heat Mass Transfer*, vol. 30, no. 9, pp. 1927–1939, 1987.

- [26] H. Cheng, J. H. Hills, and B. J. Azzopardi, “A study of the bubble-to-slug transition in vertical gas-liquid flow in columns of different diameters,” *Int. J. Multiphase Flow*, vol. 24, no. 3, pp. 431–452, 1998.
- [27] T. Hibiki and M. Ishii, “Experimental study on hot-leg u-bend two-phase natural circulation in a loop with a large diameter pipe,” *Nuclear Engineering and Design*, vol. 195, pp. 69–84, 2000.
- [28] M. Shoukri, I. Hassan, and I. Gerges, “Two-phase bubbly flow structure in large-diameter vertical pipes,” *The Canadian Journal of Chemical Engineering*, 2003.
- [29] M. S. Capovilla, P. C. de Sousa, and P. J. Waltrich, “Experimental investigation of vertical high-velocity two-phase flows in large-diameter pipes,” in *18th International Conference on Multiphase Production Technology 2017, Cannes, France*, 2017.
- [30] Minerals Management Service, “Gulf of Mexico deepwater operations and activities,” Environmental Assessment OCS EIS/EA MMS 2000-001, U.S. Department of the Interior - Minerals Management Service, New Orleans, May 2000.
- [31] N. Ros *et al.*, “Simultaneous flow of gas and liquid as encountered in well tubing,” *Journal of Petroleum Technology*, vol. 13, no. 10, pp. 1–037, 1961.
- [32] J. Schlegel, P. Sawant, S. Paranjape, B. Ozar, T. Hibiki, and M. Ishii, “Void fraction and flow regime in adiabatic upward two-phase flow in large diameter vertical pipes,” *Nuclear Engineering and Design*, vol. 239, pp. 2864–2874, 2009.
- [33] F. B. X. Teles, P. J. Waltrich, M. S. Capovilla, I. Gupta, and R. Highes, “Development and improvement of flow models applied to multiphase flows in large-diameter pipes and high-velocity flows,” Internal interim report prepared under BOEM Award M17PX00030 by Louisiana State University, US Department of the Interior - Bureau of Ocean Energy Management, 2018.
- [34] E. Pagan, W. Williams, S. Kam, and P. Waltrich, “A simplified model for churn and annular flow regimes in small-and large-diameter pipes,” *Chemical Engineering Science*, vol. 162, pp. 309–321, 2017.
- [35] A. Hagedorn and K. Brown, “The effect of liquid viscosity in two-phase vertical flow,” *Journal of Petroleum Technology*, vol. 16-02, pp. 203 – 210, 02 1964.
- [36] D. Beggs and J. Brill, “A study of two-phase flow in inclined pipes,” *Journal of Petroleum Technology*, vol. 25-05, 05 1973.
- [37] Schlumberger, “Olga dynamic multiphase flow simulator,” 2000.
- [38] H. Mukherjee and J. Brill, “Pressure drop correlations for inclined two-phase flow,” *Journal of energy resources technology*, vol. 107, no. 4, pp. 549–554, 1985.

- [39] S. Jayanti and N. Brauner, “Churn flow,” *Multiphase Science and Technology*, vol. 8, no. 1-4, 1994.
- [40] M. V. C. Alves, *Modelagem Numerica do Escoamento Transient Churn-Annular em Tubulacoes Verticais e sua Aplicacao na Simulacao de Carga de Liquido em Pocos de Gas*. PhD thesis, Universidade Federal de Santa Catarina, Florianopolis, Santa Catarina, 2014.
- [41] G. B. Wallis, *One Dimensional Two-Phase Flow*. Ney York: McGraw-Hill, 1969.
- [42] N. Brauner and D. Barnea, “Slug/churn transition in upward gas-liquid flow,” *Chemical engineering science*, vol. 41, no. 1, pp. 159–163, 1986.
- [43] K. McQuillan and P. Whalley, “Flow patterns in vertical two-phase flow,” *International Journal of Multiphase Flow*, vol. 11, pp. 161–175, mar 1985.
- [44] A. Hasan and C. Kabir, “Two-phase flow in vertical and inclined annuli,” *International Journal of Multiphase Flow*, vol. 18, no. 2, pp. 279–293, 1992.
- [45] S. Jayanti and G. Hewitt, “Prediction of the slug-to-churn flow transition in vertical two-phase flow,” *International Journal of Multiphase Flow*, vol. 18, no. 6, pp. 847–860, 1992.
- [46] J. Tengesdal, A. Kaya, C. Sarica, *et al.*, “Flow-pattern transition and hydrodynamic modeling of churn flow,” *SPE Journal*, vol. 4, no. 04, pp. 342–348, 1999.
- [47] M. Ishii, “One-dimensional drift-flux model and constitutive equations for relative motion between phases in various two-phase flow regimes,” Tech. Rep. ANL-77-47, Argonne National Laboratory, 9700 South Class Avenue; Argonne, Illinois 60439, 10 1977.
- [48] J. Weisman, D. Duncan, J. Gibson, and T. Crawford, “Effects of fluid properties and pipe diameter on two-phase flow patterns in horizontal lines,” *International Journal of Multiphase Flow*, vol. 5, no. 6, pp. 437–462, 1979.
- [49] Y. Taitel and A. Dukler, “A model for predicting flow regime transitions in horizontal and near horizontal gas-liquid flow,” *AIChE Journal*, vol. 22, no. 1, pp. 47–55, 1976.
- [50] G. F. Hewitt and G. B. Wallis, “Flooding and associated phenomena in falling film flow in a tube,” tech. rep., United Kingdom Atomic Energy Authority. Research Group. Atomic Energy Research Establishment, Harwell Berks, England, 1963.
- [51] A. Bennett, “Flow visualisation studies of boiling at high pressure,” *Proc. Inst. Mech. Eng.*, vol. 180, pp. 1–11, 1965.
- [52] T. Smith, “Two-phase flow regime identification in large diameter pipes,” *MSNE Thesis, Purdue University, USA*, 1999.

- [53] G. B. Wallis, “Critical two-phase flow,” *International Journal of Multiphase Flow*, vol. 6, no. 1-2, pp. 97–112, 1980.
- [54] W. Gilbert *et al.*, “Flowing and gas-lift well performance,” in *Drilling and production practice*, American Petroleum Institute, 1954.
- [55] F. Ashford *et al.*, “An evaluation of critical multiphase flow performance through wellhead chokes,” *Journal of Petroleum Technology*, vol. 26, no. 08, pp. 843–850, 1974.
- [56] F. Ashford, P. Pierce, *et al.*, “Determining multiphase pressure drops and flow capacities in down-hole safety valves,” *Journal of Petroleum Technology*, vol. 27, no. 09, pp. 1–145, 1975.
- [57] R. Sachdeva, Z. Schmidt, J. Brill, R. Blais, *et al.*, “Two-phase flow through chokes,” in *SPE Annual Technical Conference and Exhibition*, Society of Petroleum Engineers, 1986.
- [58] S. Selmer-Olsen, H. Holm, K. Haugen, P. J. Nilsen, and R. Sandberg, “Subsea chokes as multiphase flowmeters,” in *International Conference on Multiphase Production, Cannes, France.*, 1995.
- [59] F. Beck, J. Langlinais, A. Bourgoyne Jr, *et al.*, “Experimental and theoretical considerations for diverter evaluation and design,” in *SPE California Regional Meeting*, Society of Petroleum Engineers, 1986.
- [60] F. Fortunati, “Two-phase flow through wellhead chokes,” in *SPE European Spring Meeting*, Society of Petroleum Engineers, 1972.
- [61] F. Beck, J. Langlinais, A. Bourgoyne Jr, *et al.*, “An analysis of the design loads placed on a well by a diverter system,” in *SPE/IADC Drilling Conference*, Society of Petroleum Engineers, 1987.
- [62] G. Oddie, H. Shi, L. Durlofsky, K. Aziz, B. Pfeffer, and J. Holmes, “Experimental study of two and three phase flows in large diameter inclined pipes,” *International Journal of Multiphase Flow*, vol. 29, no. 4, pp. 527–558, 2003.
- [63] A. Ohnuki and H. Akimoto, “An experimental study on developing air-water two-phase flow along a large vertical pipe: effect of air injection method,” *Int. J. Multiphase Flow*, vol. 22, no. 6, pp. 1143–1154, 1996.
- [64] X. Shen, J. P. Schlegel, S. Chen, S. Rassame, M. J. Griffiths, T. Hibiki, and M. Ishii, *Frontiers and Progress in Multiphase Flow I*, ch. Chapter 2 - Flow Characteristics and Void Fraction Prediction in Large Diameter Pipes, pp. 55–103. Springer, 2014.
- [65] H. Asheim *et al.*, “Mona, an accurate two-phase well flow model based on phase slippage,” *SPE Production Engineering*, vol. 1, no. 03, pp. 221–230, 1986.

- [66] P. J. Waltrich, G. Falcone, and J. R. Barbosa, “Axial development of annular, churn and slug flows in a long vertical tube,” *Int. J. Multiphase Flow*, vol. 57, pp. 38–48, 2013.
- [67] G. Hewitt and S. Jayanti, “To churn or not to churn,” *International Journal of Multiphase Flow*, vol. 19, no. 3, pp. 527–529, 1993.
- [68] K. Reinicke, R. Remer, and G. Hueni, “Comparison of measured and predicted pressure drops in tubing for high-water-cut gas wells,” in *1987 SPE Annual Technical Conference and Exhibition held in Houston, Spet 16-19*, no. SPE13279, 1987.

Appendix:
Data from LSU experiments

Table A.1. Experimental data generated at LSU.

ID (m)	u_{sg} (m/s)	u_{sl} (m/s)	dp/dz (kPa/m)	H_l (-)	Obs. FR
0.10	0.140	0.134	7.759	0.99	Bubbly
0.10	0.147	0.582	5.540	0.56	Slug/Churn
0.10	0.152	1.605	3.710	0.36	Churn
0.10	0.155	2.830	2.833	0.20	Churn
0.10	0.155	3.884	2.557	0.13	Churn
0.10	0.155	6.457	2.264	0.12	Churn
0.10	0.157	8.624	2.031	0.06	Churn
0.10	0.182	29.669	1.855	0.11	Annular
0.10	0.477	0.395	6.626	0.70	Slug/Churn
0.10	0.450	1.503	4.496	0.39	Slug/Churn
0.10	0.469	2.746	3.504	0.28	Churn
0.10	0.445	4.461	3.122	0.25	Churn
0.10	0.462	6.164	2.608	0.20	Churn
0.10	0.466	8.989	2.562	0.18	Churn
0.10	0.331	20.723	2.045	0.08	Churn/Annular
0.10	0.422	25.973	1.972	0.09	Annular
0.10	0.902	0.421	7.343	0.73	Bubbly
0.10	0.953	1.114	5.456	0.51	-
0.10	0.885	2.285	4.141	0.32	Churn
0.10	0.827	3.402	3.118	0.41	-
0.10	0.857	6.301	2.734	0.21	-
0.10	0.829	8.636	2.570	0.16	-
0.10	0.803	16.035	2.998	0.14	-
0.10	1.639	0.471	8.284	0.73	-
0.10	1.776	0.878	7.559	0.59	-
0.10	1.727	1.982	5.960	0.33	-
0.10	1.690	3.440	5.148	0.24	-
0.10	1.714	5.529	4.941	0.23	-
0.10	1.717	7.863	4.810	0.14	-
0.10	1.749	16.333	5.627	0.17	-
0.10	4.232	0.059	10.983	0.90	-
0.10	4.228	0.590	10.587	0.69	-
0.10	4.125	0.867	10.339	0.55	-
0.10	4.248	1.740	10.270	0.69	-
0.10	4.247	1.675	10.326	0.59	-
0.10	4.173	2.671	10.206	0.50	-
0.10	4.350	4.505	11.416	0.43	-
0.10	4.349	4.458	11.380	0.54	-

continued ...

... continued

ID (m)	u_{sg} (m/s)	u_{sl} (m/s)	dp/dz (kPa/m)	H_l (-)	Obs. FR
0.10	4.216	6.032	11.811	0.28	-
0.10	3.982	10.135	13.756	0.12	-
0.20	0.203	0.600	5.784	0.60	-
0.20	0.225	1.099	4.625	-	-
0.20	0.221	2.142	3.243	0.28	-
0.20	0.216	4.350	2.477	0.28	Slug
0.20	0.220	5.803	1.712	0.17	Churn
0.20	0.199	9.212	1.672	0.20	Churn
0.20	0.268	10.565	1.889	0.21	-
0.20	0.200	11.796	1.286	0.13	Churn/Annular
0.20	0.215	13.206	1.297	0.12	-
0.20	0.385	0.728	5.896	0.58	Bubble
0.20	0.426	1.008	5.296	-	-
0.20	0.406	2.093	3.733	0.40	-
0.20	0.398	3.587	2.770	0.31	-
0.20	0.417	4.890	2.423	0.25	Churn
0.20	0.443	8.073	2.332	0.24	Churn
0.20	0.421	6.311	2.146	0.21	-
0.20	0.418	6.621	2.083	0.24	Churn
0.20	0.433	10.293	2.107	0.15	Churn
0.20	0.429	11.640	1.830	0.13	Churn
0.20	0.711	0.654	6.915	0.70	Bubble
0.20	0.701	1.157	5.858	0.56	Bubble
0.20	0.720	1.907	4.855	0.49	-
0.20	0.739	2.935	4.125	0.41	Churn
0.20	0.761	5.065	3.364	0.32	Churn
0.20	0.721	6.117	2.938	0.27	-
0.20	0.722	8.467	2.611	0.26	Churn/Annular
0.20	0.729	11.411	2.453	0.22	Churn/Annular
0.20	0.723	11.921	2.465	0.26	-
0.30	0.025	0.161	8.236	-	-
0.30	0.030	0.272	7.285	-	Churn
0.30	0.026	0.281	6.595	-	-
0.30	0.027	0.420	5.940	-	-
0.30	0.027	0.546	5.609	-	-
0.30	0.027	0.654	5.208	-	-
0.30	0.023	0.687	5.654	0.60	Churn
0.30	0.027	0.758	4.994	-	-
0.30	0.026	0.947	4.520	-	-
0.30	0.026	0.984	4.508	-	-
0.30	0.028	2.979	2.588	-	Churn
0.30	0.030	3.832	2.250	0.27	Churn

continued ...

... continued

ID (m)	u_{sg} (m/s)	u_{sl} (m/s)	dp/dz (kPa/m)	H_l (-)	Obs. FR
0.30	0.056	1.000	4.487	-	-
0.30	0.054	0.988	4.762	-	-
0.30	0.053	0.921	5.028	-	-
0.30	0.055	0.796	5.192	-	-
0.30	0.054	0.693	5.581	-	-
0.30	0.057	0.603	5.722	-	-
0.30	0.057	0.480	6.192	-	-
0.30	0.056	0.393	6.589	-	-
0.30	0.055	0.263	7.157	-	-
0.30	0.086	0.201	7.750	-	-
0.30	0.096	0.231	7.646	-	-
0.30	0.088	0.276	7.340	-	-
0.30	0.086	0.351	7.012	-	-
0.30	0.087	0.440	6.597	-	-
0.30	0.086	0.509	6.353	-	-
0.30	0.086	0.616	5.970	-	-
0.30	0.090	0.678	5.840	0.64	-
0.30	0.088	0.711	6.353	-	-
0.30	0.102	0.839	5.463	0.59	-
0.30	0.089	1.715	3.609	0.43	Churn
0.30	0.095	3.742	2.615	-	-
0.30	0.088	3.912	2.286	-	-
0.30	0.090	5.968	1.837	0.27	-
0.30	0.087	7.932	1.704	0.22	-
0.30	0.129	0.245	7.703	-	-
0.30	0.131	0.333	7.255	-	-
0.30	0.130	0.406	6.876	-	-
0.30	0.131	0.488	6.663	-	-
0.30	0.129	0.565	6.362	-	-
0.30	0.128	0.657	6.000	-	-
0.30	0.134	0.748	5.840	-	-
0.30	0.144	0.826	5.499	0.60	-
- 0.30	0.179	1.278	5.237	0.56	-
0.30	0.186	1.826	4.299	0.46	-
0.30	0.186	3.785	3.004	0.33	-
0.30	0.184	6.060	2.419	0.30	-
0.30	0.179	7.921	2.205	0.29	-
0.30	0.460	1.149	6.225	0.72	-
0.30	0.463	1.901	4.606	0.54	-
0.30	0.459	3.907	3.353	0.41	-
0.30	0.454	5.843	2.996	0.34	-
0.30	0.418	7.644	2.625	0.32	-

continued ...

... continued

ID (m)	u_{sg} (m/s)	u_{sl} (m/s)	dp/dz (kPa/m)	H_l (-)	Obs. FR
0.30	0.716	0.298	8.385	0.86	Bubbly
0.30	0.728	0.656	7.162	0.75	Bubbly
0.30	0.736	1.066	6.797	0.71	Churn
0.30	0.724	1.782	5.460	0.83	-
0.30	0.735	2.662	4.714	0.53	-
0.30	0.733	3.571	3.991	0.47	-
0.30	0.729	3.832	3.857	0.48	-
0.30	0.725	5.562	3.529	0.40	-
0.30	0.717	7.407	2.287	0.29	-

Vita

Matheus Sigaki Capovilla was born in Maringá, Paraná, Brazil, on January 12, 1992. He is son of Ivete Naomi Sigaki and Marcos Aurelio Borges Capovilla.

Matheus started his academic career at the Federal university of Santa Catarina in August, 2010. During his Mechanical Engineering undergraduate course, he joined an emerging technologies research team at Polo Research Laboratories for Emerging Technologies in Cooling and Thermophysics. He helped developing the first operating magnetic refrigeration prototype in the Southern Hemisphere.

After graduating in September of 2015, he was accepted to enter the Graduate Program at Louisiana State University in Petroleum Engineering with full assistantship. He started his program in January of 2016.